ANALOG SIGNAL PROCESSING WITH TOPOLOGICAL METAMATERIALS

Farzad ZANGENEH NEJAD

École
polytechnique
fédérale
de Lausanne

2021

Dedication

To my Dear wife, for her continuous and unparalleled love. To my mother for her unconditional support in every step of the way.

Acknowledgements

I could not accomplish this thesis without the endless support of many people, to whom I am kindly grateful. First and foremost, I would like to warmly thank my supervisor, Professor Romain Fleury, for his guidance and extreme support throughout my time at EPFL. It was one of the best opportunities of my life to work with him in a very relaxed environment. I learned a great deal from his experience and expertise. I am very grateful that, despite his extremely busy schedule, he always dedicated some of his time to our discussions. I cannot imagine that I was able to accomplish even one chapter of this dissertation without his support and extreme commitment.

The influence of Romain on me goes beyond science. During the last four years, he helped me a lot to deal with the problems that I had in my life, from the tiniest to the biggest ones. He provided me with highly insightful, inspiring discussions about every single aspect of my life, from personal to professional. For me, Romain was like a gracious father who trains his children patiently and helps them kindly, without any hesitation and getting tired. I will be forever grateful to him. I cannot find the right word and sentence to express my gratitude to him, so I just stop acknowledging him.

I would like to thank all members of my thesis committee: Prof. Demetri Psaltis, Prof. Andrea Alu, Prof. Anja Skrivervik, and Prof. Muamer Kadic, for providing me with insightful comments and encouragement, and for the hard questions which helped me broaden the horizons of my research from various perspectives.

During my Ph.D., I had the privilege to work with outstanding and, at the same time, humble experts in our group. I thank all members of LWE for making a friendly, convenient, and warm working environment. I am thankful for the energy that I received from the postdocs of our group, Drs. Nadege Kaina, Bakhtiyar Orazbayev, Mohammad Sajjad Mirmoosa, and Maliheh

Abstract

Originally discovered in condensed matter systems, topological insulators (TIs) have been ubiquitously extended to various fields of classical wave physics including photonics, phononics, acoustics, mechanics, and microwaves. In the bulk, like any other insulator, TIs prohibit energy propagation. On their surface, however, they support one-way propagative states with inherent protection against certain types of disorders and defects. In this work, I explore the possibility of performing advanced signal processing and analog computing tasks based on the boundary states of wave topological insulators. By providing numerical and experimental verifications, I demonstrate that such kind of computing scheme, referred to as topological analog signal processing, provides one with strong robustness against imperfection and disorder. It is in sharp contrast to conventional signal processors, which are often very sensitive to geometrical tolerances. Going a step further, I even demonstrate that, in some topological systems with specific parameter ranges, the harmful effects of the disorder can be turned into an asset so as trigger functionalities of interest. These findings open up large perspectives for a new generation of all-optical signal processors that are not only fast and power-efficient but also offer strong levels of reliability and robustness to disorder.

Keywords

Résumé

Découvert à l'origine dans les systèmes de matière condensée, les isolants topologiques (TI) ont été étendus à divers domaines de la physique des ondes classiques, notamment la photonique, la phononique, l'acoustique, la mécanique et les micro-ondes. A l'intérieur, comme tout autre isolant, les TI présentent une résistance excessivement élevée à la propagation d'énergie ondulatoire, interdisant la transmission d'énergie. A leur périphérie externe, cependant, ils supportent des modes de bords topologiques dont l'existence est robuste à certains types d'imperfections, et à des niveaux modérés de désordre. Dans cette thèse, j'étudie la possibilité inexplorée d'effectuer des tâches avancées de traitement du signal et de calcul analogique en utilisant les états de bord des isolants topologiques. En s'appuyant sur des vérifications numériques et expérimentales, je démontre que ce type d'approche, appelé traitement topologique de signaux analogiques, offre une forte robustesse contre les imperfections géométriques et le désordre. Cela contraste fortement avec les systèmes analogiques et les processeurs de signaux conventionnels, qui sont souvent très sensibles aux tolérances géométriques. Allant plus loin, je démontre même que, dans certains systèmes topologiques, les effets habituellement nocifs du désordre peuvent se transformer en un atout pour déclencher des fonctionnalités d'intérêt. Ces découvertes ouvrent de grandes perspectives pour une nouvelle génération de processeurs de signaux entièrement analogiques qui non seulement effectuent des tâches de traitement du signal ultrarapides, à haut débit et basse puissance, mais offrent également de hauts niveaux de fiabilité et de robustesse au désordre.

Contents

List of Figures

List of Equations

Chapter 1   Introduction

1.1   Analog signal processing

Nowadays, digital computers are ubiquitously used for carrying out a large variety of computational functionalities, from relatively simple to highly complex ones. Such general-purpose functionality, however, comes with the restriction of high-power consumption, rendering digital computers expensive for performing simple operations such as differentiation or integration [1]. In addition, the approach to employ digital techniques for computation is often accompanied with a time delay between the input and the output that grows exponentially as the complexity of the computational task is increased [1]. For these reasons, researchers have recently tried to revisit the old idea of analog computing. An analog computer leverages the continuously changeable aspects of a physical phenomenon, such as the current of an electrical circuit or the motion of a mechanical aid, to solve the computational problem [2]. Such kinds of analog computing systems are much simpler than their digital versions. Yet, their slow speed and bulky structure hinder their applicability in modern systems, where speed and miniaturization are sought. In 2015, however, an idea [3] was proposed to perform ultra-fast analog computation at scales much smaller than the wavelength. The idea was to leverage the continuous aspects of waves (in particular propagating optical fields) interacting with artificial structures (called metamaterials [4]) to perform the desired computational operation. The ultra-fast character of optical waves enables an almost instantaneous response, leading to an ultra-high computational speed for these kinds of computational systems. In addition, thanks to their analog nature, such types of computing structures are less expensive than
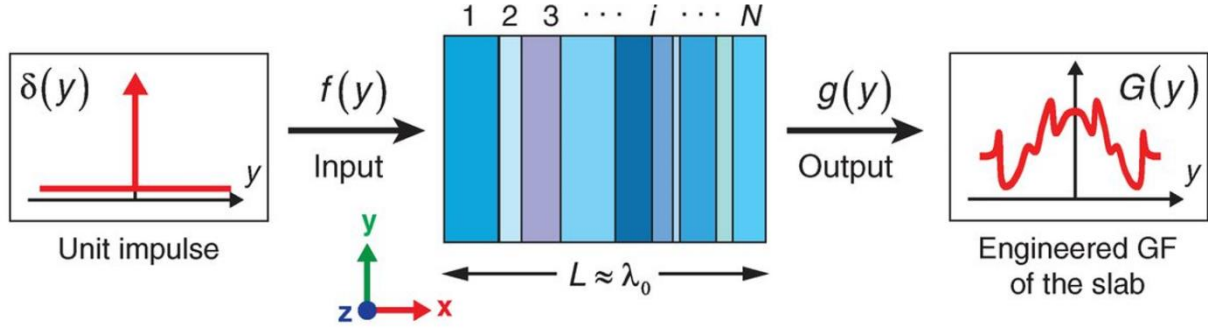
Figure 1.1: Analog computing based on Green's function approach. Consider a multilayer of dielectrics. By changing the refractive indices and thicknesses of the dielectric layers, one may implement the Green's function $g(y)$, associated with a desired operator [3].

digital signal processors. These salient features established wave-based computing systems as cornerstones for performing special-purpose signal processing tasks such as image processing and equation solving.

Following the pioneering work of [3], many proposals were proposed to perform wave-based computational operations. In a broad sense, the proposed approaches for wave-based computing can be classified into two types. The first approach (known as Green's function method) realizes the functionality of interest in real space, by engineering the parameters of the system such that its Green's function matches the one of the desired operator. The alternative strategy, on the other hand, realizes the operator of choice in the Fourier domain, by tailoring the spectral characteristics of the input signal using a meta-structure. In the following, I explain both of these approaches in detail.

1.2 Green's function approach

Consider an arbitrary structure, for example, a multilayer of dielectrics with varying refractive indices and thicknesses (Figure. 1.1). Suppose that the structure is interacting with an irregularly shaped optical field $f(y)$. Our goal is to apply a specific mathematical operation, such as differentiation, to $f(y)$. To this end, an intuitive approach is to engineer the refractive indices and thicknesses of the dielectric layers such that the Green's function of the system becomes identical
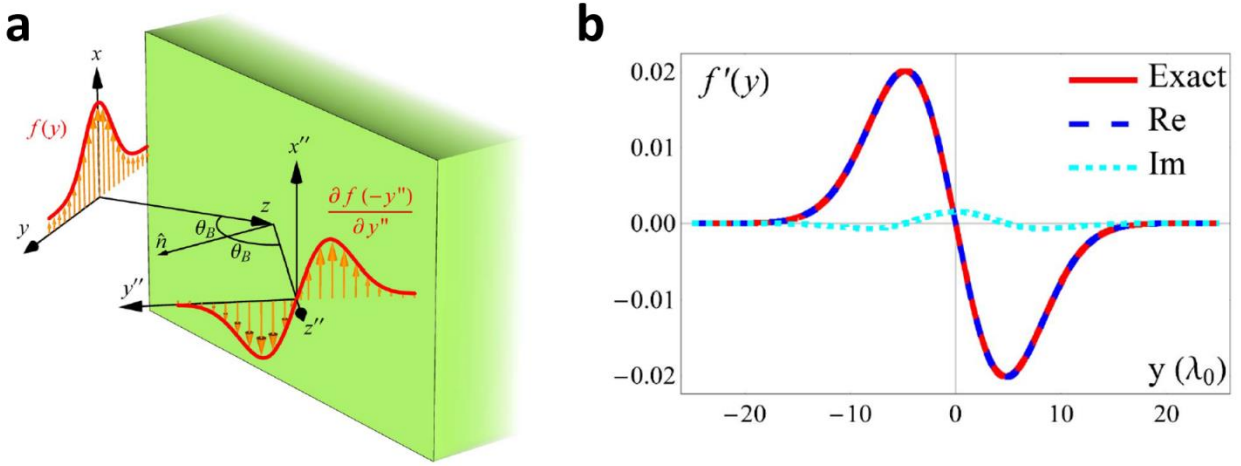
Figure 1.2: Analog spatial differentiator based on Green's function approach, a, A TM-polarized incident field impinges on the interface between a dielectric and free space at the Brewster angle. b, The corresponding reflected field is nothing but the spatial derivative of the input signal [5].

to that of the operator of choice, which is for example $G(k_y) = ik_y$ for the derivative operator $(\partial/\partial y)$. Such an approach is referred to as Green's function (GF) approach in the literature [3]. This appellation comes from the fact the GF technique realizes the intended Green' function directly in real space (as opposed to the metasurface approach that realizes the desired operator in the Fourier domain).

I now discuss several representative examples of wave-based computing systems based on GF approach. Consider the configuration shown in Fig 1.2a [5], consisting of an interface between two dielectrics with different refractive indices ($n_1 = 1$, and $n_2 = 3.4$). Suppose that a TM-polarized Gaussian incident field impinges on the interface between the two dielectrics. The incident angle is assumed to be $\theta_b = tan^{-1}(n_2/n_1)$. At this incident angle, known as Brewster angle, the reflection coefficient of the structure vanishes. Near θ_b, by employing a simple Taylor expansion, one can approximate the reflection coefficient of the interface with a linear function of the form $R(k_y) = Ak_y$, with A being an arbitrary constant. Interestingly, $R(k_y)$ is quite similar to the Green's function of the ideal differentiator $G(k_y) = ik_y$. This implies that, for those signals impinging the structure at the Brewster angle, the corresponding reflected field is nothing but the derivative of the incident field. This effect is demonstrated in the inset of Fig. 1.2b, in which I have
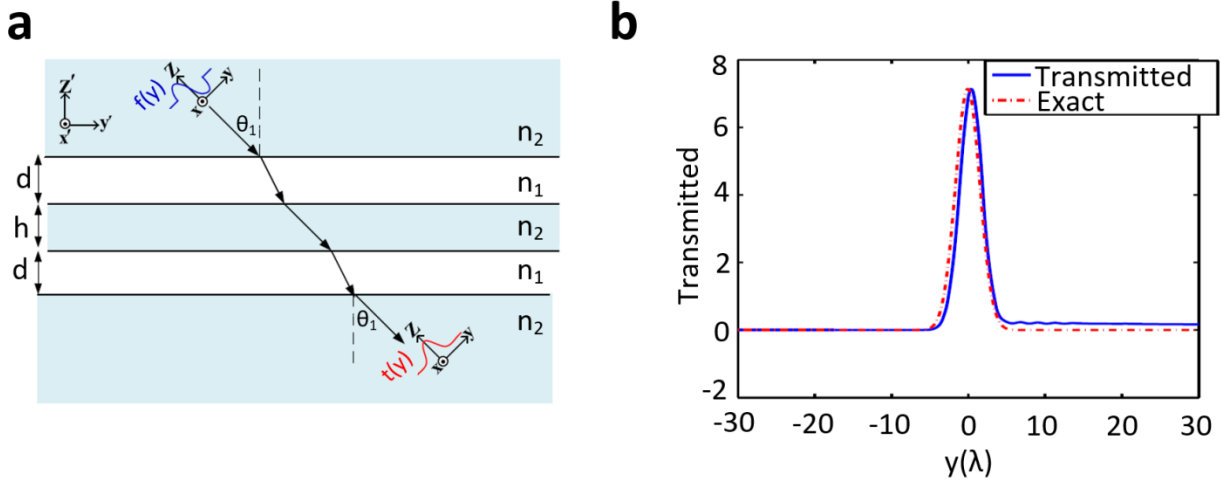
Figure 1.3: Analog spatial integration based on Green's function approach, a, An incident field excites the guided mode of a dielectric slab from the far field. b, The corresponding transmitted field is nothing but the spatial integration of the input signal [6].

reported the reflected field corresponding to a Gaussian-type incident signal. It is observed that the reflected field has a Gaussian-derivative profile, constituting an evidence of the fact that the interface indeed acts as an optical spatial differentiator.

Figure 1.3a represents another example [6] of a wave-based analog computing based on GF method. Consider a well-known dielectric slab waveguide, consisting of a core layer with the refractive index of $n_2 = 3.4$, and cladding layers having refractive indices of $n_1 = 1$. A prism coupler is used to excite the structure from the far-field. The incident angle is chosen such that the momentum of the incoming beam becomes equal to the one of the guided mode of the dielectric slab waveguide, leading to a resonance peak in the transmission spectrum. Near this resonance, assuming that the incoming field has no DC component, we can approximate the transmission coefficient of the structure using the relation $T(k_y) = A/k_y$, in which A is an arbitrary constant. The fact that the transmission coefficient of the structure is identical to the Green's function of the ideal integrator ($G(k_y) = 1/ik_y$) implies that, for signals having no zero Fourier component, the structure under study functions as an analog integrator. This is confirmed in Figure 1.3b, in which I have considered a Gaussian derivative signal as the incident wave and calculated the corresponding
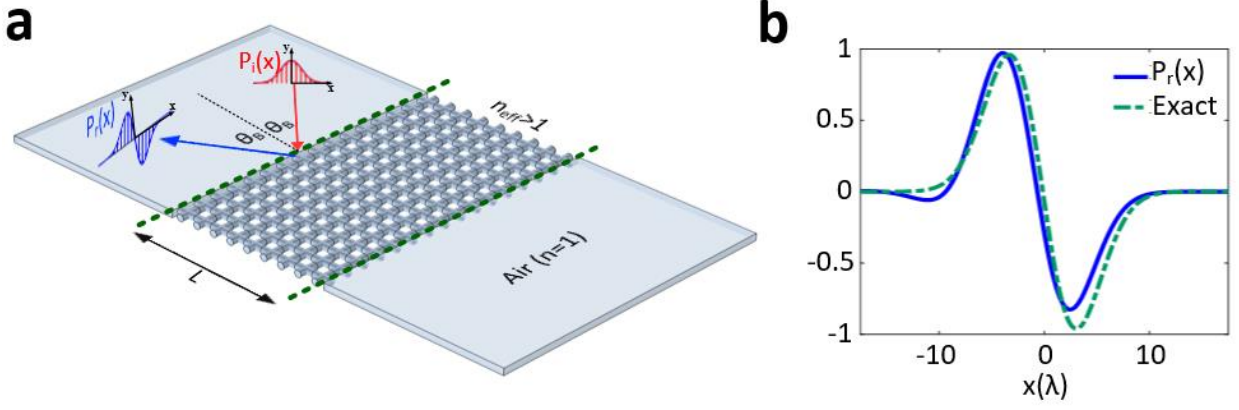
Figure 1.4: Acoustic spatial differentiator based on Green's function approach, a, An incident field impinges a half-wavelength high-index acoustic metamaterial, b, Corresponding transmitted field, following the spatial derivative of the incident signal [7].

signal. It is observed that the transmitted field has indeed a Gaussian distribution, as expected.

The idea of wave-based computing can also be implemented in other classical platforms such as acoustics. In the following, I demonstrate an acoustic analog computer, based on GF method, calculating the spatial derivative of the incident fields. The structure, shown in Fig. 1.4a, is composed of a metamaterial built from cross-shaped pipes, arranged at subwavelength scale. The meta-structure effectively acts as a high-index medium for acoustic waves, confining sound and guiding it. The length of the metamaterial (L) is designed to be half of the wavelength of the corresponding guided mode. As a result, the crystal behaves like a half-wavelength transmission line, allowing perfect matching between the input and the output signals. This leads to a dip (zero) in the reflection spectrum of the structure. Near this zero, the reflection spectrum of the structure can be approximated with a linear function, following the Green's function of a first order differentiator. As such, for those signals impinging the structure at this angle, the structure under investigation behaves like an analog spatial differentiator. In order to demonstrate this prediction, I calculated the reflected signal corresponding to a Gaussian incident pressure field and compared it with the spatial derivative of the incident signal (Fig. 1.4b).
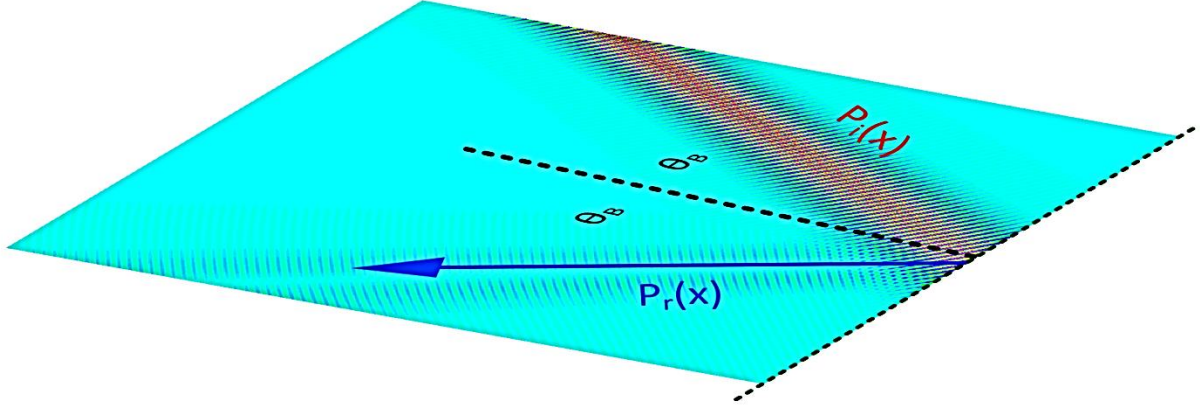
Figure 1.5: Field profiles of the incident pressure field ($P_i(x)$) and reflected field from the proposed acoustic spatial differentiator [7].

It is observed that the transmitted field is in perfect agreement with the spatial differentiation of the incident signal. Figure 1.5 illustrates the field profiles of the incident pressure field and the corresponding reflected field.

It should be noted that it is possible to perform more complex operations based on the acoustic spatial differentiator. Consider, for example, realization of the second order differentiation, an operator which is diversely found in important partial differential equations. There is a very simple, straightforward approach to realize a second order differentiator using the first order differentiator demonstrated here. One only needs to cascade two half-wavelength acoustic slab waveguides, each of which differentiates the incoming pressure field one time. The cascading process is conceptually represented in Figure 1.6a: an incident pressure field with the spatial distribution P_i strikes the boundary of a half-wavelength slab waveguide. Then, the resulting reflected field P_{r1}, which is in fact the spatial derivate of P_i, impinges another half-wavelength slab waveguide. The final pressure field P_{r2}, reflecting back from the second slab will therefore be the second order derivative of P_{r1}. To examine the performance of the corresponding second order differentiator, let us assume again that the input field has a Gaussian field distribution. The corresponding output field P_{r2} together with the exact second order derivative of the input field are
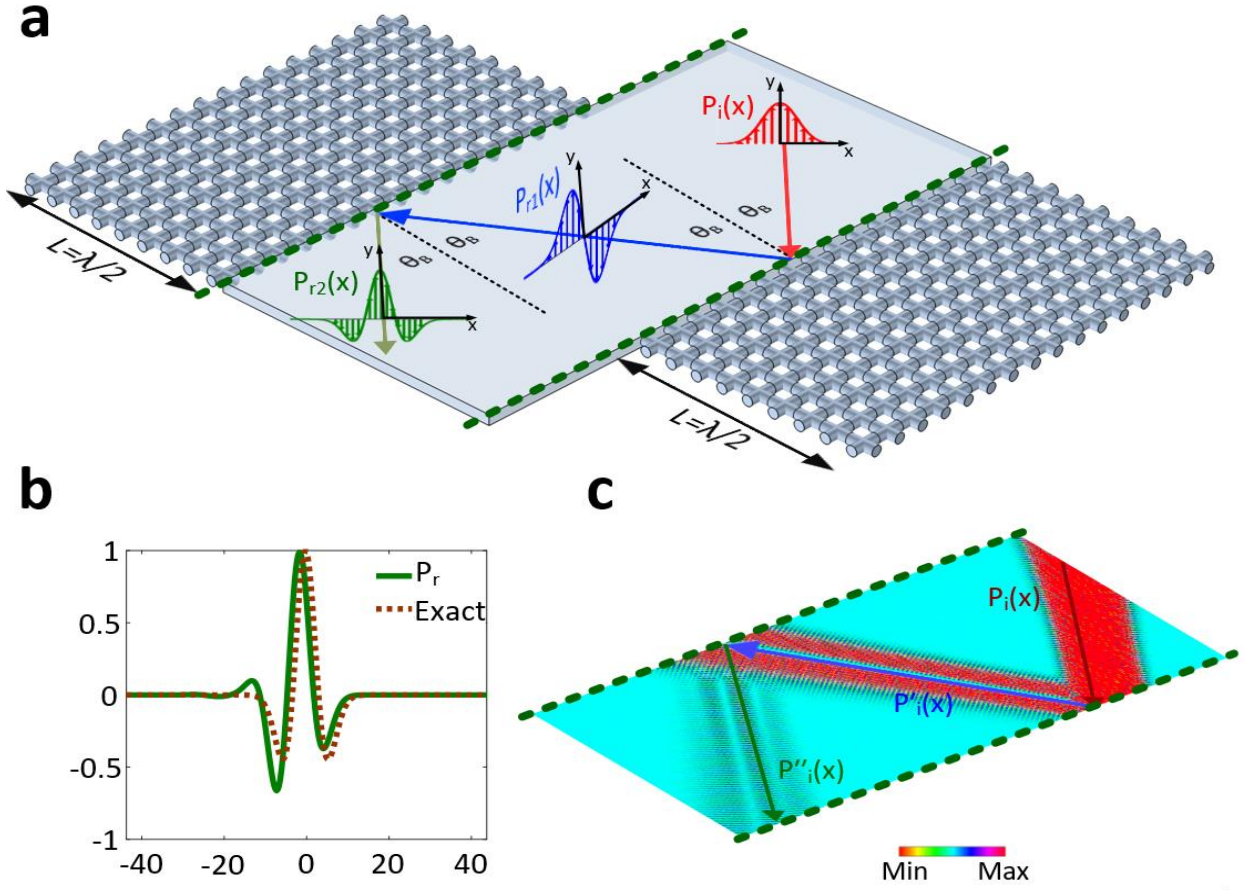
Figure 1.6: Demonstration of an acoustic computing system carrying out second order differentiation. a, Two half-wavelength slab waveguides are cascaded so as to realize an acoustic second order differentiator. b, Output signal of the computing system when the incoming field has a Gaussian-like distribution. The output field is in perfect agreement with the second order derivative of the incident beam. c, Field profile of the incident and reflected fields [7].

reported in Figure 1.6b, confirming the proper functioning of the system. Further insight into the computation process can be obtained by looking at the calculated field profile illustrated in the inset of Figure 1.6c. It should be noted that, in principle, cascading several differentiators reduces the amplitude of the resulting output drastically. This is because the differentiators work near the zero of reflection coefficient. Yet, the proposed cascading approach provides a straightforward and fully passive wavy to realize higher order operators.

The high-index acoustic metamaterials discussed previously can also be used as an analog integrator. Insets of Fig. 1.7 illustrate such a possibility, in which the prism coupling technique has been used to excite the guided mode of the high-index metamaterial. The excitation of this mode leads to a peak in the transmission spectrum of the configuration.
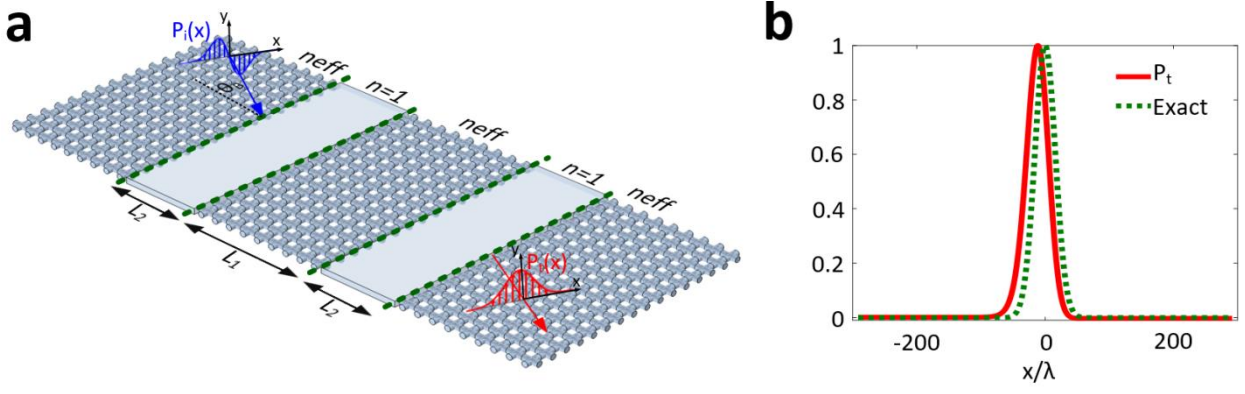
Figure 1.7: Acoustic spatial integrator based on Green's function approach, a, An incident field impinges on a half-wave-length high-index acoustic metamaterial, b, Corresponding transmitted field, following the spatial integration of the incident signal [7].

Near the resonance peak, the transmission spectrum of the system can be approximated with the Green's function of an ideal integrator, provided that the input signal has no DC component. As a result, the structure under analysis effectively behaves like an analog integrator. This is demonstrated in Figure 1.7b, in which I have reported the transmitted signal corresponding to a Gaussian derivative incident pressure field. It is seen that the transmitted field is indeed the integration of the incident signal, namely a Gaussian pulse.

1.3 Metasurface (MS) approach

Although GF method is a straightforward paradigm for realizing specific operators such as differentiation or integration, it does not provide a generic platform for carrying out arbitrary complex operations. The alternative strategy, the metasurface (MS) approach [4], on the other hand, enables realization of a wider range of operators. Fig. 1.8a shows the block diagram of an analog computing system based on MS technique. The system includes three sub-blocks: two graded index lenses, performing Fourier and inverse Fourier transforms, and a properly designed metasurface (MS) realizing the Green's function of the desired operator in the Fourier domain. The metasurface is composed of three sub-layers made from two alternating materials, namely silicon (Si) and AZO with properly designed inhomogeneous distribution of attenuation. The metasurface provides one with full control over phase and amplitude of the transmitted field, allowing one to realize an

arbitrary operator of choice. Figure 1.8b, as an instance, demonstrates the possibility of performing first order differentiator by appropriately tailoring the metasurface parameters.
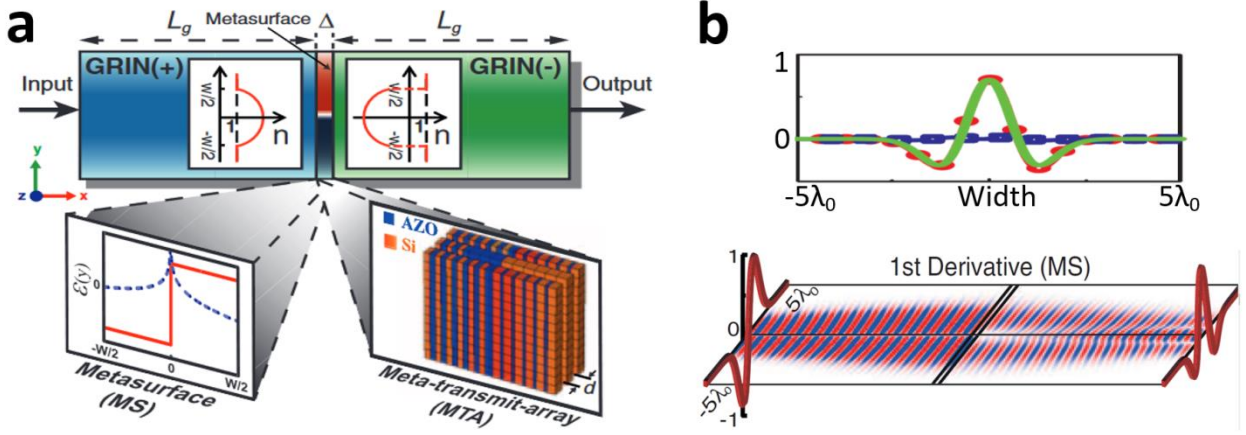
Figure 1.8: Analog computing based on metasurface approach, a, An optical metasurface designed to perform spatial derivative of the incident fields, b, Demonstration of the adequate functioning of the differentiator by exciting the differentiator with a signal having a Gaussian derivative distribution. As observed, the transmitted signal is the spatial derivative of the incident wave [3].

In this figure, a Gaussian derivative input signal is used to test the behavior of the differentiator. Inspecting the profile of the corresponding transmitted signal, one validates the proper functioning of the differentiator.

The metasurface approach has been employed in different platforms for performing analog computing. In plasmonics, for instance, Pors, et. al [8] proposed to implement differentiation and integration based on a plasmonic meta-reflect array consisting of silicon nano-bricks arranged on a silica layer (spacer). The space layer was placed on an optically thick metallic film (silver). The structure, shown in the inset of Fig. 1.9a, was illuminated by a circularly polarized light. By varying the sizes of the nano-bricks (L_x and L_y parameters), the amplitude and the phase of the corresponding reflected field could be manipulated independently, as observed in the inset of Fig. 1.9a. This enables realization of arbitrary operators, ranging from differentiation to integration and convolution.
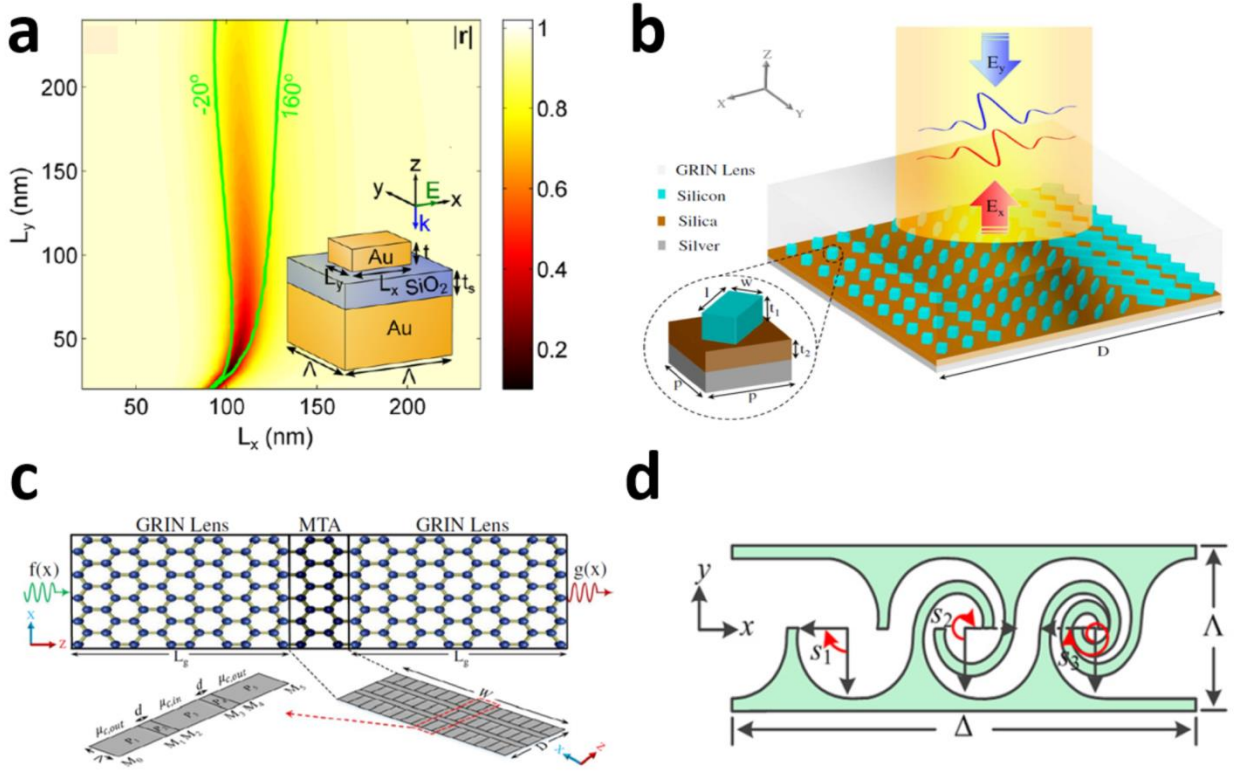
Figure 1.9: Analog computing based on the metasurface approach, a, A plasmonic optical metasurface, consisting of silver plates placed in top of a silicon dioxide substrate [8]. The metasurface provides one with a large control over both phase and amplitude of the transmitted field, enabling analog computation. b, An analog optical computer based on dielectric metasurface, offering high efficiencies [9], c, A reconfigurable analog optical computer based on a graphene meta-structure [11]. d, A single pixel of an acoustic metasurface, composed of three tapered labyrinthine components with varying spiral radians, performing analog signal processing [12].

Despite its applicability, the plasmonic computing system described above suffers from high absorption and low polarization conversion efficiency. In [9], Chizari, et. al circumvented these restrictions by proposing to perform computation based on a dielectric meta-reflective array, consisting of silicon nano-particles placed on top of a space layer (Figure 1.9b). Similar to the plasmonic case, by changing the width and lengths of the silicon nano-bricks, the metasurface can be manipulated to realize the Green's function of an arbitrary operator. As opposed to the plasmonic case, however, the structure provides much higher efficiencies. It is mainly due to its silicon-based inclusions that are almost lossless in the optical regime.

Both plasmonic and dielectric computing systems discussed share a common restriction. They are capable of performing "only one" specific functionality, depending on the metasurface design. The recent advances in the field of graphene physics [10], however, suggest a solution to tackle this restriction. In [11], Abdollahramezani, et. al. demonstrated the possibility of achieving a reconfigurable analog computing system by using a metasurface of graphene nano-ribbons with varying chemical potentials (Fig. 1.9c). By properly engineering μ_{in} and μ_{out}, a full control over both transmission amplitude and phase can be achieved, enabling realization of arbitrary operations in a fully dynamic manner.

Finally I note that the metasurface approach has also been implemented in acoustics to perform analog computational tasks. In [12], for instance Zuo. et. al demonstrated the possibility of performing mathematical operations based on a layered labyrinthine metasurface composed of three tapered labyrinthine components with varying spiral radians, enabling a full control over the phase and amplitude of the transmitted field. The metasurface structure is represented in Fig. 1.9d.

1.4   Applications

In this section, I describe two important application areas of wave-based analog computing systems, namely equation solving and image processing.

Equation solving: Most physical systems can be described by means of a system of differential or integral equations. Wave-based analog computers represent an ideal platform for solving such kinds of equations with ultra-high speeds, allowing us to unravel the behavior of the system very quickly. In order to indicate how waves can be leveraged for solving an equation, let us consider a simple resonator, shown in Fig. 1.10a. According to the coupled mode theory, the transfer function of the resonator can be approximated with

$$H(f) = \frac{A}{j(f - f_0) + f_0/2Q} \tag{1.1}$$
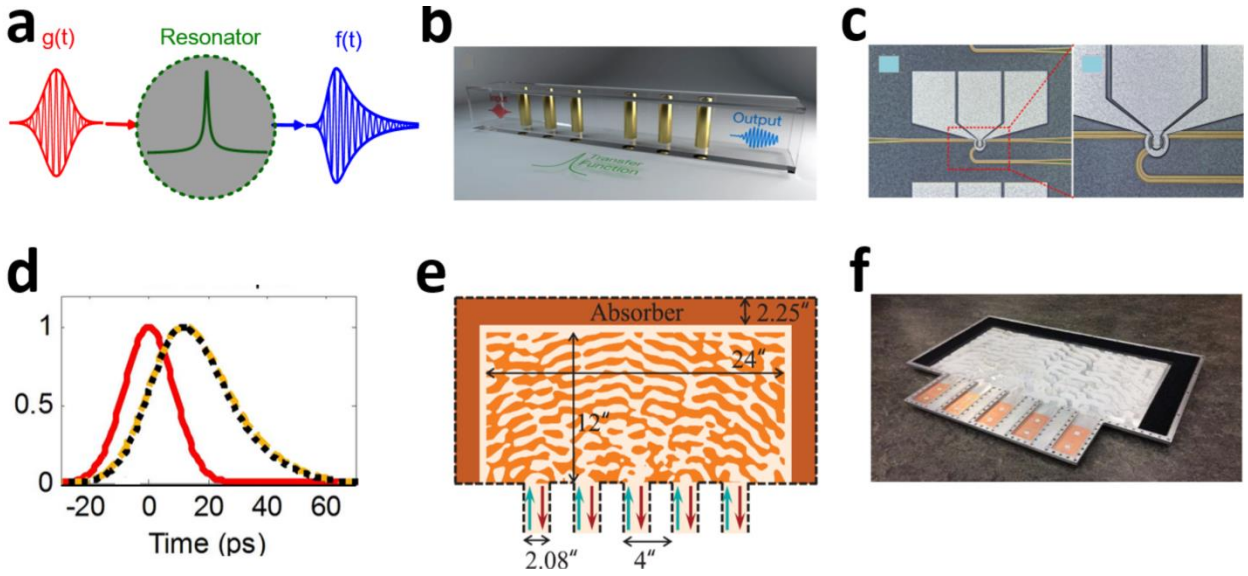
Figure 1.10: Solving mathematical operation based on wave-based analog computers, a, Equation solving based on a resonator possessing a Lorentzian spectral line shape. The transfer function of the resonator corresponds to a first order ODE in time domain. b, An instance of an analog equation solver based on the resonance tunneling through the Bragg band gap of a phononic crystal [172]. c, An instance of an analog equation solver based on the resonance of a micro-ring resonator, shown in the inset [13]. d, Measured output signal (yellow curve) of the mirroring resonator, corresponding to a Gaussian input pulse (red curve), compared with the ideal waveform (black curve). e, An inverse design metamaterial that solves integral equation. The metamaterial is composed of only two materials, air and low-loss polystyrene. f, Fabricated prototype of the metasurface of panel e [14].

where I have used the time harmonic convention $\exp(j2\pi ft)$, A is an arbitrary constant, and Q is the quality factor of the resonance. Now, if we consider a source term $\hat{g}(t)$ of the form $\hat{g}(t) = g(t)\cos 2\pi f_0 t$, its relationship with the output $\hat{f}(t) = f(t)\cos 2\pi f_0 t$ can be obtained via inverse Fourier transform of the transfer function (TF) of Eq. 1.1, leading to a first-order differential equation $f'(t) + \alpha f(t) = \beta g(t)$, with $\alpha = \pi f_0/Q$ and $\beta = 2\pi A$. What this simple analysis reveals is that any resonator, like the photonic Bragg crystal represented in Fig. 1.10b, can be viewed as an analog equation solver, solving the differential equation given in Eq. 1.1. This example also reveals the main advantages of analog computation over digital one: there is no need for converting the input signal $g(t)$ to a digital stream (and vice versa), and the computation is being performed in real time.

In [13], Yang used such a strategy to design and demonstrate an all-optical equation solver, solving first order differential equations with constant coefficient. The equation solver was based on a single silicon mirroring resonator, shown in Fig. 1.10c. The spectrum of the micro resonator could be drifted by changing the voltage applied to it, which corresponds to solving a first-order linear ODE with tunable constant-coefficients. Fig. 1.10d shows the measured output signal (yellow curve) of the mirroring resonator associated with a Gaussian input pulse (red curve), and compares it with the ideal waveform (black curve).

In terms of the classification framework described before, the equation solvers discussed in Figures. 1.10a-d are based on Green's function (GF) approach. The other strategy, i.e. the metamaterial approach, has also been used to perform equation solving. In [14], Estakhri, et. al proposed a metamaterial platform that solves arbitrary integral equations. The metamaterial, shown in Fig. 1.10e, is composed of only two materials, air and low-loss polystyrene. The inhomogeneity existing in the metamaterial structure can be described by an inhomogeneous relative permittivity $\varepsilon(x, y)$, allowing one to realize the kernel of the operator associated with the intended integral equation. Figure 1.10f shows the fabricated prototype of the metamaterial structure.

Image processing: Here, I describe the relevance of analog computing devices for detecting the edges of an image. One common and established technique for edge detection, known as zero crossing technique, relies on calculating the spatial derivative of the image in the direction(s) whose edges are intended to be detected. This can easily be carried out, for example, by exploiting the acoustic spatial differentiator demonstrated in Fig. 1.5. The corresponding edge-detector system, shown in Figure 1.11a, consists of a loudspeaker, a mask plane with locally engineered transparencies according to the shape of the desire image (shown in Figure 1.11b), a half-wavelength acoustic slab waveguide, and a microphone. The underlying working principle of the setup is the following. The sound generated by the loudspeaker is spatially modulated by the mask plane, creating the appropriate spatial field distribution corresponding to the image.
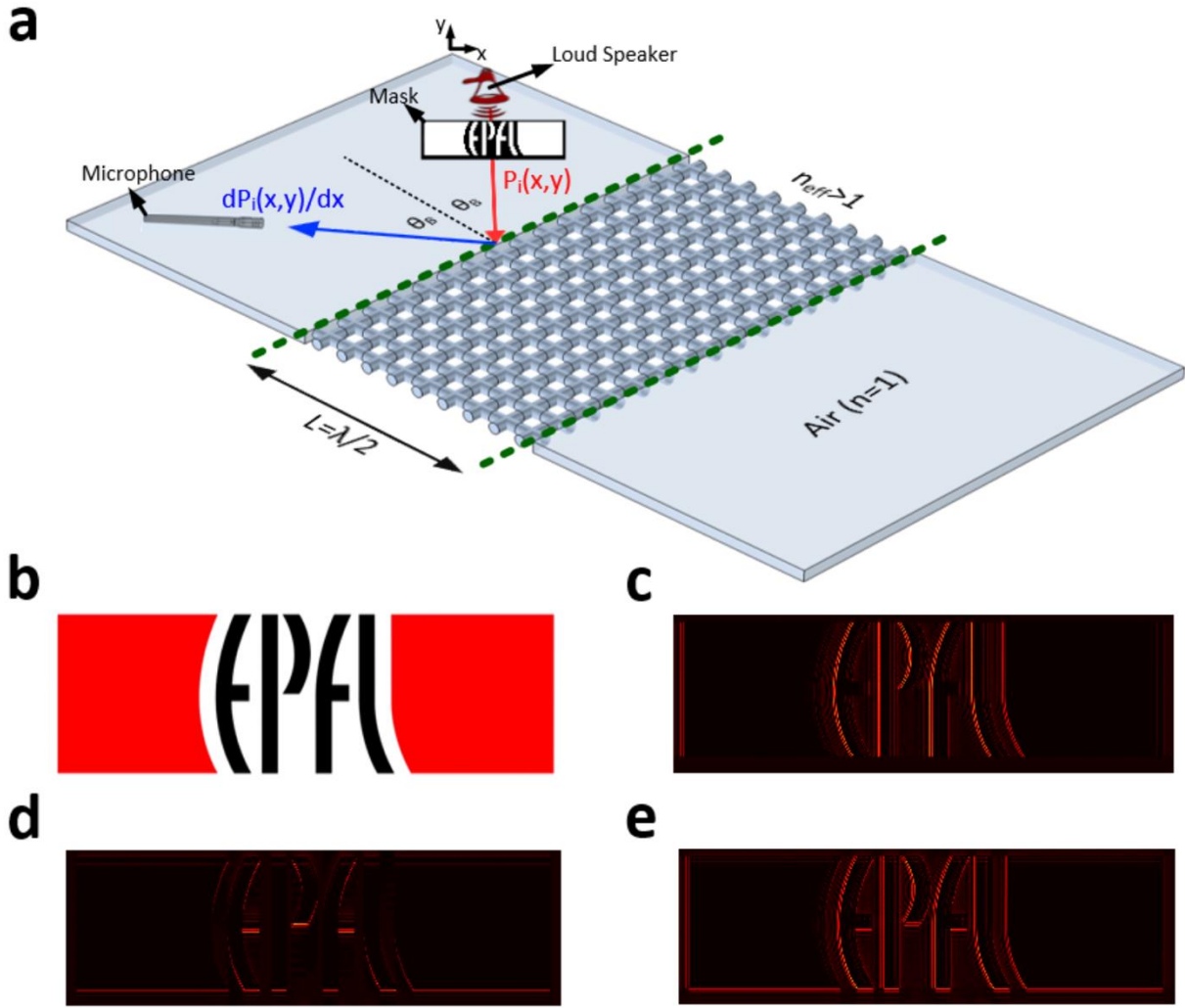
Figure 1.11: Edge detection of an image utilizing the proposed acoustic computing system. a, Acoustic computing setup designed for detecting the edges of an image: the setup consists of a loudspeaker as the source, a mask plane with locally engineered transparencies according to the shape of the image whose edges are intended to be detected, a half-wavelength acoustic slab waveguide differentiating the image, and a microphone to resolve the edge-detected image. b, Photograph of the image whose edges are aimed to be detected. c, Output edge-detected image when the slab waveguide differentiates the image along *x* direction: the vertical edges of the image have been detected. d, Same as panel c except that the slab differentiates the image in *y* direction, detecting its vertical edges. e, Resulting image when two differentiators differentiates the image in both *x* and *y* directions, revealing its horizontal and vertical edges simultaneously [7].

The resulting pressure field then impinges on the high-index acoustic slab and is spatially differentiated. The reflected field is then detected by the microphone so as to create the edge-detected image. Figure 1.11c reports the output edge-detected image. Notably, since differentiation is carried out along *x* direction, only the vertical edges have been resolved. The horizontal edges can also be detected by employing a similar setup, but with a slab waveguide carrying out

differentiation along *y*. The edge-detected image corresponding to the latter case is provided in Figure 1.11d. One may also consider two-dimensional edge detection by cascading two different differentiators and adding their resulting output fields to each other. Both vertical and horizontal edges of the images will then be detected in one measurement, as observed in Figure 1.11e.

1.5   Research objectives and organization of the thesis

While wave-based analog computers provide a well-established platform for carrying out ultra-fast computational tasks, they suffer from an important limitation, severely hindering their applicability in large scale applications. As opposed to digital signal processor for which the observational errors is negligible, analog computers do not provide high levels of reliability since they do not rely on digitalization and are very fragile to geometrical perturbations. To clarify this better, let us consider again the equation solver described in Fig. 1.12a, based on resonance defect tunneling through a Bragg band gap. Suppose that some disorder is added to the system by, for example, changing the position of the scatterers from their original position (Figure 1.12b). The corresponding transfer function can be significantly disturbed by the creation of disorder-induced modes, shifting its spectrum and introducing new resonating peaks. This leads to an output signal that has nothing to do with the desired solution. This sensitivity broadly restricts the applicability of analog signal processors in large scale applications, which may be prone to error accumulation.

Recently, it has been discovered that some specific types of structures, possessing a non-trivial topological order (e.g. topological insulators (TIs) [15]), can exhibit strong immunity against certain types and levels of imperfection. In this thesis, I investigate the possibility of leveraging topological insulators for alleviating the sensitivity of analog signal processors to disorder. More specifically, I realize a novel class of analog signal processors and computers whose functionality is protected by their non-trivial topological character, offering strong immunity against imperfections and geometrical tolerances. This is in sharp contrast to conventional analog computers for which the performance severely degrades upon introducing disorder.
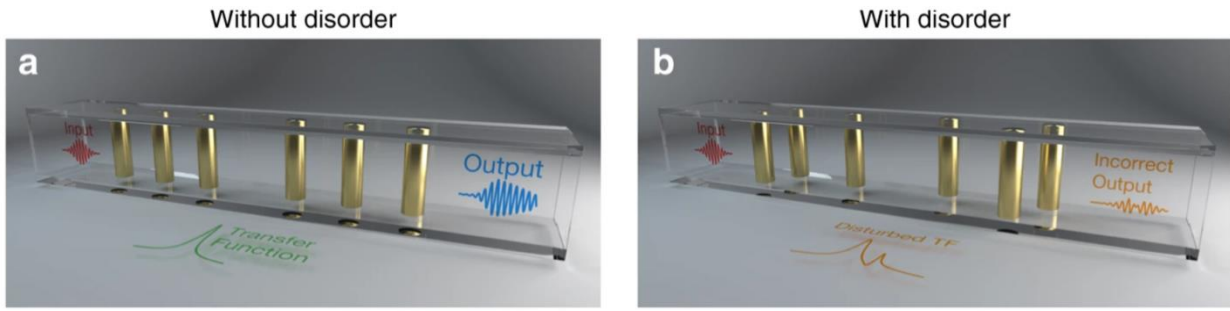
Figure 1.12: Sensitivity of analog signal processors to disorder, a, An analog equation solver based on resonance defect tunneling through a Bragg band gap, b, Some disorder is added to the system by randomly moving the positions of the scatterers. The corresponding transfer function can be significantly disturbed by the creation of disorder-induced modes, shifting its spectrum and introducing new resonating peaks. This leads to an output signal that has nothing to do with the desired solution [172].

The thesis is organized as follows: In Chapter 2, I provide a comprehensive overview of topological insulators in classical wave physics, surveying their realization in different platforms. I start with describing the simplest one-dimensional scenario, which is a model known as Su-Schrieffer-Heeger (SSH)model. I then move to two and three dimensions, reviewing analogues of quantum Hall and quantum spin Hall phases in classical systems, as well as other related ideas such as valley-selective waveguiding, Floquet topological insulators and Weyl semimetals.

In Chapter 3, I propose to perform analog signal processing tasks based on the edge modes of topological insulators. In particular, I demonstrate, both theoretically and experimentally, how the much-sought protection of the edge states of TIs allows one to alleviate the sensitivity of analog signal processors. I demonstrate this by achieving an important analog computational task, namely the resolution of linear differential equations, in an acoustic system that is protected by topology against large levels of disorder. I further discuss the possibility of generalizing the concept to electromagnetics and photonics.

In Chapter 4, I discuss the possibility of performing more complex computational tasks based on topological Fano resonances. By providing numerical and experimental results, I demonstrate that it is possible to achieve a novel class of sturdy Fano resonances, whose much-sought line shapes are topologically protected. Not only are such resonances relevant for carrying

out advanced signal processing operations, but also they open up exciting frontiers for a new generation of reliable wave-based devices such as including low-threshold lasers, perfect absorbers, ultrafast switches, modulators, accurate interferometers.

Going a step further, in Chapter 5, I demonstrate new class of topological analog signal processing systems in which disorder not only does not hurt the system, but is highly beneficial to it. More specifically, inspired by the recently proposed concept of disorder-induced topological insulators, I demonstrate that, in some topological systems with specific parameter ranges, strong randomness can be leveraged as a strategic asset to trigger analog functionalities of interest.

Finally, in Chapter 6, I summarize all of the achieved results and provide an outlook for future investigations.

Chapter 2   Topological wave insulators

Phases of matter are conventionally characterized using the so-called Landau's approach [16], classifying them in terms of the symmetries that break spontaneously at phase transitions. In the 1980's, however, the discovery of the quantum Hall effect, the quantum mechanical version of the classical Hall effect, suggested a fresh view on how to distinguish insulating phases using topological concepts [17]. This phenomenon, observed in a 2D electron gas subject to an out-of-plane magnetic field, indicated a completely different classification paradigm based on topology [18], a branch of mathematics concerned with the study of quantities that are preserved under continuous transformations.

Over the past few years, the topological classification of phases of matter has been extensively developed in order to understand the pivotal differences in the physical properties of electronic insulators, allowing for the distinction between ordinary and topological insulators (TIs) [19-15]. In the bulk, like any other ordinary insulator, a TI exhibits an energy band gap separating the valance and conduction bands. However, contrary to normal insulators, TIs support conductive gapless states flowing along their edges. These edge states are characterized by a special non-local integer number, known as a topological invariant or Chern number [21], which guarantees their presence and cannot change unless the insulating phase undergoes a discontinuous transformation that closes the band gap.

The edge modes of topological insulators can exhibit various interesting properties, the most important ones being the robustness of their existence, as well as their resilience to disorder-induced backscattering. Indeed, in order to destroy the presence of the edge states, topology requires that the bandgap is first closed, implying a stringent modification of the bulk properties, impossible with

localized edge imperfections or weak disorder. In addition, fermionic topological edge propagation is typically unidirectional or spin-locked, due to symmetry properties that are not broken by most impurity types. In electronics, these features have been established as a cornerstone for the realization of novel devices with a strong immunity against imperfections. For instance, new types of spin-resolved electronic devices have recently been proposed that, by taking the advantage of the robustness of TIs, perfectly separate the "read" current path from the "write" one [22,23]. This leads to not only a better output signal but also an improved reliability of spintronic systems.

Although discovered in quantum condensed matter systems, topological insulators are not intrinsically based on quantum phenomena and, as such, can be also obtained in classical systems. Indeed, the topological properties of insulators boil down to geometrical phase effects [24] that are, in principle, not related to the spatial scale or the physical nature of the system. In a pioneering paper [25], Haldane and Raghu proposed to extend the notion of Chern topological insulators to electromagnetic waves propagating in periodic media comprising magnetically biased ferrites. This sparked a search for classical applications of topological physics, in particular in wave phenomena of various kinds, from electromagnetics and photonics [26], to acoustics and phononics [27], as well as mechanics [28]. Classical wave systems can therefore benefit from a new kind of topologically inherited robustness to defects and disorder. In comparison with their fermionic counterparts, classical topological systems offer a larger control over their space and time properties, representing a particularly relevant platform to design, fabricate and detect all kinds of topological effects that may not be straightforwardly observed in condensed matter systems.

In this chapter, I provide a comprehensive overview of topological insulators in condensed matter systems and their classical analogues, and explain the important underlying physical concepts. I first explain the basics of topological insulators with the simplest one-dimensional scenario, namely the Su-Schrieffer-Heeger (SSH) chain. I then discuss the realization of this model in various physical platforms, including photonics and acoustics. I then move to two-dimensions

and survey wave analogues of quantum Hall insulators, quantum spin Hall insulators, valley-Hall insulator, and Floquet topological insulators.

2.1   One-dimensional topological insulators

The simplest form of topological insulating phases is a periodic one-dimensional discrete chain, known as the Su-Schrieffer-Heeger (SSH) chain [29-35], consisting of identical evanescently coupled resonators with alternating coupling coefficients. The unit cell of the SSH tight-binding chain, shown in Fig. 2.1, includes two resonators with identical resonance frequency coupled to each other with an intra-cell coupling coefficient K, whereas an extra-cell coupling coefficient J couples adjacent unit cells. Considering the associated coupled mode equations with the Floquet boundary condition applied to the lateral sides of the unit cell, one can write the system's Hamiltonian as

$$H = \begin{pmatrix} \omega_0 & K + J e^{jk_x a} \\ K + J e^{-jk_x a} & \omega_0 \end{pmatrix} \tag{2.1}$$

in which K is the intra-cell coupling coefficient, J is the extra-cell coupling coefficient, ω_0 is the resonance frequency of the resonators, k_x is the corresponding Bloch wave number and a is lattice constant. Depending on the values of K and J, the eigen-frequency spectrum of the Hamiltonian given in (2.1) is different. I first consider the case of $K = J$. Figure 2.2b represents the corresponding dispersion bands of this two-level system for $K = J = 0.1$. It is observed that the two dispersion bands of the system under study touch each other at the edge of the Brillouin zone, creating two point-degeneracies. These degeneracies represent an ideal condition for engineering the topological property of the system. More specifically, by introducing symmetry-lowering mechanisms, one may lift the degenerate points and open band-gaps belonging to different topological orders. In order to demonstrate such a possibility, I now consider the cases $K \neq J$. Fig. 2.2a and c represent the band structure of the chain for $K = 0.05 > J = 0.1$ and $J = 0.05 > K = 0.1$, respectively. It is observed that, in both cases, the band structure is gapped, indicating insulating phases. These insulating phases, however, can be of trivial or topological origin.
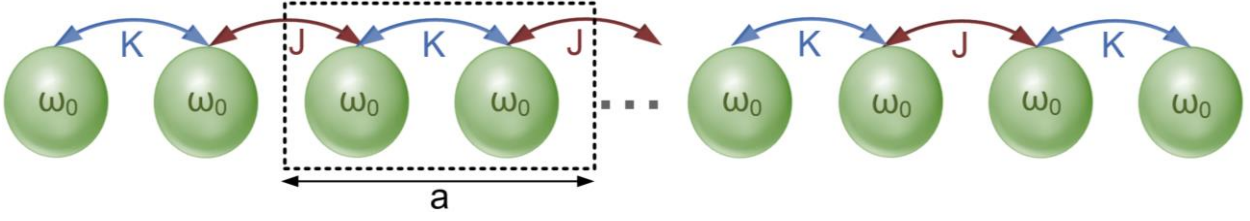
Figure 2.1: Su-Schrieffer-Heeger (SSH) tight binding toy model. The model consists of evanescently coupled resonators (with the resonance frequency of ω_0), coupled to each other with intra-cell coupling coefficients of K and extra-cell coupling coefficients of J.

In particular, while both cases ($K > J$ or $K < J$) look similar when only considering the band structure, i.e. the eigenvalues of the tight-bighting Hamiltonian, the topological difference resides in the associated eigenmodes, which shows a band inversion as one goes from the center to the edge of the Brillouin zone when the two cases are considered. In this one-dimensional case, the topology is defined from the mapping between the Brillouin circle to the space of 2×2 Hermitian Hamiltonian with chiral symmetry (also known as the equator of the Bloch sphere), and is characterized by a winding number [29]. The winding number W is defined as

$$W = 1/2\pi \oint_{BZ} A(k_x) dk_x \qquad (2.2)$$

in which BZ stands for the Brillouin zone, k_x is the Bloch wave number, and $A(k_x)$ is the so-called Berry connection, defined as

$$A(k_x) = \langle \Psi(x) | i\partial k_x | \Psi(x) \rangle \qquad (2.3)$$

where $\Psi(x)$ is the corresponding eigenstate. Note that this topological invariant is only well defined for chiral symmetric systems, meaning that all of the resonators should have the same resonance frequency. As a consequence, edge modes are robust to any disorder that preserves this symmetry and is not strong enough to close the band gap, which happens at the onset of Anderson localization. By calculating the winding number defined in Eq. 2.2, one realizes that the two cases of Fig. 2a and c are associated with different topological invariants. Namely, the case in which the values of extra-cell coupling coefficients are larger than the intra-cell ones corresponds to a non-zero winding number (winding number of 1). In reverse, when intra-cell coupling coefficients are
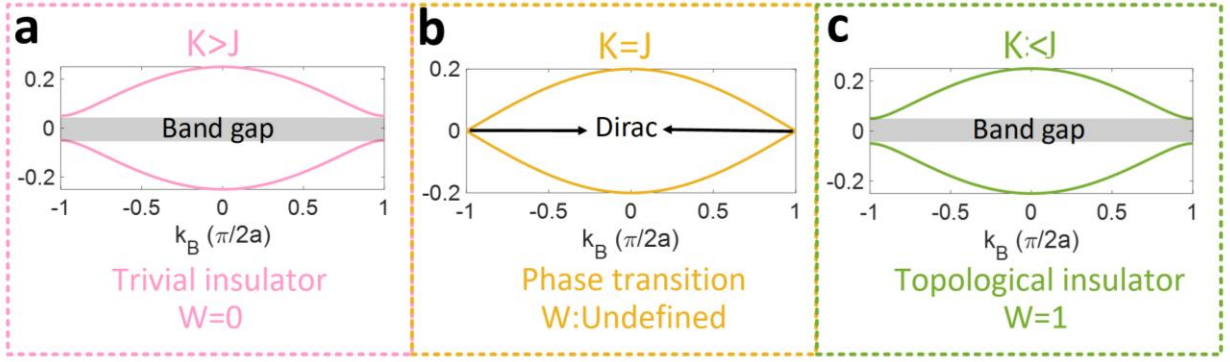
Figure 2.2: Band structure of the SSH model for a, $K > J$, b, $K = J$, and c, $K < J$, corresponding respectively to a trivial insulator, phase transition between a trivial and topological insulator, and a topological insulator. The topological index is defined as the winding (parameter W) of the Hamiltonian across the origin of the momentum space.

larger than the extra-cell ones, the system possesses a zero winding number, corresponding to a trivial topological index.

The most striking property of topological insulators is that they support gap-closing boundary states on their edges, when they form a boundary with another crystal having a different topological index. In order to probe these states, I have made an interface (see Fig. 2.3a) between two crystals, one with a zero topological order (i.e. $J < K$) and the other with a non-zero one ($J > K$). Fig. 2.3b represents the mode profile of the corresponding topological edge state. It is observed that the mode is confined to the interface between the two crystals. What is special about this edge mode is that its existence is only due to the difference between the topological indices of the two crystals on the left and right sides of the interface. Since the topological indices of the insulating phases are protected by chiral symmetry, the edge mode remains intact as long as this symmetry is preserved, even if one introduces some (symmetry preserving) disorder to the system. In order to demonstrate this, I calculated the corresponding transmission spectrum of the chain (see Fig. 2.3c). It is seen that the spectrum exhibits a mid-gap resonance corresponding to the zero-energy edge mode. Next, in Fig. 2.3d, I report the evolution of the line shape of this resonance as a function of disorder, applied to the coupling coefficients of the chain. It is observed that the zero-energy edge mode of the system is not significantly affected by the disorder.
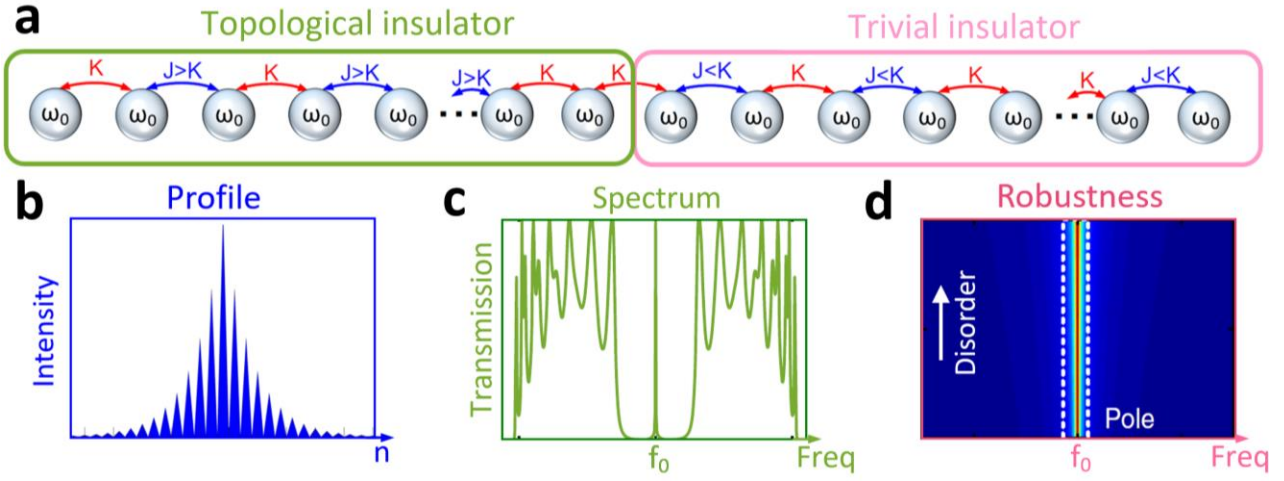
Figure 2.3: Topological edge modes of the SSH chain, a, An interface between a topological chain and a trivial one is made, b, Profile of the corresponding edge mode, confined to the phase transition interface between the two crystals, c, Transmission spectrum of the chain, showing a mid-gap resonance (at f_0) d, Evolution of the resonance line-shape of the topological zero energy mode as a function of disorder [172].

Considering the simplicity of the SSH model, this topological system has been implemented in a large variety of classical platforms. For instance, in [36] Parto, et. al, realized the optical version of the SSH structure making use of 16 identical coupled micro ring resonators fabricated on InGaAsP quantum wells (Fig. 2.4a). By changing the successive distances between the adjacent rings, the strengths of intra-cell and extra-cell coupling coefficients were engineered such that they give rise to a non-trivial topological phase. The inset of Fig. 2.4b illustrates the profile of the corresponding topological mid-gap state, which is pinned to the edge of the array, and exploited for robust lasing.

The SSH model has also been implemented in acoustics. In [37], Xiao, et. al. demonstrated the model in a one-dimensional sonic crystal consisting of cylindrical pipes with alternating cross-sectional areas, thereby mimicking the SSH scheme. Fig. 2.4c shows a photograph of the fabricated SSH structure, which consists of two one-dimensional arrays with different topological properties (different winding numbers), connected to each other to form a mid-gap edge state at the phase transition interface. The inset of Fig. 1d shows the profile of the edge mode.

The strong localization of the edge mode of the SSH array has been of particular interest for applications such as lasing [36,38], and sensing [39]. Yet, these kinds of edge modes cannot be used
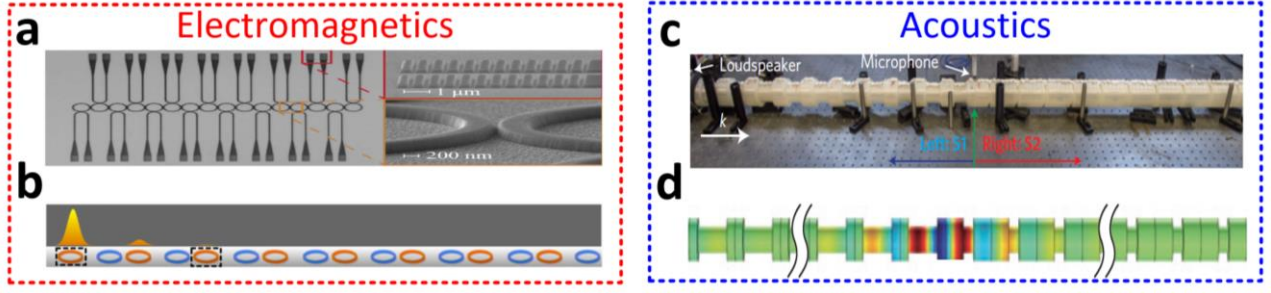
Figure 2.4: a,b, Realization of a one-dimensional electromagnetic topological insulator (based on the SSH scheme) in an array of coupled micro ring resonators fabricated on InGaAsP quantum wells [36], c,d, Realization of the SSH model in acoustics based on cylindrical waveguides with alternating cross-sectional areas, tuning the strengths of the coupling coefficients [37].

for waveguiding, as they are confined in zero dimensions. In the next part of this section, I move to two dimensions, describing 2D topological insulators whose edge modes are confined in one dimension and can therefore be leveraged for waveguiding and energy transport.

2.2   Chern Wave insulators

The integer quantum Hall effect (IQHE) provides the first example of a two-dimensional (2D) electronic topological insulator, in which the electrons flow unidirectionally along the edge of a 2D system subject to an out-of-plane external magnetic field [40]. Under these conditions, the Hall conductance takes the quantized values $\sigma_H = Ce^2/h$, in which h is the Plank constant, e is the electron charge, and C is an integer, corresponding to the topological invariant of the system. This quantity, also known as Chern number, is defined as a surface integral over the entire Brillouin zone (BZ), which is a torus in the three-dimensional momentum space. The integral is expressed as

$$C = \frac{1}{2\pi} \oint_{BZ} A(k)\, dk \, . \tag{2.4}$$

The parameter $A(k)$ in Eq. 2.4 is the so-called Berry curvature defined as $A(k) = \nabla_k \times [\langle \psi_n(k)|i\partial_k|\psi_n(k)\rangle]$, in which $\psi_n(k)$ represents the corresponding Bloch state on the nth band, k is the Bloch wave number, and ∂_k and $\nabla_k \times$ are the derivative and curl operators with respect to k, respectively. Since $A(k)$ is an odd function for time-reversal symmetric systems, the Chern number C is zero in the absence of an external magnetic field. Applying a bias odd under time reversal is

therefore essential to achieve a non-zero Chern number. Insulating phases with non-trivial topological order exhibit intriguing unidirectional charge transport along their edges. Note that in two dimensions the topology is defined by mapping the Brillouin torus to the entire Bloch sphere. In this picture, a twisted topology corresponds to an obstruction to define the Bloch wave functions over the entire Brillouin zone using a single phase convention [29].

Motivated by the developments of quantum Hall phases in electronic and quantum systems, the classical analogues of such phases were realized shortly thereafter. As mentioned earlier, Chern insulating phases are associated with a broken time reversal symmetry, which can be achieved in the context of microwave engineering using ferromagnetic materials. In [41], Wang et al. realized the electromagnetic version of quantum Hall phases based on gyromagnetic microwave materials. This achievement was obtained using a two-dimensional square lattice of ferrite rods, implemented
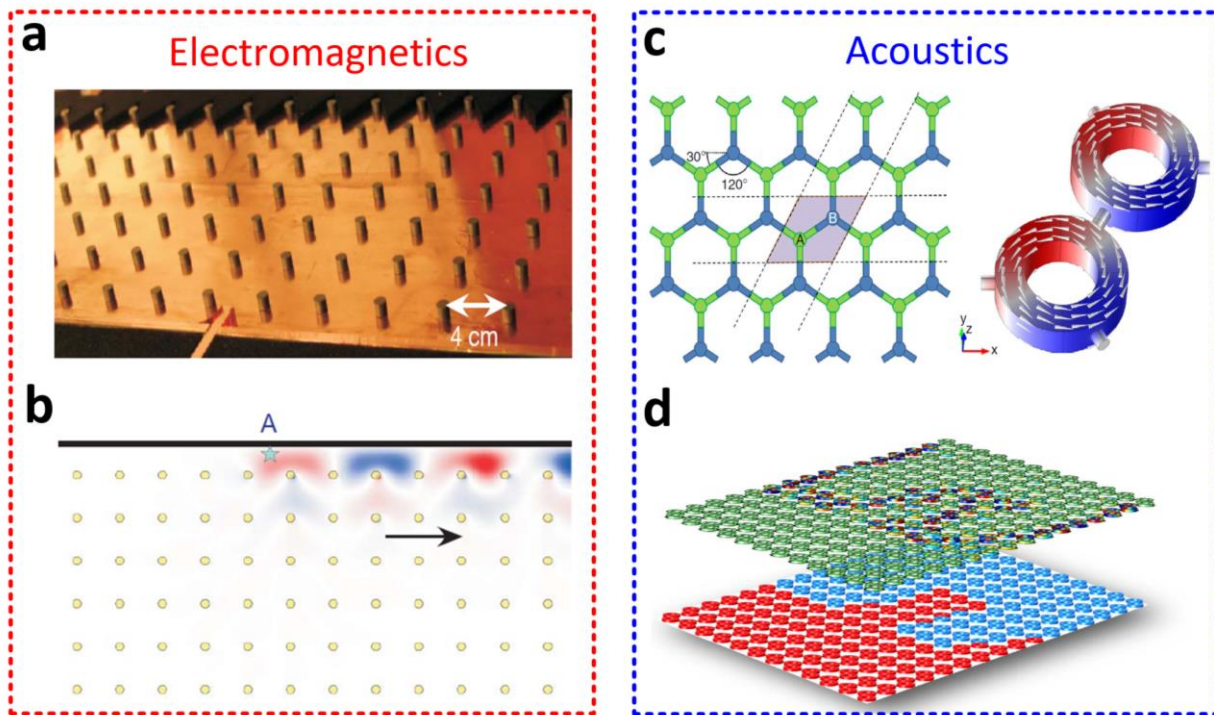
Figure 2.5: a,b, Two-dimensional Chern wave insulators were firstly realized in electromagnetics based on a square lattice of magnetically-biased gyromagnetic ferrite rods, implemented inside a microwave waveguide [41]. c,d, Realization of a Chern insulator in acoustics by constructing a hexagonal lattice of sonic ring cavities filled with rotationally biased moving fluids [42].

inside a microwave waveguide and biased with an external uniform magnetic field (see Fig. 2.5a). The one-way character of the topological edge mode was studied and demonstrated both in numerical simulations and experiments, as illustrated in Fig. 2.5b. Just a few years after this work, researchers extended such extraordinary phases to another field of classical wave physics, namely acoustics. This extension, however, required a different trick. In particular, since sound waves do not interact efficiently with magnetic fields, a different strategy was employed to break time-reversal symmetry, namely the use of fluid motion [42]. In 2015, two independent works proposed the use of rotating fluids to realize acoustic analogues of quantum Hall phases [43,44]. Khanikaev, et. al proposed an acoustic analogue of magnetically-biased graphene (Fig. 2.5c), based on a honeycomb network of ring cavities filled with rotationally moving fluids [43]. Yang, et. al [44] suggested a different approach employing a triangular array of rotating cylinders in a viscous fluid. The corresponding edge modes of such topological phases provide the unique opportunity of reflection-less routing of sound along irregularly shaped pathways, as seen in Fig. 2.5d. Such backscattering-immune classical wave transport has been confirmed in a series of related proposals, as well as experimental investigations.

2.3 $\mathbb{Z}_2$ topological insulators

While Chern insulators require breaking of time-reversal symmetry, there exists another type of topological insulators in two-dimensions that, on the contrary, preserve time-reversal symmetry. In electronic condensed matter systems, these insulators are referred to as $\mathbb{Z}_2$ topological insulators, and typically emerge in the presence of spin-orbit coupling, as in the quantum spin-Hall effect [45,46]. Such phases can be pictured as systems in which two time-reversed copies of a quantum Hall phase with opposite spin-sector restricted Chern numbers coexist without coupling. One of the copies corresponds to electrons with positive spins, and its time-reversed version to electrons with negative spins. As a consequence, two topological edge modes exist that propagate in opposite directions, carrying electrons with different spins. In presence of time-reversal symmetry, Kramers theorem prevents any interaction between the two spin species, which cannot backscatter

at non-magnetic defects. Since they do not require time-reversal symmetry breaking, $\mathbb{Z}_2$ topological insulators may appear easier to realize than the Chern class in electronic systems. Yet, realization of these phases in classical systems is not quite straightforward for two principal reasons. First, photons (and also phonons), associated with electromagnetic (or sound) waves, are spin-less particles. Second, they are bosons, for which the time-reversal operator $\mathcal{T}_b$ squares to $+1$, and not to -1, as for electrons, which are fermions ($\mathcal{T}_f^2 = -1$). Interestingly, the relation $\mathcal{T}_f^2 = -1$ is essential for Kramers theorem to hold, guaranteeing truly independent spin subspaces. In order to solve these issues, one must construct a pseudo-spin degree of freedom and "augment" bosonic time-reversal with another symmetry operation $\mathcal{C}$ such that $(\mathcal{C}\mathcal{T}_b)^2 = -1$, enforcing Kramers degeneracy when both $\mathcal{C}$ and $\mathcal{T}_b$ are preserved [47-61]. Note that this procedure potentially makes the classical version of a $\mathbb{Z}_2$ topological phase less robust than its electronic counterpart, since not only $\mathcal{T}_b$ breaking defects induces backscattering for the topological edge modes, but also defects that break $\mathcal{C}$.

For electromagnetic waves, described by Maxwell equations, spin can be emulated by leveraging electromagnetic duality as an additional symmetry $\mathcal{C}$, by enforcing $\varepsilon = \mu$. This assumption indeed restores the duality of Maxwell's equations, creating two degenerate, time-reversed (pseudo)spins. By properly introducing some bi-anisotropy (coupling the TE and TM components of the field), the two spins of such a system can undergo opposite interaction terms emulating spin-orbit coupling. This leads to the realization of an electromagnetic analogue of the quantum spin Hall effect, based on the combination of duality and time-reversal symmetry. Employing this scheme, in [62] Khanikaev et.al. proposed the photonic analogue of the quantum spin Hall effect in a hexagonal lattice of a spin-degenerate dual metamaterial, composed of split ring resonators with strong bianisotropic behavior (Fig. 2.6a). The inset of Fig. 2.6b represents the profile of one (spin up) of the corresponding edge modes. Defects in the form of sharp turns that do not couple the two polarizations do not break duality nor time-reversal symmetry, hence they do not reflect the spin-locked topological edge modes that can seamlessly be routed along an irregularly

shaped topological interface. Note that the duality condition $\varepsilon = \mu$ is hard to achieve as dispersive effects might make it difficult to guarantee this condition over a broad frequency range. Nevertheless, it can be enforced with very good approximation over a couple of crystal bands, which is more than sufficient for observing exceptionally robust edge wave transport along bent paths. A similar idea has been implemented for Lamb waves over a structured plate based on accidental degeneracy between two Lamb modes with distinct polarizations [63].

In fluid acoustics, the explained strategy to achieve quantum spin Hall phases is not readily functional due to the absence of a polarization degree of freedom. An alternative strategy to emulate acoustic pseudospin is to exploit the symmetry of a crystal lattice, in which case $\mathcal{C}$ is some sort of crystalline symmetry operation. Such a scheme, based on six-fold rotational symmetry, was initially proposed by Wu and Hu in 2015 in a triangular lattice of hexagonal resonators [64], and implemented in a variety of platforms including microwaves [65], photonics [66-70], elastic [71-74] and acoustics [75-78]. Figures 2.6c and 2.6d indicate an example [78] that employed this strategy to
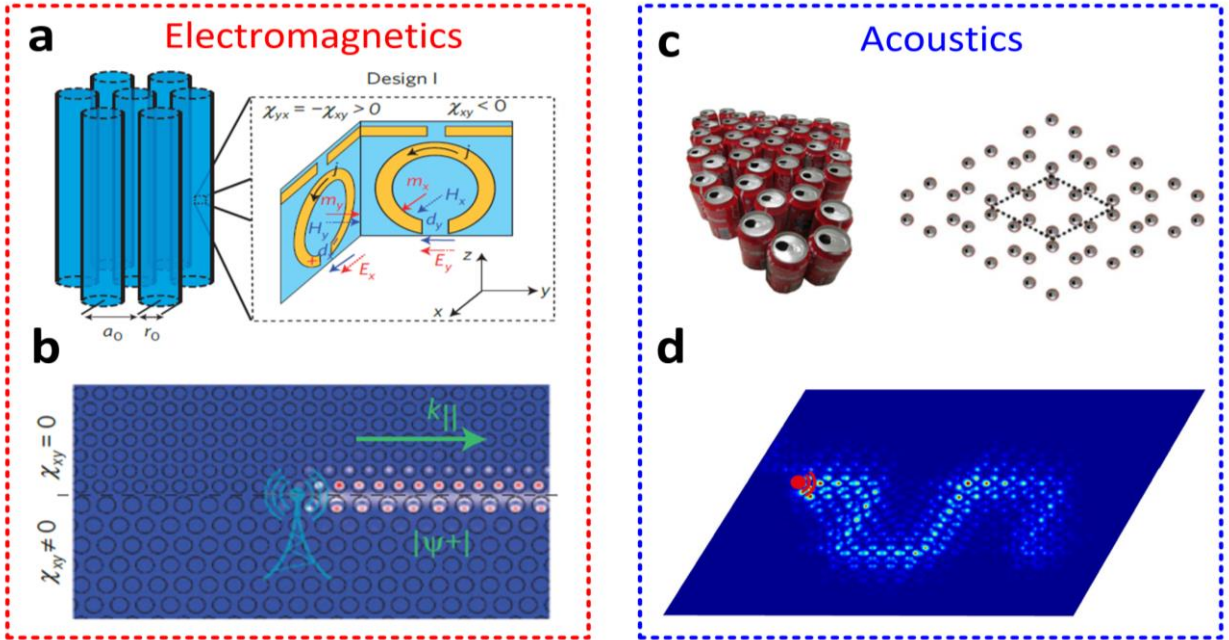
Figure 2.6: a,b, Photonic realization of $\mathbb{Z}_2$ wave insulating phases based on a metamaterial with strong bi-anisotropic behavior, providing TE and TM polarized modes with opposite spin-orbit forces [62]. c,d, A strategy to achieve acoustic versions of $\mathbb{Z}_2$ insulators is to expand the primitive unit-cell of a hexagonal lattice to a larger one, and use the corresponding folded degenerate Bloch states as pseudo-spins [78].

induce a deeply subwavelength acoustic topological edge mode in a subwavelength sonic crystal made of Helmholtz resonators (simple soda cans) arranged in a modified hexagonal-like lattice. The unit cell of the crystal is shown in the inset of Fig. 2.6c. Fig. 2.6d illustrates how the edge mode of such a crystal propagates with good transmission along a path involving sharp turns. Note that all symmetry-based strategies for emulating pseudo-spins only allow for an approximate realization of Kramers degeneracy, which only holds at the high-symmetry points of the Brillouin zone (Γ point in the case of six-fold rotational symmetry). Thus, the quantum spin-Hall Hamiltonian can only be emulated "locally" around this degenerate point, as may be proven by performing a first order $k.p$ approximation of the Hamiltonian around the point [64]. However, pushing the $k.p$ analysis beyond first order reveals that Kramers degeneracy is quickly broken away from the high symmetry point, on the same band. Direct use of topological quantum chemistry concept [79] has also confirmed the
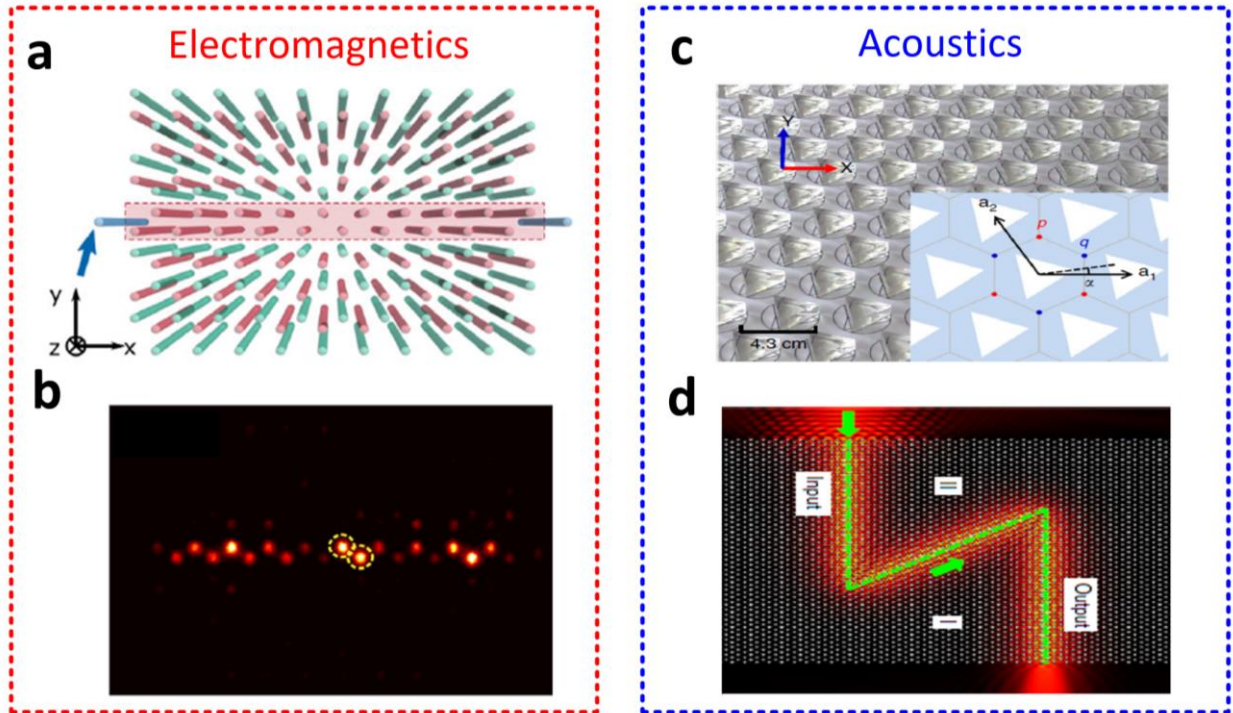
Figure 2.7: a,b, Photonic realization of Valley Hall insulators based on a zigzag edge domain wall of two crystals with opposite on-site potential organizations [91], c,d, Realization of Valley Hall insulators in a sonic crystal consisting of triangular polymethyl methacrylate rods positioned in a triangular-lattice with opposite rotation angles [92].

impossibility of rigorously defining a global $\mathbb{Z}_2$ topological invariant on the entire band structure of these systems. Rigorous quantitative statistical analysis of the edge mode robustness against different kinds of defects [80] is also consistent with an incomplete, or approximate, level of topological protection. Nevertheless, designs based on exploiting crystalline symmetries work very well in practice, and they allow easy and direct exploitation of topological ideas based on lattice symmetries regardless of the physical platform, still leading to relatively large robustness to backscattering.

2.4 Valley Hall wave insulators

In a hexagonal lattice in which the Dirac degeneracy has been lifted by breaking inversion symmetry, modes belonging to the K and K' valleys, which are obviously time-reversed images of each other, also carry some form of chirality or pseudospin [81-90]. Locally, these time reversed pairs, which correspond to valleys created by opening time-reversed Dirac cones, carry an opposite Berry flux. Since inversion also changes the K valley into the K' one, one can construct two crystals, inversion images of each other, with valleys having opposite Berry fluxes oriented along a given direction. Then, interfacing these two crystals along this direction amounts to requiring an abrupt sign change of the Berry flux, which requires the band gap to close at the interface, supporting the necessary presence of an edge mode.

Similar to the schemes based on six-fold rotational symmetries, it is not possible to define a global topological invariant over the full Brillouin zone, and this type of edge modes is not globally topological. However, it remains exceptionally robust to Valley-preserving defects, like Z shaped turns. In [91], Noh, et. al. leveraged the valley degree of freedom to realize photonic analogues of the Valley Hall effect in a two-dimensional honeycomb lattice of optical waveguides, shown in Fig. 2.7a. The red and green waveguides in the figure possess different refractive indices, corresponding to two different on-site potentials that allow inversion symmetry breaking. The valley edge modes were obtained along a zigzag edge domain between two crystals with opposite on-site potential configurations (referred to as AB and BA). Under this condition, the edge modes cross the band

gaps formed at the proximity of high-symmetric corners of the Brillouin zone. The inset of Fig. 2.7b illustrates the profile of one of the corresponding edge modes. Interestingly, the valley Hall waveguiding scheme also works in other types of lattices, when some form of operation that flips the sign of the Berry curvature is used. For instance, topological valley Hall phases were realized in acoustic systems based on symmetry-breaking rotations of the crystal constituents. In [92], Lu et. al built a sonic valley Hall waveguide with a sonic crystal consisting of triangular polymethyl methacrylate rods (Fig. 2.7c) positioned in a triangular lattice with a rotation angle α with respect to the vector a_1. When $\alpha = n\pi/3$, the crystal supports two-folded Dirac cones at the edge of the Brillouin zone. These degeneracies are lifted for other rotation angles, opening a frequency band gap. By connecting two different domain walls with opposite rotation angles of $\alpha = 10°$ and $\alpha = -10°$ corresponding to opposite Berry fluxes, a pair of valley chiral edge states, counterpropagating at the interface, can be realized. Such edge modes can be utilized for guiding of sound along an irregularly shaped zigzag path (Fig. 2.7d). This method is transposable to other wave platforms, including highly dispersive ones, such as gravity-capillary waves at the surface of liquids [93].

2.5   Floquet topological insulators

Another conceptually distinct route to achieve electronic topological phases without the need for an external magnetic field is to apply a time-periodic modulation in the electron potential energy or hopping rate [94-96]. For the first time, in the field of semiconductor physics, it was shown [97] that, by irradiating a trivial semiconductor quantum Well with a time periodic microwave wave, a new of topological phase transition can be achieved. Such kinds of topological phases, dubbed as Floquet topological insulators, support helical edge modes in their quasi-energy spectral gaps.
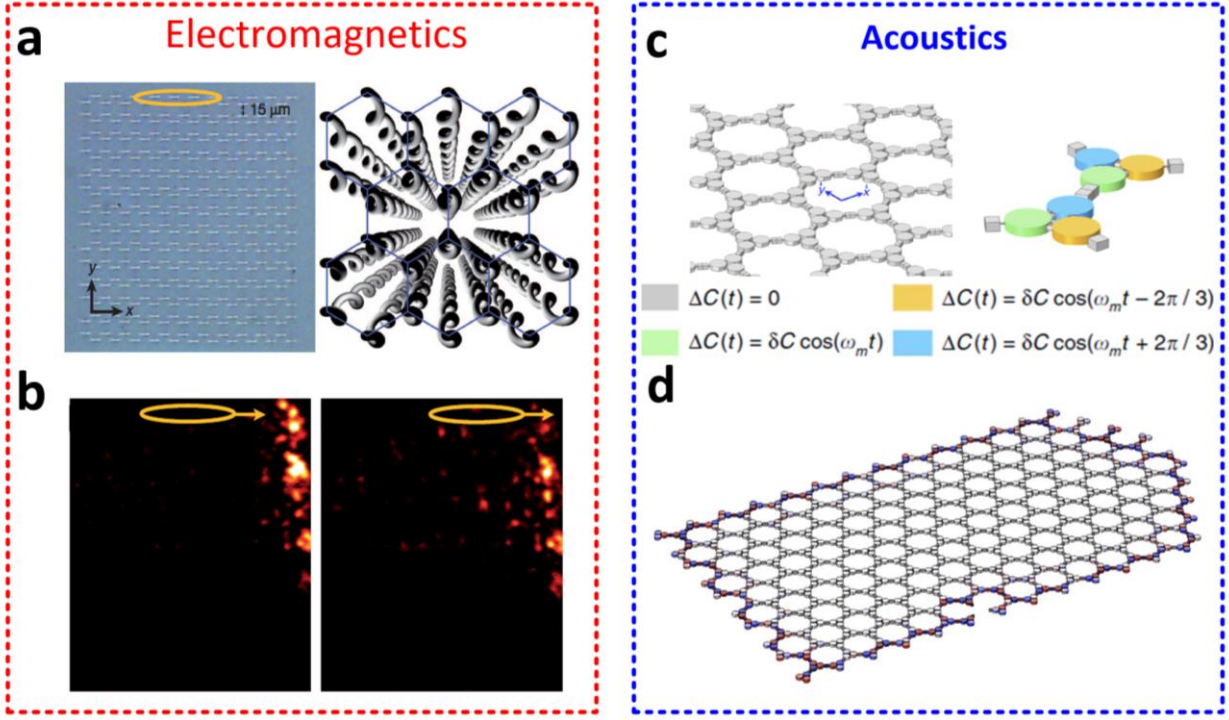
Figure 2.8: Floquet topological insulators, a,b, Photonic analogue of Floquet topological insulator, based on a graphene-like lattice of helical waveguides evanescently coupled to each other. The helicity of the waveguides breaks z-reversal symmetry [97], c,d, Realization of Floquet topological insulator based on a hexagonal lattice of acoustic trimers, with capacitances modulated in time in a rotating fashion [105].

Parallel to the developments of Floquet topological insulators in condensed matter systems, these concepts were extended to classical systems [97-103]. In [104], Rechtsman, et. al., demonstrated the photonic analogue of a Floquet topological insulator, based on a graphene-like lattice of helical waveguides evanescently coupled to each other, as seen in Fig. 2.8a. The dynamics of beam diffraction through such a lattice is described by the Schrödinger equation, where the distance of propagation takes the role of time. The helicity of the waveguides breaks z-reversal symmetry, effectively emulating time-Floquet modulation. Within the framework of this mapping, the quasi-band structure of the crystal becomes identical to the one of a Floquet topological insulator, supporting one-way edge states that are protected from scattering at the lattice corners. Shown in Fig. 2.8b is the profile of such edge modes when a beam excites the array from its top edge.
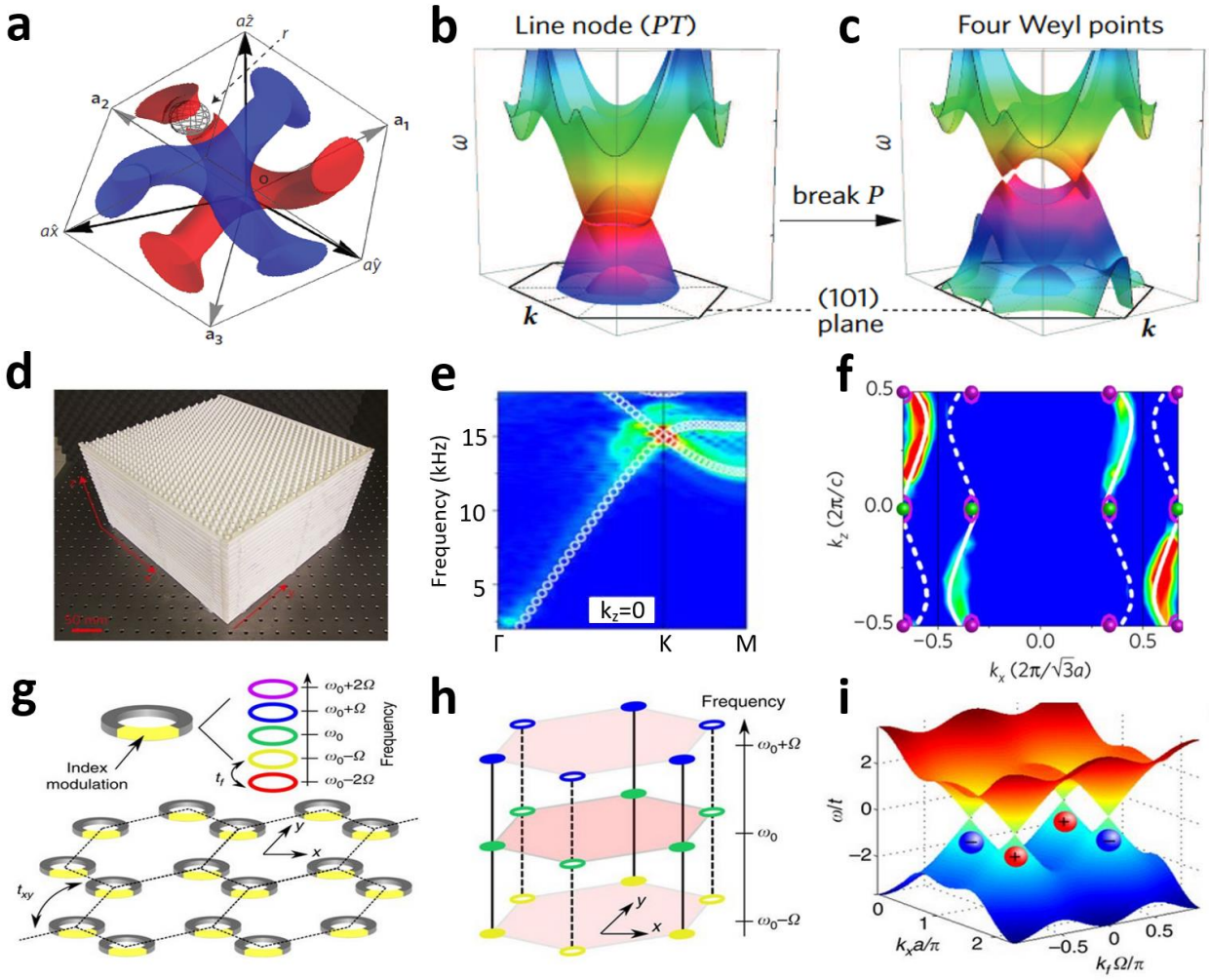
Fig. 2.9: Classical wave Weyl semimetals, a, Realization of electromagnetic analogues of topological semimetals based on a crystal with the real-space unit cell shown in the panel [131]. b, Band structure of the corresponding nodal semi metallic phase. c, By breaking the spatial inversion symmetry of the unit cell, the line node degeneracy splits into four distinct Weyl points. d, Realization of acoustic topological semimetals in a chiral phononic crystal fabricated using a layer-stacking strategy [132]. e, Band structure of the crystal shown in panel f, exhibiting Weyl degeneracy at K point. f, Fermi arc surface of the corresponding topological states. g, Exploring Weyl physics in a planar 2D geometry. h, The discrete resonance modes can be pictured as a periodic lattice in the synthetic frequency dimension. i, Band structure of the crystal in the 3D synthetic dimension, exhibiting four Weyl points [134].

Time-Floquet topological insulators have also been proposed in acoustics. In [105], Fleury et. al. demonstrated a time-Floquet topological insulator based on a hexagonal lattice of acoustic trimers, whose acoustic properties were periodically modulated in time in a rotating fashion, with uniform handedness throughout the lattice (Fig. 2.8c). Fig. 2.8d shows the profile of one of the corresponding edge states, flowing across the boundary of a finite piece of such a crystal. Compared to acoustic quantum Hall phases discussed before, such kinds of topological states are potentially

more practical as they do not rely on moving background fluids. It is also worth mentioning at this point that a one-to-one correspondence between time-Floquet systems and unitary scattering networks can be made, where the unitary network scattering matrix takes the role of the Floquet time-evolution operator over a period [106,107]. This has allowed an easier experimental exploration of different Floquet topological phases (Chern or anomalous [108]), in both photonics and acoustics [109-111].

2.6 Topological insulators in three dimensions

In 2D periodic systems, the topological phases usually stem from point degeneracies in the band structure, which are known as Dirac cones. By properly tuning the system parameters, the degenerate points can be lifted, and bandgaps can be opened, leading to different topologies. In three dimensions, possible band degeneracies are line nodes [112-116], Weyl points [117-125], or 3D Dirac points [126-130]. Weyl points are particularly interesting as they behave as sources of Berry flux, carrying a Chern number of ± 1, which manifests itself as topological surface states along any surface interface enclosing a non-vanishing number of Weyl charges.

Following the discovery of Weyl and nodal semimetals in the field of semiconductor physics [118], Lu et. al. theoretically realized both line nodes and Weyl points in a gyroid photonic crystal made from germanium high-index glasses [131]. Shown in Fig. 2.9a is the real space unit cell of the 3D periodic structure. By applying proper symmetry-breaking perturbations to the unit-cell of such structure, a nodal line degeneracy was realized. This is accomplished by replacing part of the gyroids with air spheres, as seen in the inset of Fig. 2.9a. Fig. 2.9b represents the 3D band structure of the crystal cut at (101) plane. A closed line degeneracy around the Γ point is observed in the band structure of the crystal. Note that the area enclosed by this line degeneracy can be controlled by the strength of the applied perturbation, that is, the radius of the air-sphere. The unit cell of the crystal in Fig. 2.9a respects parity-time (PT) symmetry. A possible approach to achieve Weyl point degeneracies is to break the PT symmetry of the unit cell. In fact, it is known that a line node degeneracy creates either a frequency band gap or a set of paired Weyl points upon breaking

PT symmetry. The PT symmetry of the double gyroid crystal can be broken by, for example, removing one of the air spheres of the two gyroids. By doing so, the line node degeneracy splits into four Weyl degenerate points along ΓN and ΓH directions, as observed in the band structure of Fig. 2.9c.

Weyl and nodal semimetals have also been realized in acoustic systems. In [132], Xiao, et. al. theoretically discussed the possibility to achieve Weyl and nodal semimetals in a lattice made of coupled sonic resonators and waveguides, described by a tight-binding model involving chiral interlayer couplings. A few years later, phononic Weyl phases were experimentally demonstrated [133] in a chiral phononic crystal, fabricated using layer-stacking technique. The insets of Fig. 2.9d represent the corresponding 3D structure, consisting of stacked layers of air-filled hollow waveguides, connected to each other via spiral hollow channels. Such a structure supports two pairs of Weyl points at $k_z = 0$ and $k_z = \pi/a$. Shown in Fig. 2.9d is the measured band structure of the crystal for $k_z = 0$, from which the existence of Weyl points at the high-symmetry point K is apparent. The inset of Fig. 2.9e shows the Fermi arcs of the corresponding surface states.

Despite the fact that topological semi-metallic phases have successfully been demonstrated in photonic and phononic systems, the realization of such phases is often challenging due to their 3D structure. Based on the notion of synthetic dimension, in [134] Lin, et. al. explored Weyl physics in a planar 2D geometry, consisting of on-chip ring resonators with dynamic modulation of the refractive index, as sketched in Fig. 2.9g. Each resonator supports a set of discrete modes, whose resonance frequencies are equally spaced. These discrete resonance modes can therefore be pictured as a periodic lattice in the synthetic frequency dimension. Together with the real dimensionality of the crystal, this third, synthetic frequency dimension forms a three-dimensional space (Fig. 2.9h). By modulating the refractive indices of the ring resonators properly, one can then appropriately couple these modes to each other so as to achieve Weyl point degeneracies in the 3D synthetic space formed by the two spatial dimensions and the frequency axis. The inset of Fig. 2.9i shows the corresponding Weyl points and their charges.
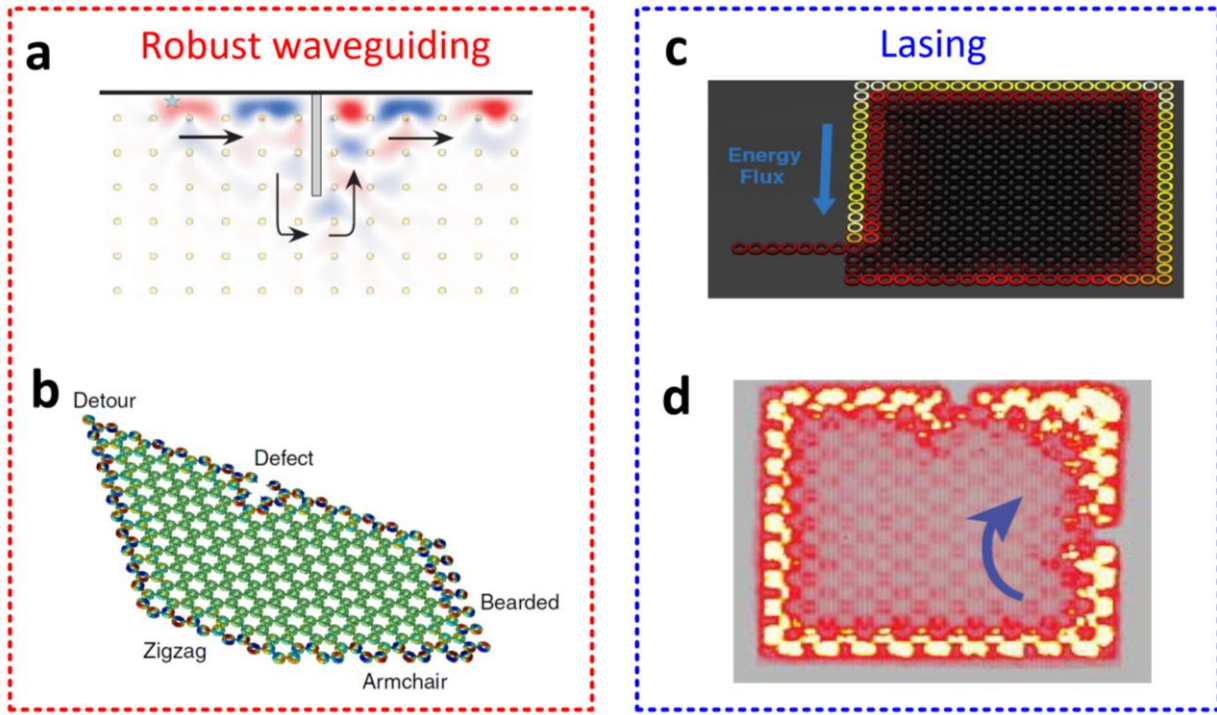
Fig. 2.10: Applications of classical wave topological insulators, a, In contrast to any ordinary type of waveguide, the edge mode of the topological insulator discussed in Fig. 2.5a smoothly flows around a PEC obstacle without backscattering, enabling robust guiding of electromagnetic energy [41,43]. b, Reflection-less guiding of sound waves using the topological insulator discussed in Fig. 2.5c. Despite the presence of several types of defects on the way of the edge mode, it flows along the perimeter of the crystal with almost perfect transmission. c, Theoretical realization of the lasing action from the edge mode of a topological insulator, based on an aperiodic topological array of micro ring resonators. d, Experimental demonstration of the lasing action. The lasing mode shows strong robustness to disorder [151].

2.7   Applications of topological wave insulators

In the previous sections, I discussed various implementation topological phases of matter in classical wave physics. However, the impact of this area of research has been rapidly expanding in the realm of practical applications of these concepts, as I detail in this section. In particular, I discuss the two important technology-oriented applications areas of topological wave insulators.

Robust waveguiding: One important application of classical topological insulators is robust guiding of energy over arbitrary paths [135-143]. An ordinary waveguide exhibits a bi-directional type of dispersion. On the contrary, the gapless edge states of Chern wave insulators possess a frequency dispersion with only positive (or negative) slope (or group velocity). Consequently, waves (light or sound) cannot couple to any backward state when it reaches an imperfection, and

does not backscatter. Suppose that a perfectly conducting obstacle is placed on the way of the electromagnetic wave propagating along the edge of the topological system discussed in Fig. 2.5a. While this normally induces strong reflection in any ordinary waveguide, the topological insulator lets the electromagnetic energy flow around the PEC with almost perfect transmission (Fig. 2.10a). Such fascinating property has also been proposed in acoustics for reflection-less guiding of sound waves. Fig. 2.10b shows how the edge mode of the acoustic topological insulator discussed before ideally travels along an interface involving various types of defects and detours. This is in stark contrast to ordinary acoustic waveguides in which two subsequent defects always create Fabry-Pérot interferences and, more generally, impedance matching issues.

Lasing: Another promising application of topological insulators is single-mode robust lasing [144-151]. In [151], Harari, et.al, theoretically proposed to achieve the lasing action from the edge modes of a topological insulator. The realization was based on an aperiodic topological array of micro-ring resonators, which was one of the basic platforms explored for achieving photonic topological insulators [152,153]. The aperiodic nature of such structure creates an artificial gauge field, allowing one to have edge states analogues to quantum Hall phases without the presence of any external magnetic field. By providing gain to the resonator cavities located on the perimeter of the crystal, the lasing action from such a configuration was demonstrated, as seen in Fig. 2.10c, and demonstrated to be robust to spin-preserving defects.

Based on these theoretical findings, in [154], Bandres et. al. experimentally verified the lasing action from such kind of a system. Fig. 2.10d represents the lasing from such a topological system. Remarkably and consistent with the topological nature of the structure, the lasing mode and its slope efficiency shows a strong immunity against disorder. It should be noted that the edge modes of this topological lasing systems are time-reversal symmetry preserved and, as such, are not truly unidirectional. Yet, there are reports [145] on the realization of topological lasers with a broken time-reversal symmetry, enabling truly unidirectional and non-reciprocal lasing action at telecommunication wavelength.

Finally, I note that, while I discussed a few important technology-oriented applications of topological wave insulators in this section, there exists a large variety of reports on other relevant applications, including switching [155], lensing [156], negative refraction [157], sensing [158], beam splitting [159], mode locked fiber lasers [160], delay lines [161], frequency converters [162], and interferometers [163].

2.8   Conclusions

In this Chapter, I reviewed recent advances in the field of classical-wave-based topological insulators. I discussed different kinds of topological insulators in one, two, and three dimensions, from the simplest SSH toy model to complex Weyl semimetals. I provided several representative examples of their realizations in various physical platforms, from photonics to phononics. I also reviewed some of the most interesting application areas of topological insulators in modern engineering.

As I explained in this chapter, the most important advantage of topological systems compared to ordinary ones is their strong robustness to geometrical tolerances and imperfections. This much-sought feature represents a perfect platform for enhancing the reliability of analog signal processors. In the next Chapter, I will demonstrate the relevance of topological insulators for achieving this.

Chapter 3   Topological   analog   signal processing

This chapter is a modified version of the materials reported in [172].

3.1   Introduction

Considering the limitations of digital signal processors, it is neither reasonable nor affordable to use DSPs for performing specific, simple computational tasks such as differentiation or integration, equation solving, matrix inversion, edge detection and image processing. Therefore, the old idea of all-analog computing and signal processing has been recently revived, driven by the development of cost-efficient nanofabrication techniques and promising related advances in ultrafast optics. By going beyond the aforementioned restrictions of DSPs, wave-based computational systems have inspired numerous exciting applications including analog computing [164-171], equation solving [172], optical image processing [172-176], optical memories [177], and photonic neural networks [178].

As I explained in Chapter 1, ASPs still suffer from one important limitation compared to DSPs. While repeating the same operation always gives rise to the same result when using DSPs (which is enabled by available error-finding algorithms and protocols in digital systems), analog signal processing is often accompanied with considerable observational error caused by the extreme sensitivity of ASPs to changes in environmental and structural parameters [179].

In this chapter, I demonstrate the possibility of enhancing the reliability of ASPs by leveraging the unique immunity of topological insulators against imperfection. More specifically, I demonstrate a topologically robust wave-based analog system that can solve linear differential equations in time-domain.
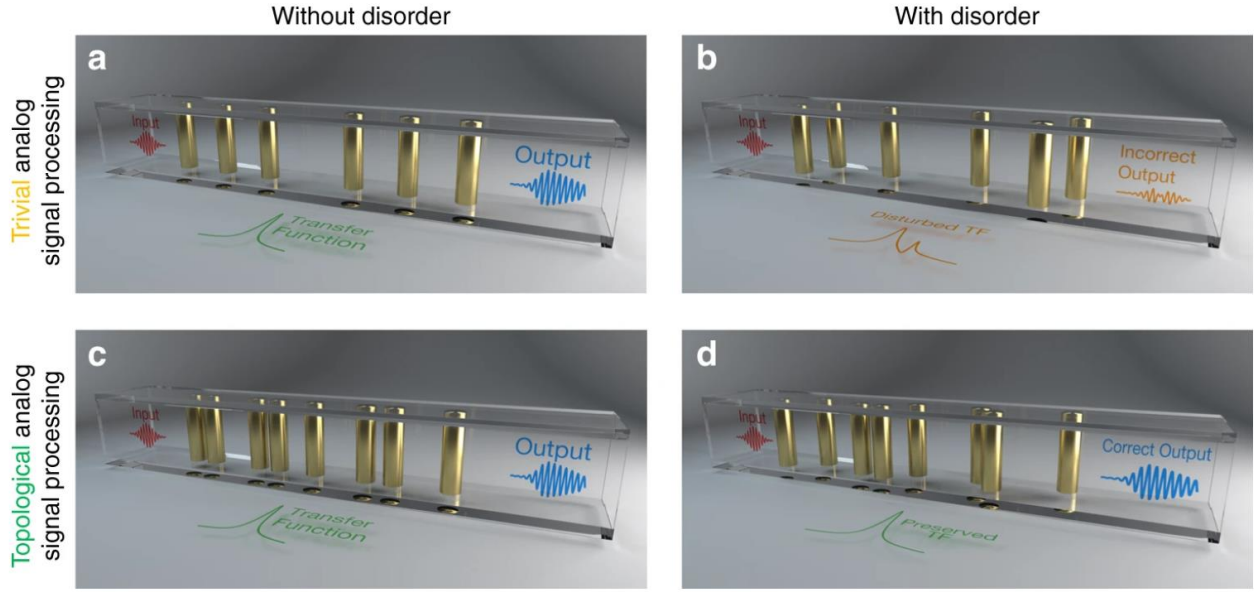
Figure 3.1: Robust topological analog signal processing. a, A first-order differential equation solver is constructed from resonant tunneling through a crystal defect. The output signal is the solution of the differential equation associated with the transfer function of the system. b, In the presence of geometrical defects, like slight position shifts, the signal processing functionality achieved with the trivial equation solver of panel (a) is completely destroyed. c, To make the signal processing robust, I propose instead to build the target transfer function of the system from resonant tunneling through a topological edge mode. d, Markedly different from the trivial equation solver of panels (a) and (b), the output of the topological solver is left totally unaffected by the disorder [172].

3.2 Topological analog equation solver

Let us consider again the analog equation solver, shown in Fig. 1a, based on the resonance defect tunneling through a Bragg band gap. Near the resonance frequency of the resonance mode, the spectral line shape of the system can be approximated with

$$H(f) = \frac{A}{j(f - f_0) + f_0/2Q} \tag{3.1}$$

in which A is an arbitrary constant, and Q is the quality factor of the resonance. As I explained in Chapter 1, in time domain $H(f)$ corresponds to a first order differential equation of the form $f'(t) + \alpha f(t) = \beta g(t)$, with $\alpha = \pi f_0/Q$ and $\beta = 2\pi A$. This analysis illustrates the possibility to realize an analog equation solver by engineering the spectral characteristics of a resonator.
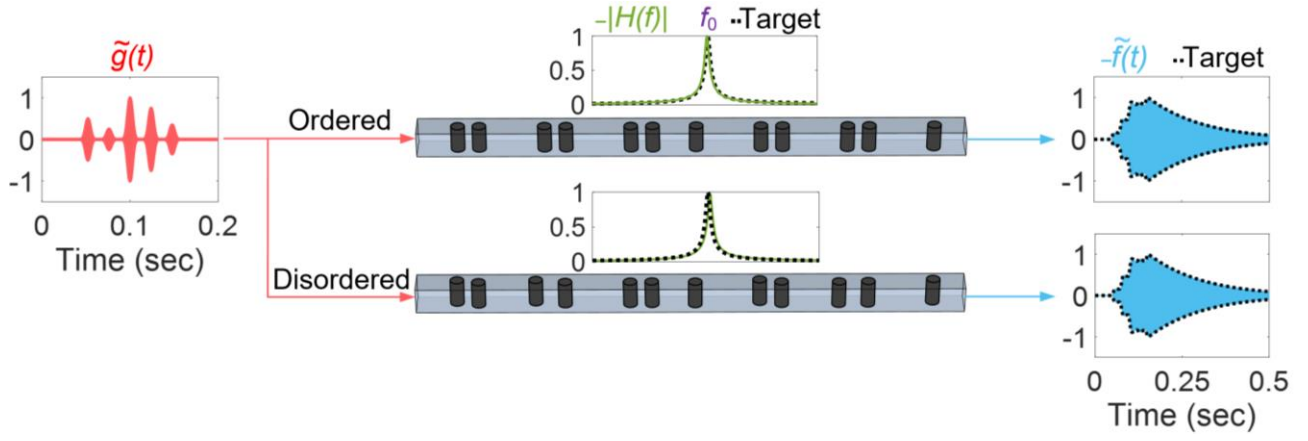
Figure 3.2: Numerical demonstration of the topological differential equation. An arbitrarily chosen signal envelope $\hat{g}(t)$ is applied to the input of the topological equation solver. The transfer function of the system $H(f)$ (green line), which reproduces exactly the mathematical target defined by the equation (dashed line), is not affected by the presence of disorder (bottom path). Thus, the envelope of the output signal $f(t)$ matches exactly the solution even in the presence of disorder [172].

When adding geometrical imperfections to the system (Fig. 3.1b), however, the transfer function of the system is significantly disturbed by the creation of disorder-induced modes, shifting its spectrum and introducing new resonating peaks. This leads to an output signal that has nothing to do with the correct solution.

What I propose is instead to form the same transfer function, but out of resonant transmission through a topological edge mode, whose existence is guaranteed by the nontrivial topologies of the surrounding bulk insulators. Figure 3.1c depicts such a solution based on two insulating lattices with supposedly different topologies, inspired by the Su−Schrieffer−Heeger (SSH) scheme, described in the previous Chapter. Like the previous case, when the input signal $g(t)$ (modulated at f_0) is applied to such system, the output signal envelope $f(t)$ is equal to the solution of the desired differential equation. However, the topological equation solver can be immune to disorder, since the presence of a single mid-gap interface mode can be guaranteed by bulk-edge correspondence (Fig. 3.1d).

To test this idea on a realistic system, I designed a topological first-order linear differential equation solver for airborne audible acoustic signals. The topological ASP system is based on sonic topological insulators inspired by the SSH scheme, obtained from solid cylinders placed in a pipe of

square cross-section, as in Fig. 3.1c,d. The topological interface is designed to provide a resonant mode at $f_0 = 2254\ Hz$, with $A = 1$ and $Q = 0.5\ f_0$, aiming at solving the differential equation $f'(t) + 2\pi f(t) = 2\pi g(t)$. The transfer function of the system, calculated by three-dimensional full-wave finite-element calculations in the frequency domain, is compared to the target transfer function in Fig. 3.2 (green and dashed curves in the middle inset), revealing their perfect agreement. Now, consider an input signal $\hat{g}(t)$ with an arbitrarily chosen time envelope $g(t)$ to be injected into the waveguide (Fig. 3.2a, left). The corresponding output signal $\hat{f}(t)$ is then calculated by convoluting $\hat{g}(t)$ with the impulse response of the system, obtained from $H(f)$ (I also verified the results by direct simulations in the time domain). Comparing the envelope of the resulting output signal $f(t)$ (blue line) to the exact solution of the intended differential equation (dashed line) reveals that the topological ASP system is indeed solving the equation as sound propagates through the system. Now, I add some disorder to our equation solver by randomly shifting the position of the cylinders (average position shift is 18% of lattice period in any direction) and repeat the same procedure in the bottom panel of Fig. 3.2.
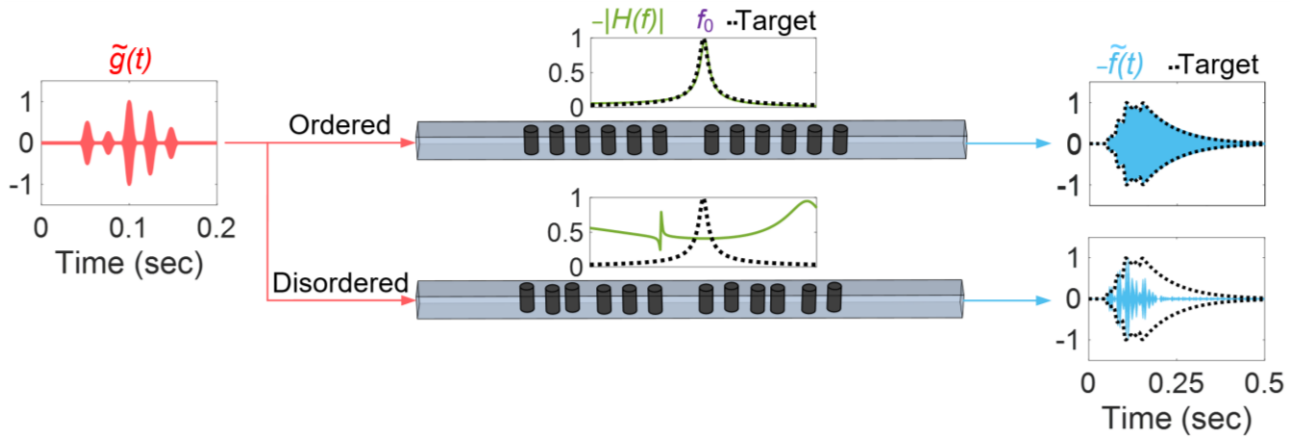
Figure 3.3: Numerical demonstration of a trivial equation solver, based on resonance defect tunneling through a Bragg band gap. (Top) When no disorder is introduced to the system, it returns the solution of the ODE equation aimed at solving. However, as opposed to the topological case, when the system is disordered, the presence of disorder-induced localized states creates spurious peaks and shifts the transfer function of the system, which makes it deviate from the targeted transfer function (dashed line) [172].

It is observed that, despite the relatively large level of disorder, the transfer function $H(f)$ has been left almost unaffected. Hence, the corresponding output signal $f(t)$ still corresponds to the solution of the desired differential equation, confirming the high robustness of the proposed equation solver.

To demonstrate that the much-sought robustness of the proposed topological equation solver is indeed linked to its topological nature, I repeat the analysis for a topologically trivial equation solver, which is based on a resonance induced by defect-tunneling through a Bragg band gap. As confirmed in Fig. 3.3, such resonating system is also capable of solving the first-order differential equation. The transfer function $H(f)$, and the output signal $\hat{g}(t)$ is however severely affected when imparting imperfections of similar strength to the sample (position shifts have the same magnitude as that of topological case). This clearly affirms the superiority of topological ASPs over trivial ones. Notice that these observations remain true, regardless of the temporal shape of the input signal $g(t)$. This is verified in the results of Figure. 3.4, in which I have considered a Gaussian-type time
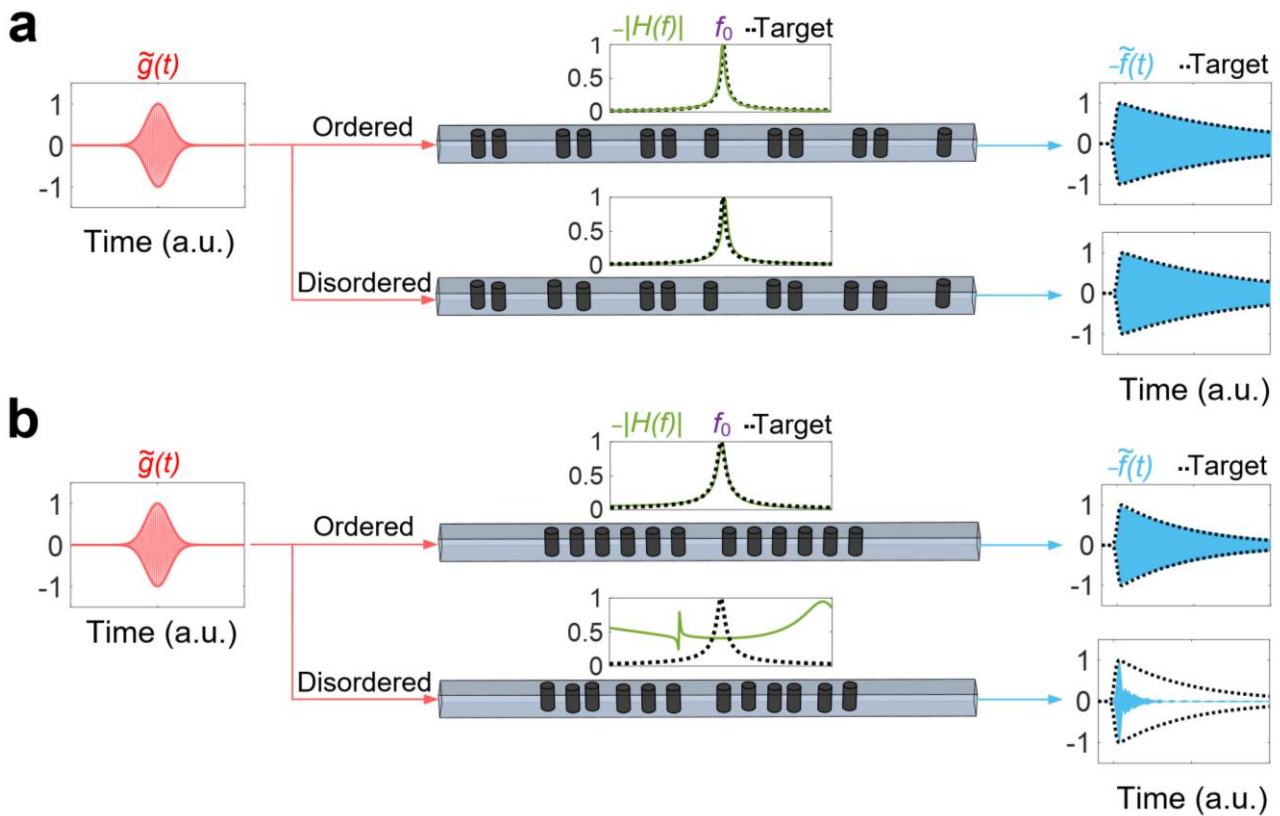
Figure 3.4: Demonstration of the proposed topological equation for a Gaussian type input signal, a, The topological equation solver works properly with or without position shift disorder. b, In contrast, the trivial equation solver only works properly in the absence of disorder [172].

modulated signal as the excitation, and investigated the behavior of the topological (panel a) and trivial equation (panel b) solvers in the absence and presence of disorder.

3.3   Symmetry protection of the proposed topological equation solver

Since 1D topological phases are symmetry protected, these numerical results raise an important question: what is the underlying symmetry of the proposed system that protects its edge modes? In regular tight-binding SSH chains, made of evanescently coupled identical resonators with detuned hoppings K and J (Fig. 3.5a, top panel), the mid-gap edge mode occurring at a topological boundary is protected by chiral symmetry [30], and a transfer function based on tunneling through this edge mode is robust to disorder in the hoppings, as long as they are weak enough not to close the band gap. However, transmission is not robust to even small levels of on-site disorder, which breaks chiral symmetry. This is exemplified in Figure 3.5a-c. Fig. 3.5a shows the mid-gap spectral transmission resonance associated with a perfectly ordered sample. Figure 3.5b shows the transfer function immunity to disorder in the couplings. Finally, Fig. 3.5c shows the large sensitivity of the transmission peak to arbitrarily small disorder in the resonance frequencies, which breaks the chiral symmetry.

The proposed multiple scattering system, albeit not based on evanescent coupling, behaves similarly. The transmission peak of the ordered sample (Fig. 3.5d) survives disorder shifts that do not close the band gap (Fig. 3.5e), but not disorder in the obstacle radii (Fig 3.5f). In order to explain these numerical observations, I investigate the topological properties and symmetry protection of the system under study in the following.

The bulk crystal is one-dimensional with lattice constant a and two obstacles per unit cell. I model it and define its topology using the transfer matrix M_{cell} of a unit cell. I start by defining the two scattering matrices S_1 and S_2, as the far-field scattering matrices of each obstacle when being alone in the monomode waveguide. These matrices relate the outgoing complex signals on the left (L) and right (R) sides of the scatterers b_L and b_R to the incident ones, a_L and a_R

$$\begin{pmatrix} b_{L,i} \\ b_{R,i} \end{pmatrix} = S_i \begin{pmatrix} a_{L,i} \\ a_{R,i} \end{pmatrix} \tag{3.2}$$

For now, I do not make the assumption that the two matrices are equal: for instance, the cylinders could have different cross-sections, or be shifted with respect to each other, etc. These matrices also usually depend on the angular frequency ω. Assuming conservation of energy during the scattering process, they must be unitary. We can therefore parametrize them very generally as
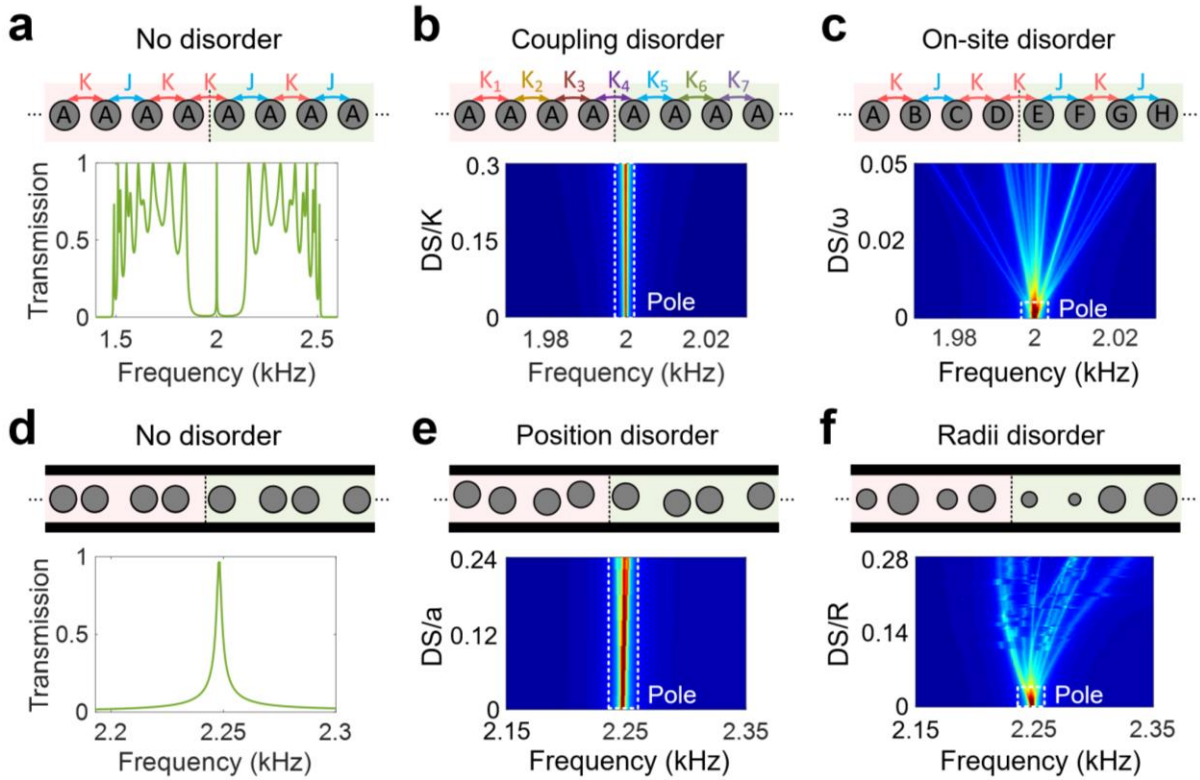
Fig. 3.5: Effect of various defect types on the topological equation solver, a, A topological interface made from tight binding SSH chains (top). The transmission spectrum of the chain (bottom) shows a mid-gap resonance, which corresponds to the topological edge mode. b, Some disorder is added to the hopping amplitudes of the system (top), which preserve chiral symmetry. The bottom panel demonstrates the robustness of the transmission peak as the disorder strength (DS) is increased. c, Same as panel c except that the disorder is applied to the on-site potentials of the chain, hereby breaking chiral symmetry. The transmission peak is sensitive to arbitrarily weak disorder. d,e,f, Same as a-c but for the proposed acoustic equation solver. The resonance line-shape of the edge mode is robust to the position movement of the rods inside the waveguide (panel e), which does not break the symmetry $M_{cell}^2 = 1$. In contrast, detuning the radii of the obstacles breaks this property, and causes degradation in the performance of the equation solver (panel f) [172].

$$S_1 = \begin{pmatrix} e^{i\varphi_1}\cos\theta_1 & e^{i\alpha_1}\sin\theta_1 \\ -e^{-i\alpha_1}\sin\theta_1\, e^{i\Phi_1} & e^{-i\varphi_1}\cos\theta_1\, e^{i\Phi_1} \end{pmatrix} \tag{3.3}$$

$$S_2 = \begin{pmatrix} e^{i\varphi_2}\cos\theta_2 & e^{i\alpha_2}\sin\theta_2 \\ -e^{-i\alpha_2}\sin\theta_2\, e^{i\Phi_2} & e^{-i\varphi_2}\cos\theta_2\, e^{i\Phi_2} \end{pmatrix} \tag{3.4}$$

where the frequency dependent angles $\theta_{1,2}$, $\alpha_{1,2}$, $\varphi_{1,2}$, and $\Phi_{1,2}$ are unique once we fix the reference plane, here at the central position of the scatterer. Assuming reciprocity ($S_{21} = S_{12}$), we must have $2\alpha_{1,2} - \Phi_{1,2} = \pi$, which restricts us to three parameters per scattering matrix, allowing to write:

$$S_1 = \begin{pmatrix} e^{i\varphi_1}\cos\theta_1 & e^{i\alpha_1}\sin\theta_1 \\ e^{i\alpha_1}\sin\theta_1 & -e^{-i\varphi_1}\cos\theta_1\, e^{2i\alpha_1} \end{pmatrix} \tag{3.5}$$

$$S_2 = \begin{pmatrix} e^{i\varphi_2}\cos\theta_2 & e^{i\alpha_2}\sin\theta_2 \\ e^{i\alpha_2}\sin\theta_2 & -e^{-i\varphi_2}\cos\theta_2\, e^{2i\alpha_2} \end{pmatrix} \tag{3.6}$$

One can then derive the associated transfer matrices M_1 and M_2, defined as

$$\begin{pmatrix} b_{R,i} \\ a_{R,i} \end{pmatrix} = M_i \begin{pmatrix} a_{L,i} \\ b_{L,i} \end{pmatrix} \tag{3.7}$$

and obtains

$$M_1 = \begin{pmatrix} \dfrac{e^{i\alpha_1}}{\sin\theta_1} & -\dfrac{e^{-i\varphi_1}e^{i\alpha_1}\cos\theta_1}{\sin\theta_1} \\ -\dfrac{e^{i\varphi_1}e^{-i\alpha_1}\cos\theta_1}{\sin\theta_1} & \dfrac{e^{-i\alpha_1}}{\sin\theta_1} \end{pmatrix} \tag{3.8}$$

$$M_2 = \begin{pmatrix} \dfrac{e^{i\alpha_2}}{\sin\theta_2} & -\dfrac{e^{-i\varphi_2}e^{i\alpha_2}\cos\theta_2}{\sin\theta_2} \\ -\dfrac{e^{i\varphi_1}e^{-i\alpha_2}\cos\theta_2}{\sin\theta_2} & \dfrac{e^{-i\alpha_2}}{\sin\theta_2} \end{pmatrix} \tag{3.9}$$

If the two scatterers are separated by a distance d in a unit cell of lattice constant a, the total transfer matrix of the unit cell M_{cell} is the product:

$$M_{cell} = M_{\frac{a-d}{2}} M_2 M_d M_1 M_{\frac{a-d}{2}} \tag{3.10}$$

with

$$M_L = \begin{pmatrix} e^{\frac{i\omega L}{c}} & 0 \\ 0 & e^{-\frac{i\omega L}{c}} \end{pmatrix}$$

(3.11)

where $L = d, \frac{a-d}{2},$ and c is the phase velocity. One obtains, after taking the matrix product,

$$M_{cell}(\omega) = \begin{pmatrix} M_{11}(\omega) & M_{21}^*(\omega) \\ M_{21}(\omega) & M_{11}^*(\omega) \end{pmatrix}$$

(3.12)

with

$$M_{11}(\omega) = e^{\frac{i\omega a}{c}} e^{i(a_1+a_2)} \csc\theta_1 \csc\theta_2 + e^{\frac{i\omega(a-2d)}{c}} e^{i(\varphi_1-\varphi_2)} e^{-i(a_1-a_2)} \cot\theta_1 \cot\theta_2$$

(3.13)

$$M_{21}(\omega) = -e^{\frac{i\omega d}{c}} e^{i\varphi_2} e^{i(a_1-a_2)} \csc\theta_1 \cot\theta_2 - e^{-\frac{i\omega d}{c}} e^{i\varphi_1} e^{-i(a_1+a_2)} \cot\theta_1 \csc\theta_2$$

(3.14)

We will use the notation z^* to denote the complex conjugate of z. Noting $|\psi\rangle = [a, b]^T$, with a and b being the forward and backward complex field amplitudes at the entrance of the unit cell, the application of Bloch theorem yields the following eigenvalue problem,

$$M_{cell}(\omega)|\psi\rangle = e^{i k_B a}|\psi\rangle$$

(3.15)

which we call the Bloch eigenproblem of the crystal. Note the nontrivial dependence of $M_{cell}(\omega)$ on ω. The most straightforward use of the above equation is the following way: for all values of ω, one can diagonalize $M_{cell}(\omega)$, and get two opposite values $\pm k_B(\omega)$ of the Bloch wavenumber in the first Brillouin zone, and resolve the band structure. Note that M_{cell} is not unitary and is non-Hermitian, meaning that in general, the values $\pm k_B(\omega)$ are complex, allowing in principle for an infinite number of bands and bandgaps. Note further the difference with the standard tight-binding SSH model, which leads to a Hermitian eigenvalue problem that maps the Brillouin circle into the
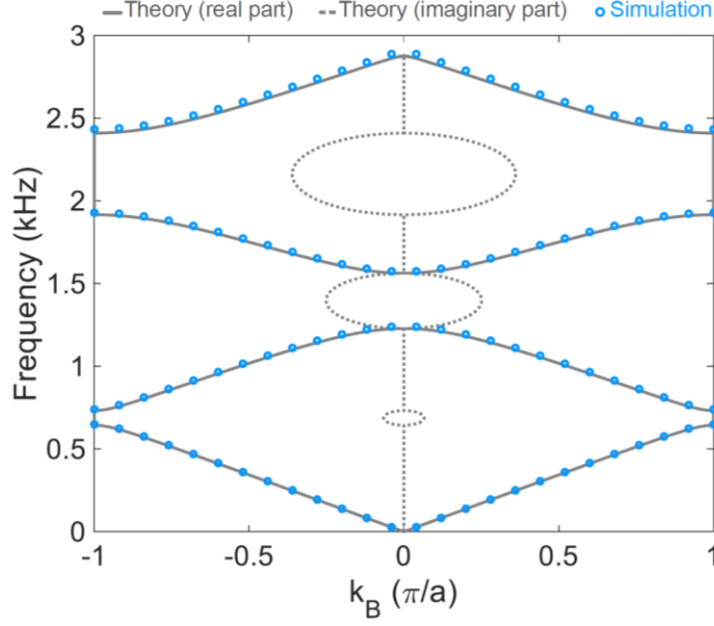
Fig. 3.6: Comparison between the crystal band structures obtained from the semi-analytical model based on the transfer-matrix approach and from full-wave finite-element simulations [172].

space of $SU(2)$ matrices, and a clear topological classification of chiral symmetric systems via the winding number. Here, consistent with time-reversal symmetry [180] $M_{cell}(\omega) \in SU(1,1)$, a group of non-Hermitian matrices [180]. $SU(1,1)$ Hamiltonians are found, for instance, in PT-symmetric extensions of the SSH tight-binding model [182] where non-Hermiticity of the Hamiltonian originates from the absence of energy conservation. Here, M_{cell} is not a Hamiltonian, in the sense that its eigenvalues are not related to ω, but to k_B, and the pseudo anti-Hermiticity of M_{cell} ($\sigma_z M_{cell}^\dagger \sigma_z = -M_{cell}$) is related to time-reversal symmetry. In Figure 3.6, I represent the band structure obtained from the transfer matrix approach, and compare it with the one obtained directly from full-wave simulations of the unit cell subjected to periodic boundary conditions (FEM method). To solve the transfer matrix eigenvalue problem, the dispersive parameters $\theta_{1,2}$, $\alpha_{1,2}$ and $\Phi_{1,2}$, which depend on frequency, were extracted from FEM scattering simulations of a single obstacle in a waveguide. The distance between the two scatterers is taken to be $d = \frac{a}{2} - e_p$, with $e_p = 2.8\ cm$ ("trivial" case) and $a = 23\ cm$. The rod diameter is $3.5\ cm$ and the width of the waveguide is $7\ cm$. The agreement between the two approaches validates the accuracy of the

multiple scattering model, in particular the underlying assumption of no near-field interactions between the obstacles in the crystal. To define the topology of the system in the next section, we first need to establish a few key properties of the unit cell transfer matrix. We start with general properties, before moving to more specific properties on a band or at degenerate points of the band structure. As a direct consequence of time-reversal symmetry [180], the transfer matrix of the system M_{cell} belongs to the group $SU(1,1)$ of matrices of the form

$$M_{cell} = \begin{pmatrix} \alpha & \beta^* \\ \beta & \alpha^* \end{pmatrix} \tag{3.16}$$

which is parametrized using the Pauli matrices as

$$M_{cell} = \alpha_R \sigma_0 + \beta_R \sigma_x + \beta_I \sigma_y + i\alpha_I \sigma_z \tag{3.17}$$

Its eigenvalues, given by $\lambda_\pm = \alpha_R \pm i\sqrt{\alpha_I^2 - \beta_R^2 - \beta_I^2}$ are real when $\alpha_I^2 < |\beta|^2$, and complex otherwise. These eigenvalues are degenerate under the condition $\alpha_I^2 - \beta_R^2 - \beta_I^2 = 0$, i.e. when the parameters β_R, β_I and α_I belong to a double cone in the $(\beta_R, \beta_I, \alpha_I)$ space. This cone is represented in the bottom panels of Figure 3.7. At the tip of the cone, one has $\beta_R = \beta_I = \alpha_I = 0$, meaning that M_{cell} reduces to $M_{cell} = \alpha_R \sigma_0$.

On a band, the matrix M_{cell} has a special form. Indeed, the Bloch eigenproblem implies that $\alpha_R \pm i\sqrt{\alpha_I^2 - |\beta|^2} = e^{i\,k_B a}$, from which follows that

$$\alpha_R = \cos(k_B a) \tag{3.18}$$

and

$$|\alpha|^2 = 1 + |\beta|^2 \tag{3.19}$$

implying $\alpha_I^2 + \alpha_R^2 = 1 + |\beta|^2$, which is equivalent to $\alpha_I^2 = \sin^2(k_B a) + |\beta|^2$, or

$$\alpha_I = \pm\sqrt{\sin^2(k_B a) + |\beta|^2} \tag{3.20}$$

On a band, we therefore have

$$M_{cell} = \begin{pmatrix} \cos(k_B a) \pm i\sqrt{\sin^2(k_B a) + |\beta|^2} & \beta^* \\ \beta & \cos(k_B a) \mp i\sqrt{\sin^2(k_B a) + |\beta|^2} \end{pmatrix} \qquad (3.21)$$

As a result, a band describes a one-to-one mapping from the Brillouin circle onto a closed path $\mathcal{C}$ in the subspace of $SU(1,1)$ matrices $M_{cell}(k_B)$ with the above form. From the Bloch eigenvalue problem $M_{cell}(\omega)|\psi\rangle = e^{i k_B a}|\psi\rangle$, one deduces that on a band, $M_{cell}(\omega)$ has complex eigenvalues, meaning that $\alpha_I^2 > |\beta|^2$, i.e. the path $\mathcal{C}$ must be inside the cone, either in the upper region $\alpha_I > |\beta|$, or the lower one $\alpha_I < -|\beta|$. In addition, the path $\mathcal{C}$ can only touch the cone whenever the eigenvalues of M_{cell}, namely $e^{i k_B a}$, are degenerate. This is necessarily the case at the edges of the Brillouin zone ($k_B = \pm\frac{\pi}{a}$), and at its center $k_B = 0$. In between, $\mathcal{C}$ cannot touch the cone, since two distinct eigenvalues $e^{\pm i k_B a}$ must be found, by virtue of time-reversal symmetry. Finally, the path $\mathcal{C}$ is not a loop, but a simple line, since M_{cell} is a simple function of ω, and therefore is the same for two opposite values of k_B on a band: it starts on the cone at $k_B = -\frac{\pi}{a}$ and lands on it again $k_B = 0$, before following the reverse path between $k_B = 0$ and $k_B = \frac{\pi}{a}$. Figure 3.7a represents an example of $\mathcal{C}$ contour for the third band of Figure 3.6 (supposedly topologically "trivial" case, with $e_p = 2.8$cm), and Figure 3.7c represents the same contour for $e_p = -2.8$cm, corresponding to the dual system, which is supposedly topological (the topological properties will be proven in the next section). Figure 3.7b represents the case $e_p = 0$ that closes the band gaps. As expected, in all cases the contour starts and ends on the cone.

To study the conditions under which two consecutive frequency bands can touch, it is convenient to recast the Bloch eigenproblem into the equivalent form:

$$e^{-i k_B a} M_{cell}(\omega)|\psi\rangle = |\psi\rangle \qquad (3.22)$$

and think of it as follows: for each k_B in the first Brillouin zone, finding the bands means finding the values of ω for which the matrix $e^{-i k_B a} M_{cell}$ has at least one eigenvalue equal to one, with the corresponding eigenvector being the Bloch eigenvector on that particular band. This can happen for infinitely many values of ω. If both eigenvalues of $e^{-i k_B a} M_{cell}$ at a given frequency are equal to

one, the band structure is doubly degenerate, which is therefore the maximum frequency degeneracy allowed by the system. Since the general form of the eigenvalues of $e^{-i\,k_B a}M_{cell}$ on a band are $v_\pm = e^{-i\,k_B a}\left(\alpha_R \pm i\sqrt{\alpha_I^2 - |\beta|^2}\right) = e^{-i\,k_B a}e^{\pm i\,k_B a}$, the second eigenvalue $e^{-2i\,k_B a}$ can only become equal to unity at the Brillouin zone edges ($k_B = \pm\frac{\pi}{a}$), or at $k_B = 0$. As a consequence, band gaps can only close at the center or edge of the Brillouin zone, i.e. when the contour $\mathcal{C}$ touches the cone.

Assuming the first case, i.e. a degeneracy at $k_B = \pm\frac{\pi}{a}$, one has $e^{-i\,k_B a} = -1$. We obtain, at the particular frequency of the degeneracy,

$$e^{-i\,k_B a}M_{cell} = \begin{pmatrix} 1 \mp i|\beta| & -\beta^* \\ -\beta & 1 \pm i|\beta| \end{pmatrix} \tag{3.23}$$

and this matrix can only be equal to identity if $|\beta| = 0$. The second case of degeneracy at $k_B = 0$ leads to the same conclusion ($|\beta| = 0$). This means that when two bands touch, the contour $\mathcal{C}$ is reaching the tip of the cone, as confirmed by Figure 3.7b.
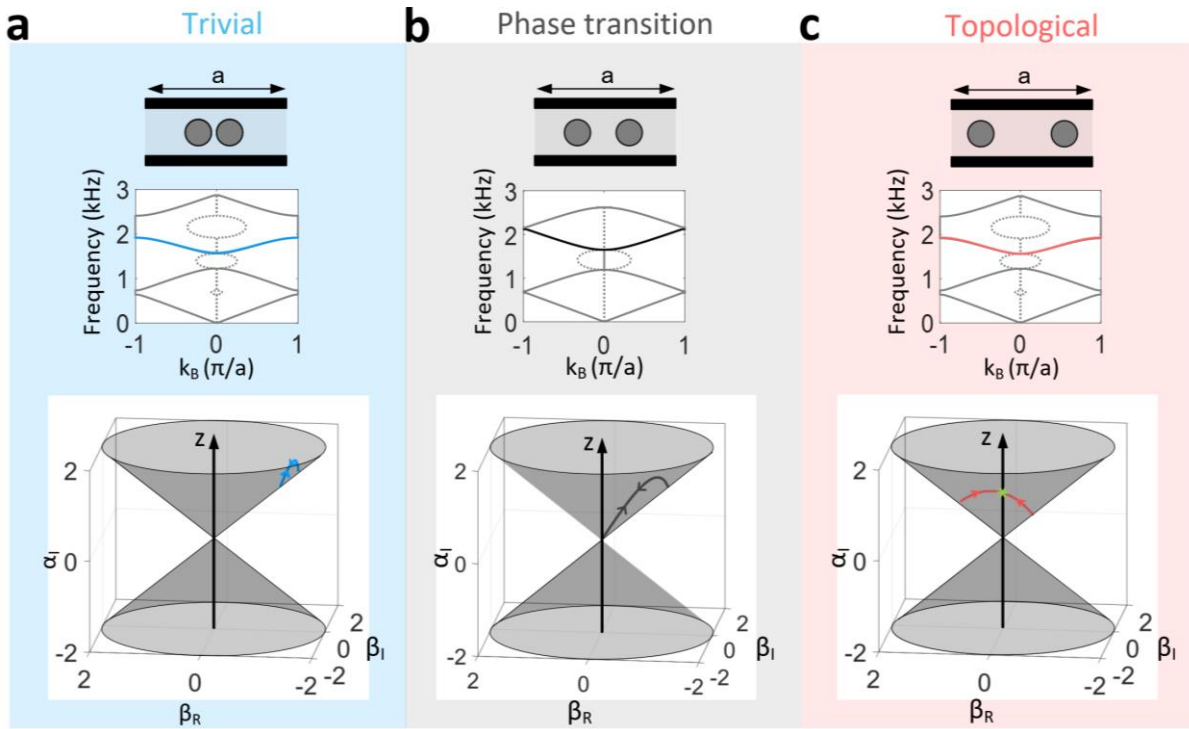
Figure 3.7: Band structure and associated contours $\mathcal{C}$ for the third band as the system goes through a topological phase transition [172].

As discussed previously, each band defines a mapping between the Brillouin circle and a subspace of $SU(1,1)$ matrices. We now define a topological invariant for each band, i.e. an integer quantity that is invariant upon continuous transformations of the band structure. This means that this number can only change when the band undergoes a discontinuous transformation, i.e. touches another one, or equivalently when the contour $\mathcal{C}$ touches the tip of the cone.

Like in the standard tight-binding SSH model, we need an extra symmetry, akin to chiral symmetry, to be able to define topological invariants on each band. Here we need to require that the scattering matrices S_1 and S_2 are equal, taking $\theta_1 = \theta_2 = \theta$, $\alpha_{1,2} = \alpha_{1,2} = \alpha$ and $\varphi_1 = \varphi_2 = \varphi$. With this extra condition, the quantity $\beta = M_{21}(\omega(k_B))$ in (3.14), that parametrizes the matrix M_{cell} on a band, becomes
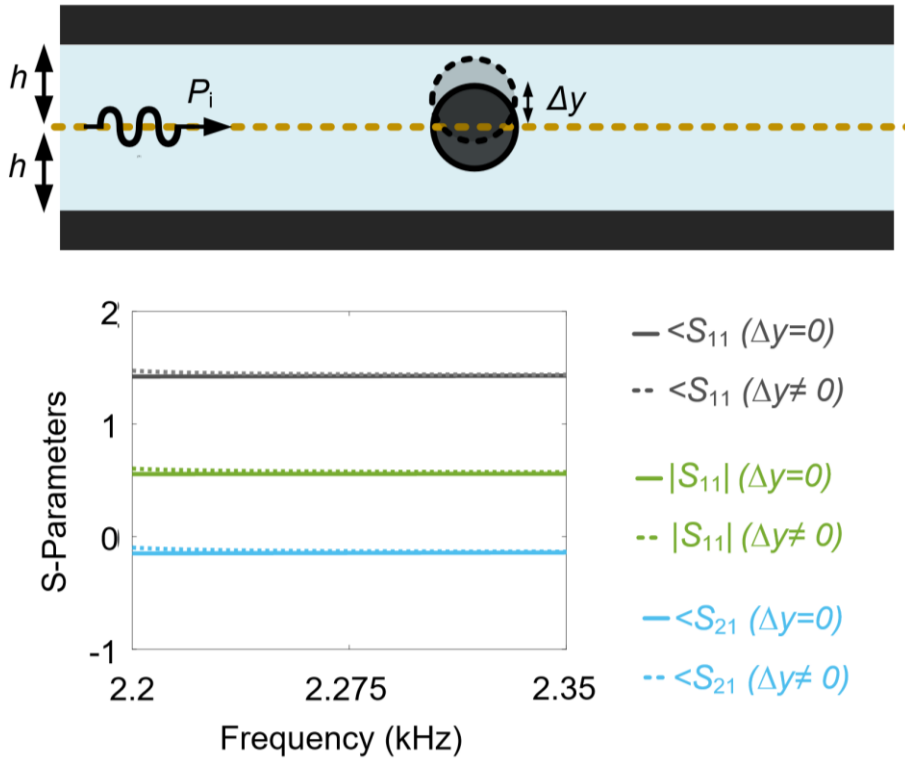
Figure 3.8: Vertical shifts negligibly affect the scattering parameters of the obstacle in the frequency range of interest, effectively preserving the symmetry $M_{cell}^2 = 1$ [172].

$$\beta(k_B) = -2e^{i(\varphi-\alpha)}\cos\left(\alpha + \frac{\omega(k_B)d}{c}\right)\cot\theta\csc\theta \qquad (3.24)$$

where the quantities α, θ and φ that parametrize the S matrix of a single obstacle generally depend on $\omega(k_B)$. We then assume the case of non-resonant scatterers, meaning that $\cos\theta$ does not vanish on the band, and the variation of α and θ on the band are weak. Then, $\omega(k_B)$ is necessarily monotonous between $-\pi/a$ and 0. Let us focus our attention to the quantity $\cos\left(\alpha + \frac{\omega(k_B)d}{c}\right)$, which can potentially make the complex number $\beta(k_B)$ vanish at some particular point of the Brillouin zone. When k_B goes from $-\pi/a$ to 0, the angle $\gamma = \alpha + \frac{\omega(k_B)d}{c}$ moves monotonically between two real values, say γ_{min} and γ_{max}, defining a continuous monotonous mapping between $\left[-\frac{\pi}{a}, 0\right]$ to $[\gamma_{min}, \gamma_{max}]$. Now, two situations can arise:

1) The segment $[\gamma_{min}, \gamma_{max}]$ does not contain $\pi/2$ (modulo π), in which case $\cos\left(\alpha + \frac{\omega(k_B)d}{c}\right)$ never vanishes as k_B go from $-\pi/a$ to 0. This means that β never vanishes on the band.

2) The segment $[\gamma_{min}, \gamma_{max}]$ contains $\pi/2$ (modulo π), in which case β vanishes at least once on the band.

Since $\beta = 0$ means that the contour $\mathcal{C}$ crosses the cone axis, we can therefore define a topological invariant η in the following way: We can count the number of times η that $\mathcal{C}$ crosses the cone axis as k_B go from $-\pi/a$ to 0. This integer number changes each time γ_{max} or γ_{min} equals $\pi/2$ (modulo π), i.e. when β is zero either at the edge or center of the Brillouin zone, i.e. when a band gap closes. Figure 3.7 shows how the contour $\mathcal{C}$ evolves for the third band of our system, when one goes from the trivial regime (panel a, $\mathcal{C}$ does not cross the cone axis, $\eta = 0$) to the topological one (panel c, $\mathcal{C}$ crosses the cone axis, $\eta = 1$). At the topological phase transition, the contour $\mathcal{C}$ touches the tip of the cone, which closes the band gap, and the number η is not defined.

The definition of the topological invariant η as the number of times the contour $\mathcal{C}$ crosses the cone axis between $-\pi/a$ to 0 is based on two underlying symmetries, and both must be fulfilled:

1) Time-reversal symmetry, which guarantees that M_{cell} belongs to $SU(1,1)$ [180].

2) Equality of S_1 and S_2 (the far-field individual scattering matrices of both obstacles must be identical), or equivalently:

$$M_{cell}^2 = 1 \tag{3.25}$$

Obviously, horizontal position disorder does not change the individual scattering parameters of the object. In addition, vertical position disorder does not change it either, at least in this frequency range, as demonstrated in Figure 3.8 (the only difference in the scattering spectrum are very sharp Fano interferences occurring from coupling to an acoustic bound state in the continuum, but they are far from the frequency range of interest). As a consequence, position disorder does not break $M_{cell}^2 = 1$. However, changing the diameter of one rod definitely changes its scattering matrix. What happens in the case of rods with different radii is that the real and imaginary part of the quantity

$$\beta(k_B) = -e^{\frac{i\omega(k_B)d}{c}}e^{i\varphi_2}\,e^{i(a_1-a_2)}\csc\theta_1\cot\theta_2 - e^{-\frac{i\omega(k_B)d}{c}}e^{i\varphi_1}e^{-i(a_1+a_2)}\cot\theta_1\csc\theta_2 \tag{3.26}$$

are never simultaneously zero, which implies that the contour $\mathcal{C}$ can avoid crossing the cone axis by simply going around it. This is analogous to an SSH chain without chiral symmetry, where some properly-chosen chirality-breaking defects at an interface can change the winding number without closing the band gap. These results explain the outcome of the full-wave simulations presented in the previous section.

3.4   Experimental demonstration of topological equation solver

Based on the theoretical findings discussed in section 3.2, I built a prototype of the topological equation solver (Fig. 3.9a, top signal path). The prototype consists of an acrylic square tube taking the role of the acoustic waveguide. Nylon 6 continuous cast cylinders were then manually inserted into the waveguide to form the SSH-type array. I first performed a frequency-domain measurement to obtain the transfer function of the system, $H(f)$, by exciting the waveguide with pseudo-random noise and recording the transmitted pressure with a microphone. The graph in the middle inset represents the magnitude of the measured transfer function (green curve) compared
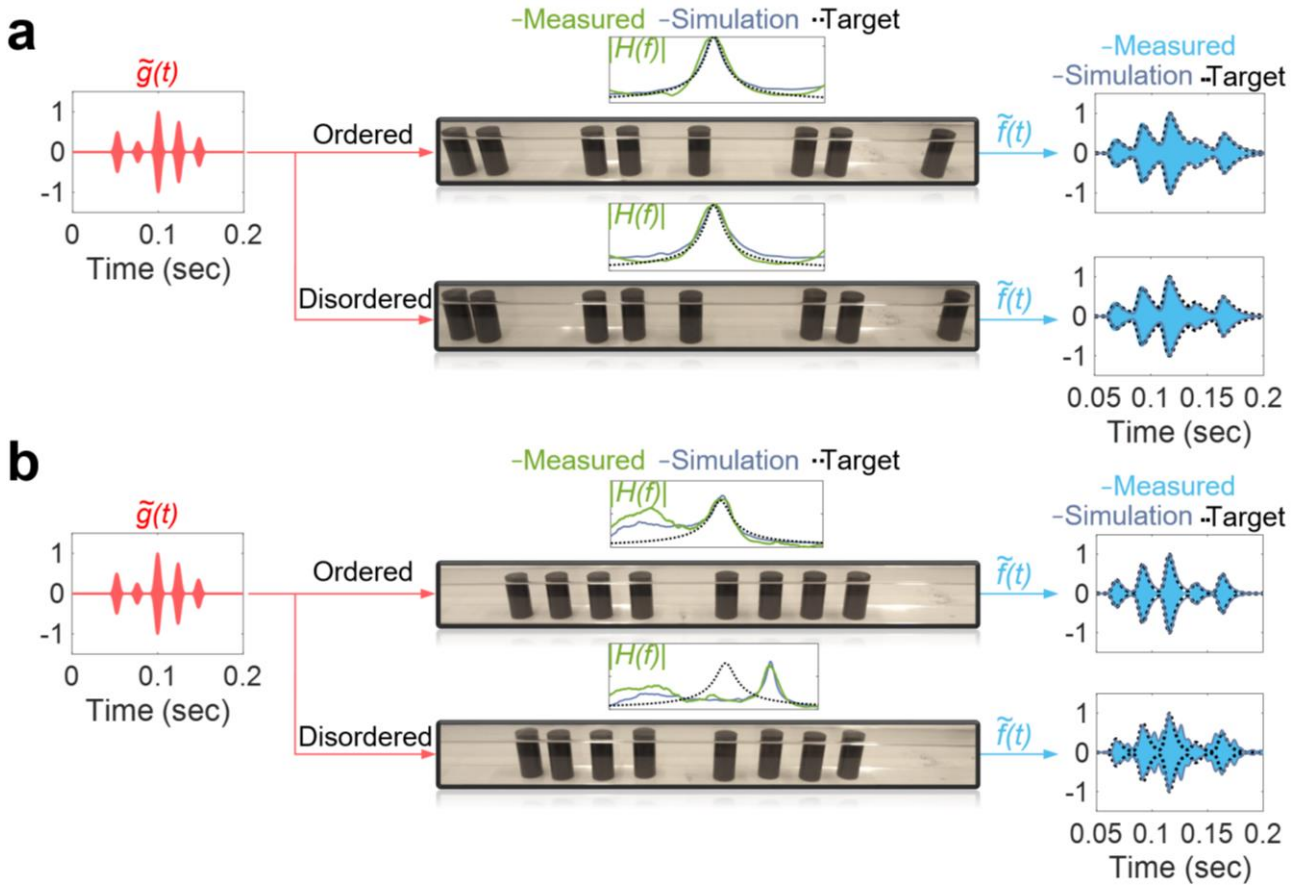
Figure 3.9: Experimental demonstration of a robust topological differential equation solver. a, The topological equation solver is indeed found to be immune to the shits in rods position. b, Very differently, the trivial equation solver is severely affected by disorder. The parameters of the linear differential equation are chosen to be $\alpha = 2.7\pi$, $\beta = 10\pi/3$, and the position disorder has the same strength in both cases [172].

to what I got from the numerical simulations (gray curve). As it is seen, the transfer function has a peak near the resonance frequency of the topological edge mode, which corresponds to the resonance parameters $A = 0.87$ and $Q = 0.03f_0$, or differential equation parameters $\alpha = 2.7\pi$, $\beta = 10\pi/3$. I next switch to a direct time-domain experiment and inject the same arbitrary input signal $\hat{g}(t)$ as in simulation into the waveguide. Comparing the measured transmitted pressure $\hat{f}(t)$ (blue line) with the exact solution of the corresponding differential equation (dashed line) confirms the proper functioning of the equation solver. To probe its stability, I then randomly move the cylindrical scatterers and repeat the same procedure (Fig. 3.9a, bottom signal path). It is noticed that, the topological ASP is still perfectly functional despite these large shifts.
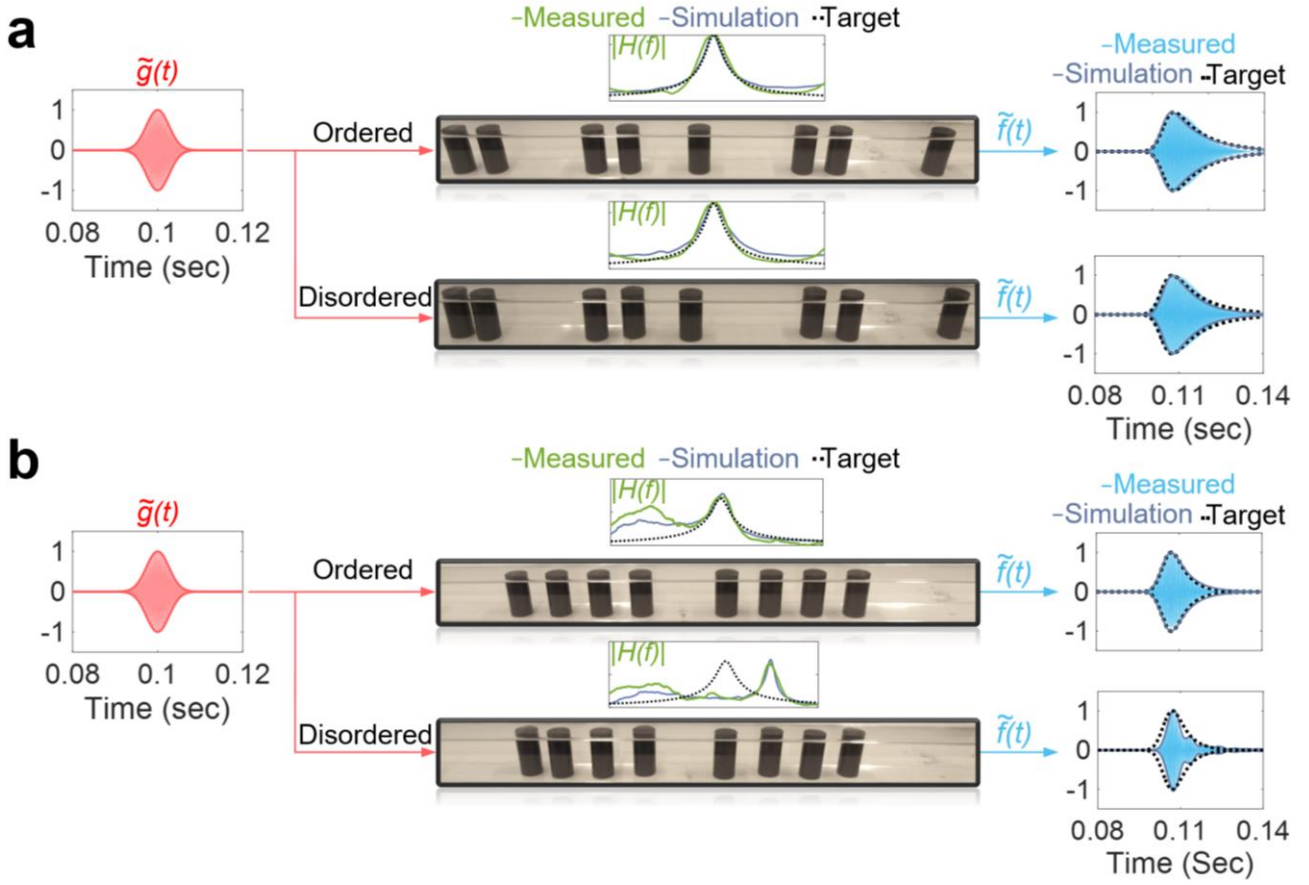
Figure 3.10: Experimental demonstration of the fabricated topological equation solver for a Gaussian type input signal. The figure repeats the results of Fig. 3.9 in the case of a Gaussian input signal. a, The topological equation solver works properly with or without position shift disorder, offering a strong stability. b, In contrast, the trivial equation solver only works properly in the absence of disorder [172].

This exceptional property is strikingly highlighted when we compare the measured output signal from the topological equation solver with that measured at the output of its trivial counterpart in the presence of disorder of similar strength (Fig. 3.9b). Very different from the topological processor, the signal coming out of the trivial processor is completely distorted, which clearly validates the superior robustness of topological ASP systems. In Fig. 3.10, I have repeated the measurement for another type of excitation signal, namely a Gaussian-type sinusoidal pulse modulated at f_0.
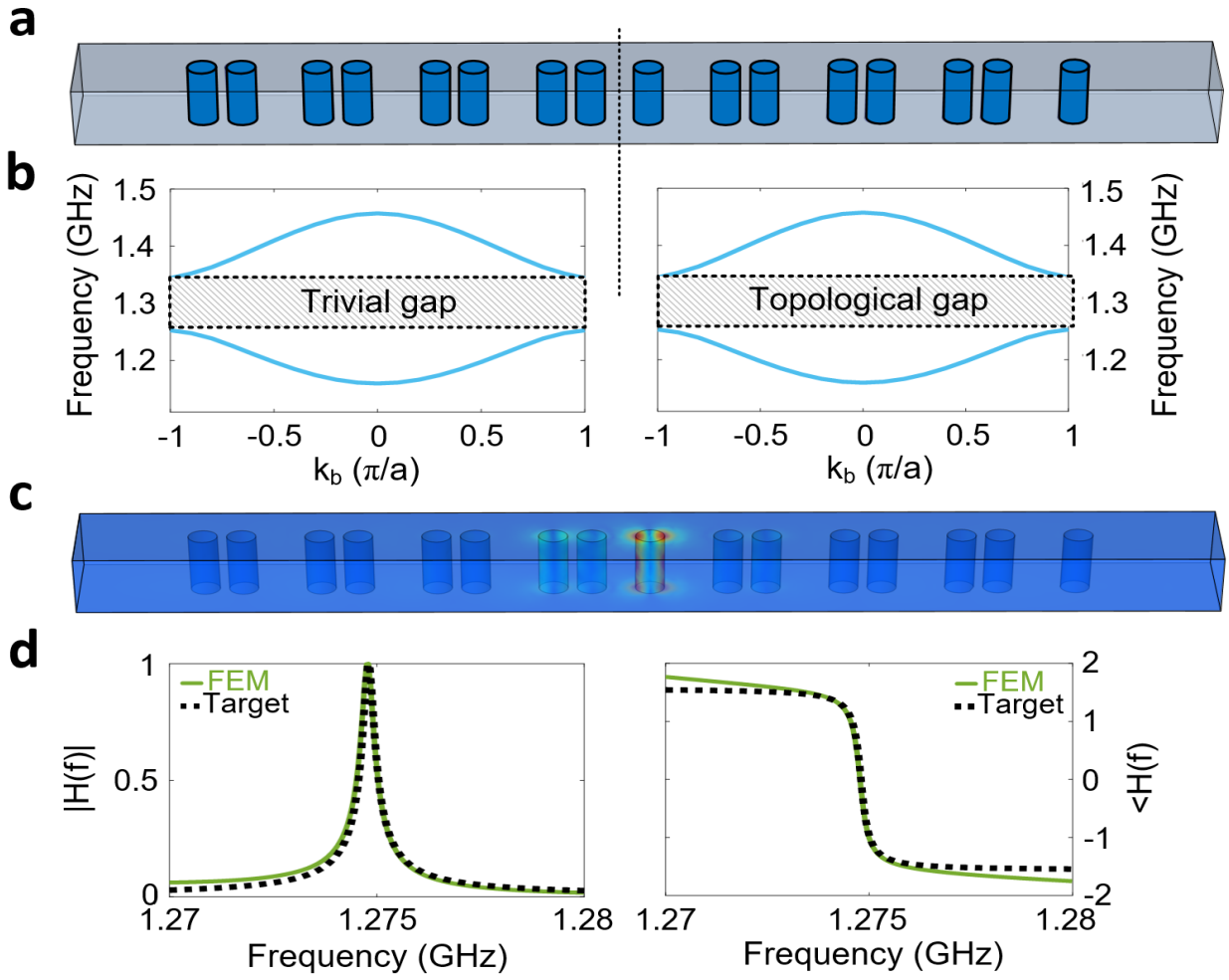
Figure 3.11: Photonic topological computer, a, A SSH array of silicon rods is implemented inside a metallic microwave waveguide. b, Band structure of the trivial (left) and non-trivial (right) semi-infinite crystals. c, Profile of the edge mode appearing at the interface between the trivial and non-trivial crystals. d, Upon exciting the edge mode, a topological resonance appears in the transmission spectrum of the waveguide [172].

3.5 Photonic topological equation solver

The idea of topological analog signal processing discussed in the previous sections can be readily transferred to other areas of classical physics. Here, as an instance, I describe the extension of the proposed acoustic equation solver to photonics and electromagnetics. Consider a SSH array of silicon rods placed inside a metallic rectangular waveguide whose width and height are 20 cm (Fig. 3.11a). Fig. 3.11b plots the band structure of the trivial (left) and topological (right) semi-infinite crystals. Through a topological phase transition, a topological edge mode appears at the interface between the two crystals whose profile is depicted in Fig. 311c.
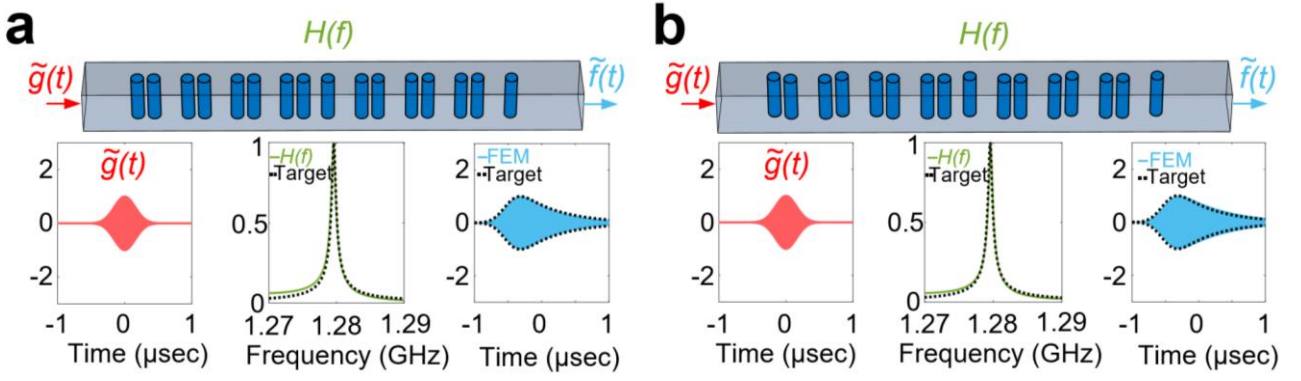
Figure 3.12: Demonstration of a topological microwave equation solver, a, A Gaussian ($\sigma = 1\,MHz$) input signal (left panel) modulated at f_0 is applied to the proposed topological resonator with the transfer function $H(f)$ (middle panel). The envelope of the output signal $\tilde{f}(t)$ (right panel) is the solution of a first order ODE. b, Same as panel a except that some disorder is added to the system. The proposed equation solver provides a strong stability against position disorder [172].

Upon its excitation, this topological edge mode creates a resonance in the transmission of the waveguide (Figs. 311d) at the frequency of $f_0 = 1.279\,GHz$. The resonance lineshape can be well estimated with the following transfer function of Eq. 3.1 for $A = 2.8 \times 10^5$ and $Q = 1.78 \times 10^{-6} f_0$, which corresponds to a first order ODE in time domain, as it was explained.

Now consider a Gaussian type ($\sigma = 1\,MHz$) input signal $g(t)$ modulated at the carrier frequency f_0 (Fig. 3.12a, left panel). Applying the transfer function $H(f)$ (middle panel) to the input signal, one obtains the corresponding output signal $\tilde{f}(t)$ (right panel), whose envelope is indeed the solution of the differential equation intended to be solved (dashed black line). Fig. 3.12b repeats the same analysis when some disorder is added to the sample by randomly moving the silicon rods. It is observed that, despite the large level of the disorder, neither $H(f)$ nor $\tilde{f}(t)$ has significantly changed, confirming the high stability of the proposed equation solver.

3.6 Towards second-order differential equation solving

The topological equation solver demonstrated in the previous section is capable of solving only one specific equation, depending on the quality factor of the resonating edge mode. More specifically, the quality factor of the resonance mode of the SSH array determines the constant coefficients of the ODE solved by the proposed topological differential equation solver. In this

section, I first discuss how the proposed topological equation solver can be tailored to solve first order ODEs with different constant coefficients. Then, I discuss the possibility of solving differential equations of second orders by constructing a network of first order ODE solvers of different kinds.

I propose three different approaches for controlling the coefficients of the ODE solved by the equation solver. The first and easiest way to do so is to increase the dissipation losses of the system, so as to change the quality factor of the topological resonating state. Consider again the SSH array of cylindrical obstacles (Fig. 3.13a) used to solve the desired equation. Previously, I had neglected the dissipation losses. Now I increase the dissipation losses a little bit and plot the resulting transfer function in Fig. 3.13b. It is observed that, as expected, the total quality factor of the resonance has been decreased with respect to the lossless case. The new transfer function of the system can be well estimated with $(f) = 1/(j(f - f_0) + 2)$, which corresponds to an ODE of the form $f'(t) + 4\pi f(t) = 2\pi A g(t)$.
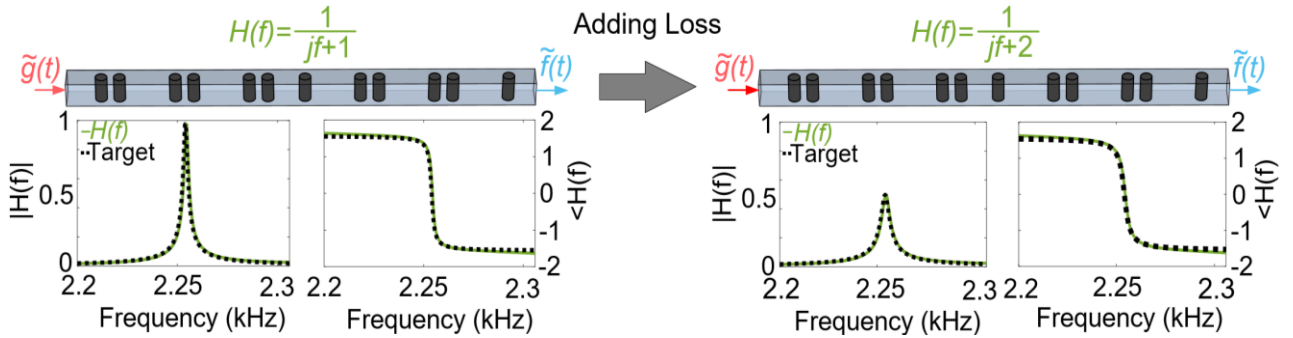
Figure 3.13: An approach to control the coefficient of the first order ODE solver by the proposed topological equation solver: The transfer function of the equation solver is changed by increasing the dissipation losses of the system [172].
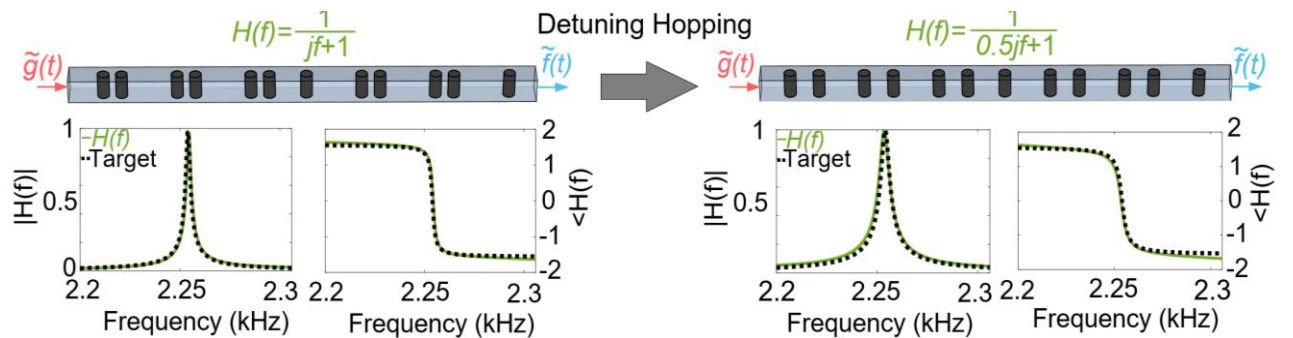
Figure 3.14: Another approach to control the coefficient of the first order ODE solver, based on detuning the hopping distances of the SSH array [172].
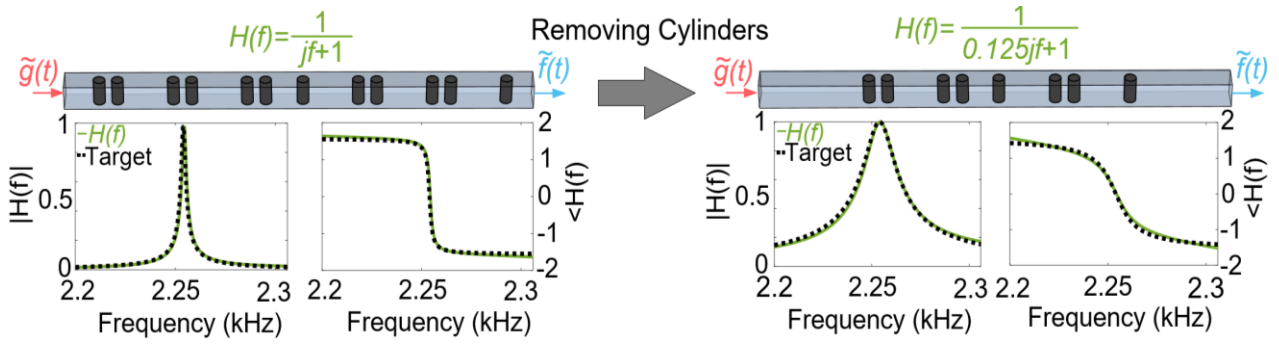
Figure 3.15: Another approach to control the coefficient of the first order ODE solved. The transfer function of the equation solver is changed by removing some of the scatterers of the array [172].

The second approach to control the quality factor of the topological resonance is to change the distances between the cylinders. Fig. 3.14a and b represent how the transfer function of the system changes from $H(f) = 1/(j(f - f_0) + 1)$ to $H(f) = 1/(0.5j(f - f_0) + 1)$ when moving from a SSH array with largely detuned array to a less deformed one. The ODE corresponding to this case has the form of $f'(t) + 4\pi f(t) = 4\pi Ag(t)$.

The third approach is to increase or decrease the number of unit cells of the SSH array. Obviously, a smaller number of unit cells gives rise to a topological resonance with a broader line-width (or smaller quality factor). This is evident from the results of Fig. 3.15a and b, where the transfer function of the system is changed from $H(f) = 1/(j(f - f_0) + 1)$ to $H(f) = 1/(0.125j(f - f_0) + 1)$ as a result of decreasing the number of unit cells from 3 to 2. The ODE corresponding to the latter case will be of the form $f'(t) + 16\pi f(t) = 16\pi Ag(t)$. Notice that, employing a combination of these three approaches, allows one to have a wide control over the constant coefficient of the ODE solved by the equation solver.

A straightforward strategy to implement a higher order topological equation solver would be constructing a network of first order ODE solvers corresponding to different transfer functions. Suppose, for instance, that we want to solve the second order differential equation $f''(t) + 6\pi f'(t) + 8\pi^2 f(t) = 4\pi^2 g(t)$, which corresponds to the transfer function $H(f) = 1/(2 + 3j(f - f_0) - (f - f_0)^2)$. Using partial fraction decomposition, one can then write $H(f) = H_1(f) - H_2(f)$, with $H_1(f) = 1/(1 + j(f - f_0))$ and $H_2(f) = 1/(2 + j(f - f_0))$. It follows that in order to

solve the desired second order differential equation, we can realize two (first order) equation solver with the transfer functions $H_1(f)$ and $H_2(f)$ and subtract their output signals, as conceptually sketched in Fig. 3.16. In order to implement the configuration shown in this figure, I first need to realize an acoustic rat-race coupler, being capable of adding or subtracting two acoustic signals to or from each other.
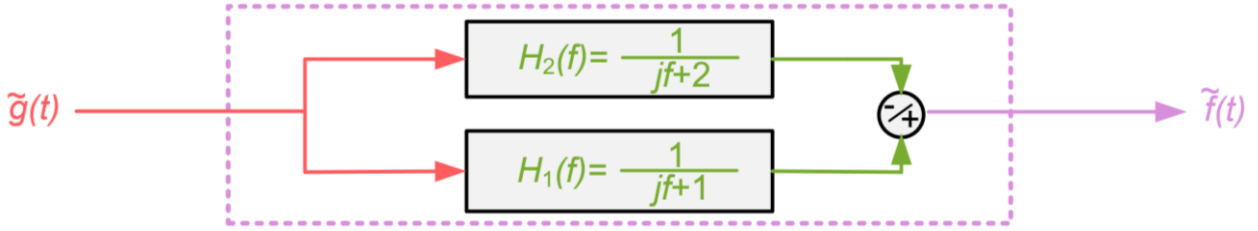
Figure 3.16: Implementation of a second order ODE solver by adding/ subtracting the output signals of two first order ODE solvers [172].

3.7   Acoustic rat-race coupler

In this section, I demonstrate, both theoretically and experimentally, the acoustic rat race coupler mentioned in the previous section, capable of adding or subtracting or two signals to or from each other in a fully analog fashion. The coupler works on the basis of constructive and destructive interferences between clockwise and counterclockwise acoustic modes of a ring resonator. The geometry of the proposed rat-race coupler is represented in Fig. 3.17. It consists of four ports placed around one half of a ring resonator at 0, 60, 120 and 180 degrees. The distance between the ports at the frequency of optimal operation is $\lambda_0/4$, while the total ring circumference is $3\lambda_0/2$. To gain some intuitive insight into the working principle of the structure, let us assume that an incident sound wave (with amplitude of a_0) is fed into port 1. The injected wave can couple, with a coupling coefficient of κ for instance, to the clockwise and counterclockwise modes of the ring. These clockwise and counterclockwise waves excite outgoing signals at ports 2 and 3 with the same phase, while their interference is destructive at port 4. Therefore, their superposition gives rise to a zero pressure field at port 4, and a pressure phasor of $-2j\kappa a_0$ at ports 2 and 3.
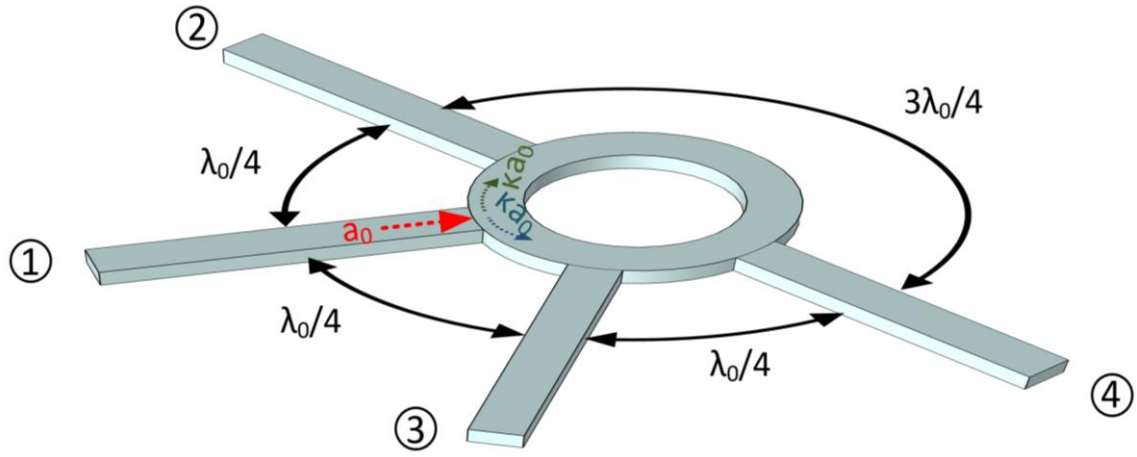
Figure 3.17: Acoustic rat-race coupler, consisting of four ports placed around one half of a ring resonator at 0, 60, 120 and 180 degrees [174].

Similarly, when the rat-race is excited from port 2, the clockwise and counter-clockwise modes interfere with each other destructively at port 3 while their constructive interferences leads to the pressure phasors of $-2j\kappa a_0$ and $2j\kappa a_0$ at ports 1 and 4, respectively. Following the same line of thoughts for the other two ports, one can obtain the scattering matrix of the four-port device as

$$S = -2j\kappa \begin{bmatrix} 0 & 1 & 1 & 0 \\ 1 & 0 & 0 & -1 \\ 1 & 0 & 0 & 1 \\ 0 & -1 & 1 & 0 \end{bmatrix} \tag{3.27}$$

Notice that, in our analysis, we have assumed that the sound injected into the ports does not reflect back when reaching the junction. This assumption holds true whenever the characteristic impedance of the ring is $\sqrt{2}$ times that of the arms. It should be further underlined that the unitary condition for the scattering matrix S implies $\kappa = 1/2\sqrt{2}$. Hence, the scattering matrix S becomes

$$S = -j/\sqrt{2} \begin{bmatrix} 0 & 1 & 1 & 0 \\ 1 & 0 & 0 & -1 \\ 1 & 0 & 0 & 1 \\ 0 & -1 & 1 & 0 \end{bmatrix} \tag{3.28}$$
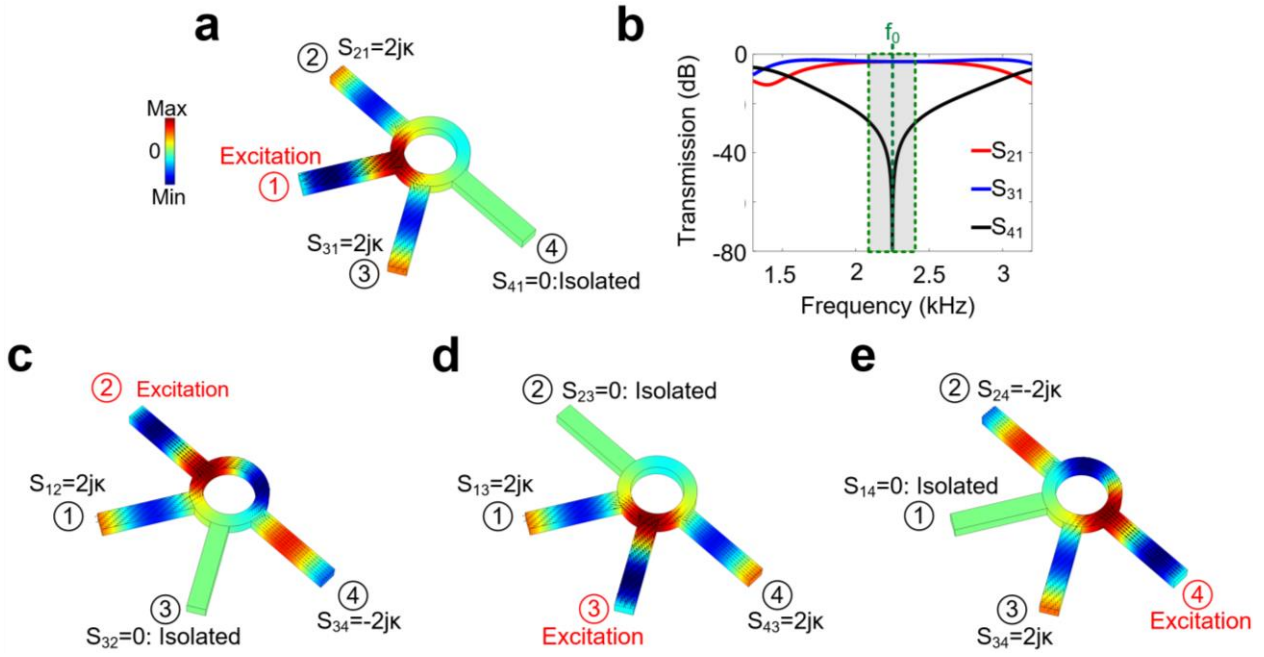
Fig. 3.18: Demonstration of the acoustic rat-race coupler. a, An input sound wave is injected into port 1 and the corresponding pressure profile is calculated using full-wave numerical simulations. The wave is transmitted, with same phase and amplitude, to ports 2 and 3 while port 4 is isolated. b, Variation of the scattering parameters versus frequency. The scattering parameters S_{21} and S_{31} become exactly equal at the frequency of desire f_0, whereas S_{41} drops to zero at this frequency. c,d,e, Same as panel a except that the structure is excited from ports 2, 3, 4, respectively [174].

From the obtained scattering matrix, it is can be inferred that, while all ports are connected to each other through the ring, one of them is always isolated from the others. It is also instructive to underline that, according the obtained scattering matrix, when ports 2 and 3 are simultaneously excited, the sum of these two input fields appears at port 1, while the received signal at port 4 is their difference. In this regard, ports 1 and 4 are sometimes known as sum and difference ports, respectively, while the two other ports are referred to as collinear arms in the literature. In order to examine the proper performance of the proposed device, I performed full-wave finite-element numerical simulations of a realistic junction, assuming that it is excited from port 1 with a time-harmonic plane wave of unit amplitude at the wavelength λ_0=15.3 cm, which corresponds to the resonance frequency of the system. The acoustic pressure distribution (snapshot in time) is shown in Fig. 3.18a. As expected, the input power couples out to ports 2 and 3, whereas the outgoing signal at port 4 is zero. Notably, the transmitted fields to waveguides 2 and 3 are out of phase with respect
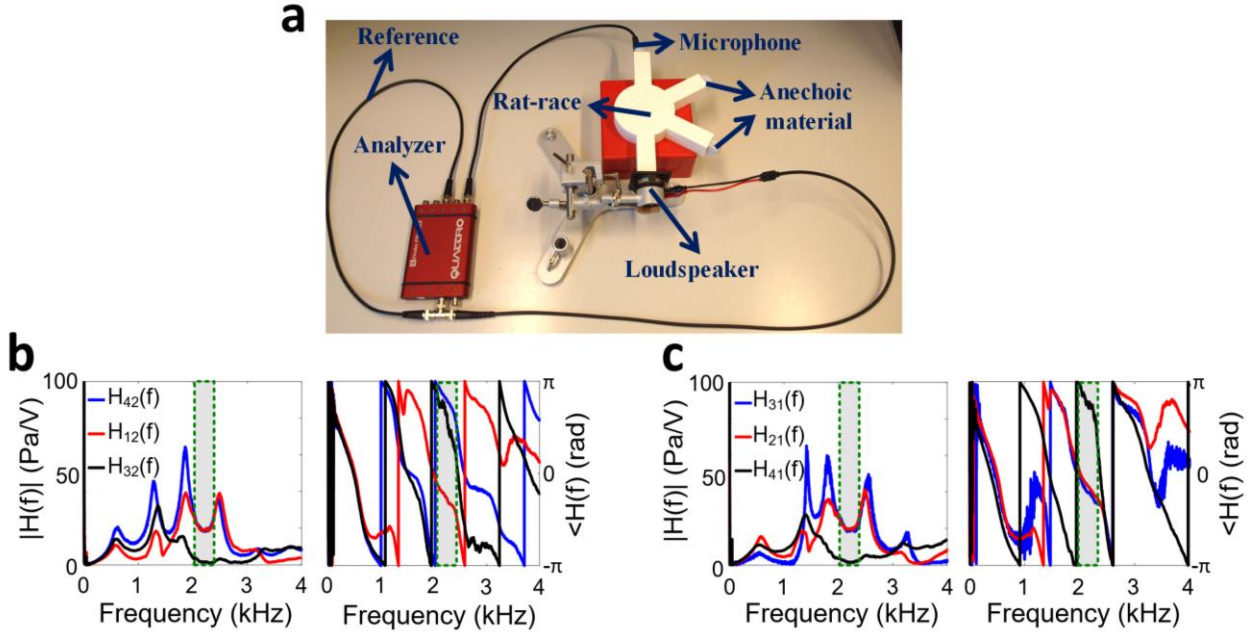
Fig. 3.19: Experimental demonstration of the acoustic rat-race coupler a, Experimental setup used to evaluate the functionality of the fabricated rat-race coupler. b, Magnitude (left) and phase (right) of the corresponding transfer functions when the rat race is excited from port 2. c, Same as panel b except that the excitation is placed at port 1. The experimental results are consistent with our numerical findings [174].

to the input signal, consistent with the scattering matrix of Eq. 3.28. The incident power is divided equally between ports 2 and 3. For further assertion, I calculated the frequency spectrum of the magnitude of the scattering parameters and plot them in Fig. 3.18b. As seen in the figure, S_{21} and S_{31} become exactly equal at $f_0 = {c}/{\lambda_0}$, whereas S_{41} goes to zero at this frequency. In order to fully prove the proper functioning of the device, I also investigate the cases of excitation at other ports. Figs. 3.18c, d and e report the corresponding pressure field distributions when ports 2, 3, and 4 are excited, respectively. The obtained field patterns are in perfect agreement with the scattering matrix derived for the system.

I built a prototype of such a coupler and evaluated its functionality using the experimental setup shown in Fig. 3.19a. To probe the scattering behavior of the fabricated structure, I first excite the rat-race from port 2 with a loudspeaker driven by a burst noise voltage, and measure the amount of pressure at ports 1, 3 and 4. Insets of Fig. 3.19b depict the magnitude (left) and phase (right) of

the resulting transfer functions versus frequency. It is clear that, near the resonance frequency of the rat-race coupler f_0 the parameters H_{42} and H_{12} become identical in magnitude but are opposite in phase. One further notices that, as expected, H_{32} approaches zero at this frequency. I next put the loudspeaker at port 1 and measure the magnitude (Fig. 3.19c, left) and phase (Fig. 3.19c, right) of the corresponding transfer functions H_{i1} ($i = 2,3,4$). It is obvious that H_{21} and H_{31} have the same magnitude and phase over a relatively large frequency range around f_0 (grey area), whereas H_{41} is close to zero within this frequency range. These experimental results are consistent with our prior numerical findings.

3.8   Realization of a second-order differential equation solver

As I already explained, one way to realize a second order differential equation solver is to subtract the output signals from two independent first order ODE solvers. This is accomplished in an analog way in Fig. 3.20, where $H_1(f)$ and $H_2(f)$ are realized using two different topological first order systems with tailored dissipation losses. The analog subtraction operation is realized with the acoustic rat-race coupler demonstrated in the previous section. Full-wave simulations involving the full geometry with the two-pipes and the rat-race coupler demonstrate that $H(f)$ is properly implemented. Hence, when an input signal, $\tilde{g}(t)$, say for example with a Gaussian envelope, is applied to the system, the envelope $f(t)$ of the output signal follows the exact solution of the target differential equation. This is confirmed by direct FDTD simulations.

The experimental demonstration of topological second-order differential equation solving is provided in Fig. 3.21. I designed two first-order differential equation solvers connected to each other via our 3D-printed acoustic rat-race coupler. The two first-order ODE solvers are tuned to solve the second order ODE by adjusting the level of transmission losses using sound absorbing melamine foam. I then simultaneously excited both waveguides with the input signal $\tilde{g}(t)$, and measured the output $\tilde{f}(t)$. As seen in the figure, excellent agreement exists between the measured output signal envelope $f(t)$ (solid blue line) and the expected exact solution of the corresponding second order differential equation (dashed line).
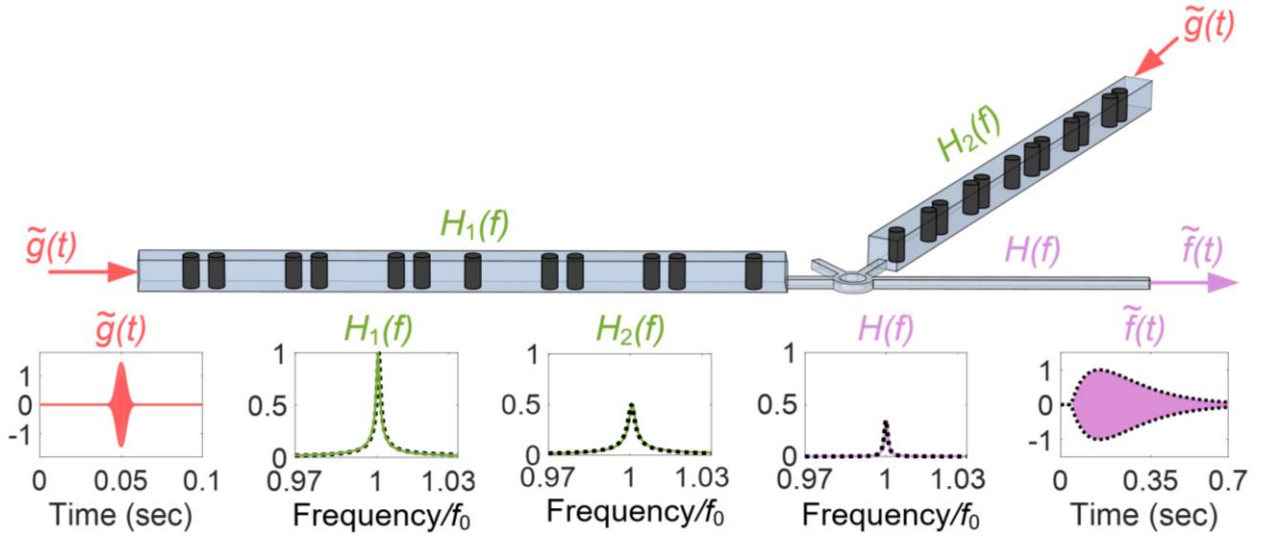
Figure 3.20: Robust resolution of a second-order differential equation by subtracting the output signals of two first order ODE solvers. The signal subtraction is realized with a rat-race. The bottom panels represent full-wave numerical simulations of the complete 3D structure in the case of a Gaussian pulse input, demonstrating that the targeted signal processing task is indeed performed by the system [172].
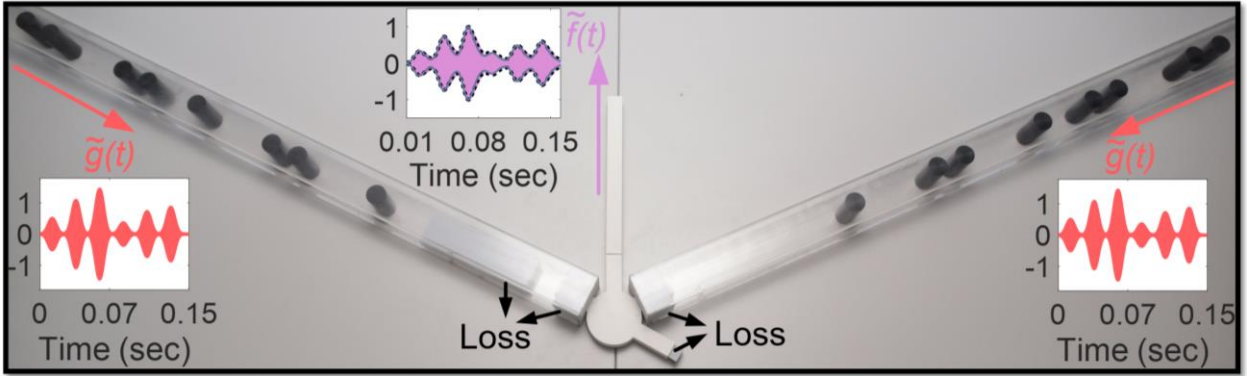
Figure 3.21: Experimental demonstration of second order topological ODE solving. The measured output signal envelope (f(t), purple lines) is found to be in perfect agreement with both the numerical simulation (gray) and with the exact solution of the corresponding second-order differential equation (dashed line) [172].

3.9 Higher-order topological differential equation solvers

The technique described in section 3.8 can easily be extended to the resolution of differential equations of arbitrary order. To clarify this, consider a differential equation of order nth of the form

$$f^n(t) + B_{n-1}f^{n-1}(t) + \cdots + B_1 f'(t) + B_0 f(t) = Ag(t) \tag{3.29}$$

By taking Fourier transform of both sides of equation, one obtains the following expression for the transfer function

$$H(f) = \frac{A/(2\pi)^n}{(j(f-f_0)^n) + 1/2\pi\, B_{n-1}\big(j(f-f_0)\big)^{n-1} + .. + 1/(2\pi)^{n-1}B_1\big(j(f-f_0)\big) + 1/(2\pi)^n B_0} \tag{3.30}$$

which can again be decomposed into partial fractions as

$$H(f) = \sum_{i=1}^{n} H_i(f) \tag{3.31}$$

where

$$H_i(f) = \frac{A_i}{j(f-f_0) + f_0/2Q}; i = 1,2,\dots,n \tag{3.32}$$

where $Q_i = -f_0/2P_i$, in which P_i are the complex poles of the following nth order polynomial

$$x^n + \left(\frac{1}{2\pi}\right)B_{n-1}x^{n-1} + \cdots \left(\frac{1}{2\pi}\right)^{n-1}B_1 x + \left(\frac{1}{2\pi}\right)^n B_0 \tag{3.33}$$

and A_i is of the form

$$A_i = \frac{\frac{A}{(2\pi)^n}(x - P_i)}{x^n + \left(\frac{1}{2\pi}\right)B_{n-1}x^{n-1} + \cdots \left(\frac{1}{2\pi}\right)^{n-1}B_1 x + \left(\frac{1}{2\pi}\right)^n B_0} |x = P_i \tag{3.34}$$

Eqs. 3. 31 and 3.32 suggest a straightforward approach to solve a differential equation of nth order: one has to first realize (first order) differential equation solvers corresponding to the transfer functions, and then add (or subtract) their output signals using rat race couplers. This is accomplished in the configuration shown in Fig. 3.22.
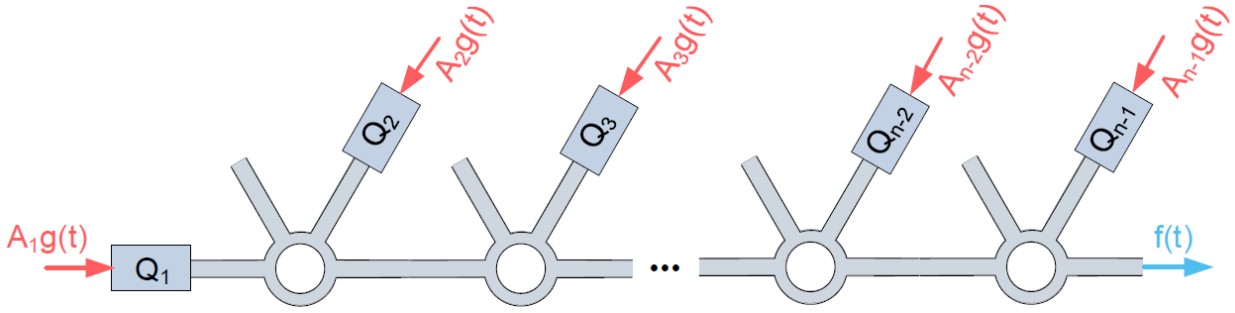
Figure 3.22: Realizing higher order topological ODE solvers: The output signals of n different first order ODE solvers are subtracted using rat race couplers. The overall transfer function of the system $H(f)$ corresponds to the transfer function of the nth order ODE [172].

3.10   Alternative strategies for realizing higher order ODE solvers

There exists alternative strategies for realizing topological equation solvers solving more complex, higher order ODEs. For example, one may consider cascading two or more SSH chains, allowing their topological edge modes to couple to each other, as I demonstrate below.

Shown in Fig. 3.23a (top) is two cascaded SSH arrays, each of which supports a topological edge mode (resonating at ω_0 with some decay rate of γ for example) at its phase transition boundary. Assuming the coupling coefficient between the two topological edge modes to be ϑ, for example, the transfer function of the overall chain then reads

$$H(\omega) = \frac{1}{-(\omega - \omega_0)^2 + 2j\gamma(\omega - \omega_0) + \vartheta^2 - \gamma^2} \tag{3.35}$$

which is nothing but the transfer function associated with a second order ODE. Fig. 3.23a (bottom) represents the transfer function of the coupled SSH chain under investigation, calculated by means of standard tight binding formalism. The obtained transmission coefficient can be fitted by the theoretical relation given in Eq. 3.35. To assess the robustness of such a topological filter, I add some disorder to the coupling coefficients between the resonators, and plot in Fig. 3.23b the evolution of the (averaged) transfer function versus disorder strength. It is apparent that the filter response is affected very minorly by the disorder. To make a comparative case, I couple two trivial resonating defect modes, forming at the boundaries between crystals with opposite on-site potential
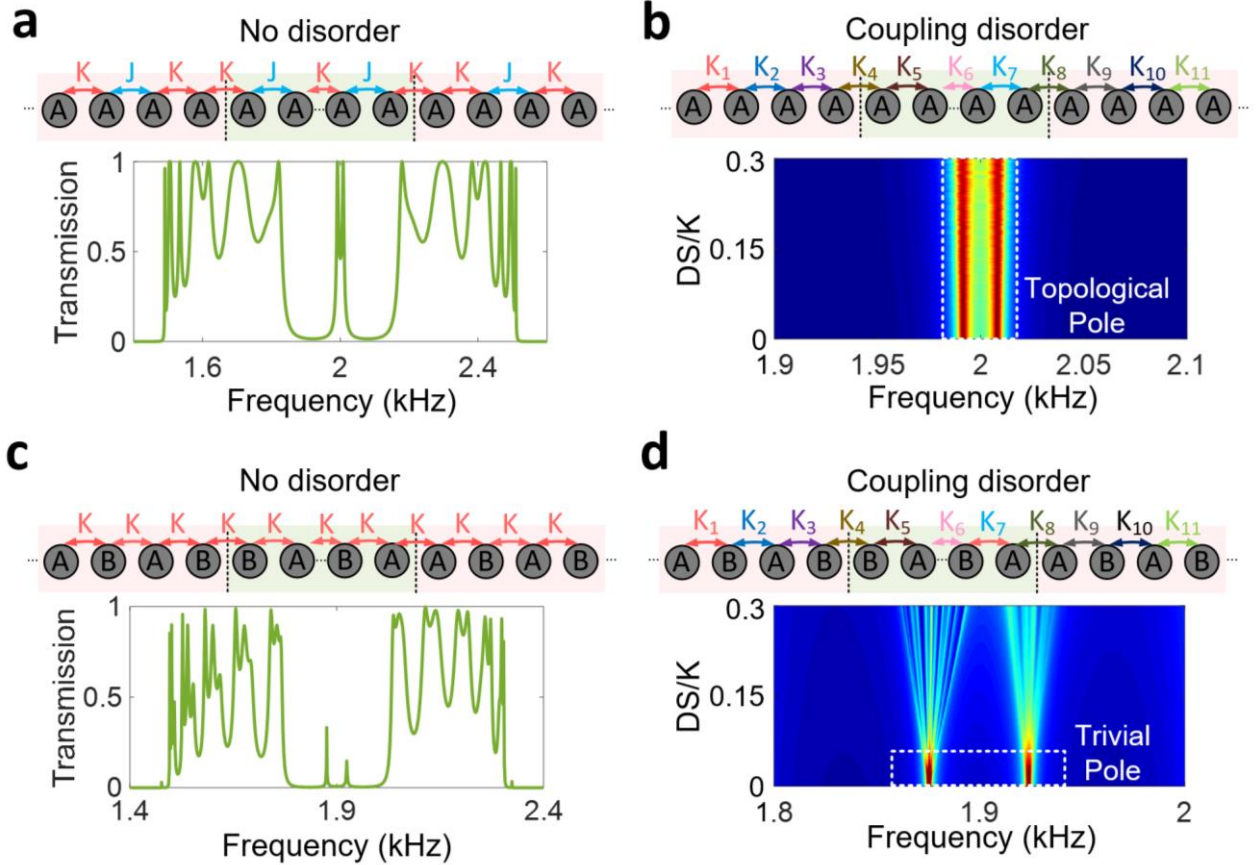
Figure 3.23: Demonstration of a second-order topological pass-band filter, a, Two SSH chain are coupled to each other. The transfer function of the whole chain can be approximated by the theoretical relation given in Eq. 3.35, corresponding to a second-order pass band filter. b, Evolution of the transfer function of the chain, averaged over 20 different realizations of disorder (applied to the hopping amplitudes), versus disorder strength. c,d, Same as a,b but for a trivial filter [172].

organizations, as shown in Fig. 3.23c. This also gives rise to the transfer function of a second order band-pass filter, which is trivial. Inset of Fig. 3.23d manifests the extreme sensitivity of such a topologically trivial filter to the applied disorder (note that we have used same type and amount of disorder in both trivial and topological cases).

Note that the system under investigation can be treated as a second order equation solver as well. More specifically, the transfer function given in Eq. 3.35 corresponds to the following second-order ODE in time domain

$$d^2 f(t)/dt^2 + 2\gamma \, df/dt + (\vartheta^2 - \gamma^2)f(t) = g(t) \tag{3.36}$$
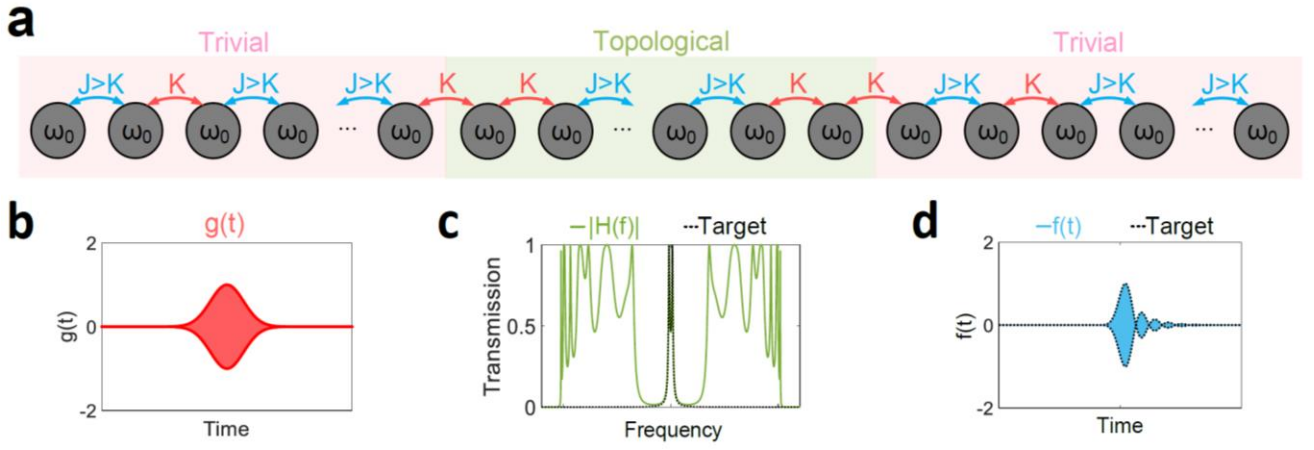
Figure 3.24: Realization of a second order ODE solver by coupling two SSH arrays to each other. a, Two distinct SSH arrays are coupled to each other. b, An input signal with a Gaussian distribution is applied to the array. c, Transfer function of the whole array. d, Output signal of the array, approximating well the solution of the ODE given in Eq. 3.36 [172].

To demonstrate such functioning, I consider in Fig. 3.24 an input signal with a Gaussian temporal evolution to be applied to the array, and calculate the corresponding output (Fig. 3.24d) by applying the transfer function of the array (Fig. 3.24c) to the input signal (Fig. 3.24b). Comparing the obtained output signal with the solution of Eq. 3.36 (its envelope) proves the expected functioning of the system. Notice that such an equation solver is protected against perturbations in the hopping amplitudes, as already demonstrated in Fig. 3.23.

3.11   Conclusions

In this Chapter, I showed how the seemingly unrelated concept of topological order in condensed matter systems can enable a novel generation of analog signal processors, whose functionalities are protected against large levels of imperfections and perturbations. This was achieved by realizing an acoustic analog computer based on the edge mode of a one-dimensional topological insulator. By providing numerical simulations and experimental measurements, I proved that, compared to ordinary trivial analog signal processors, the proposed topological computer provides one with strong immunity against geometrical disorder. I further demonstrated that, by

constructing a network or array of such kinds of computing systems, it is possible to realize more complex signal processing tasks.

The proposed topological equation solver was based on the "Lorentzian" line shape of the resonance associated with the edge mode of a one-dimensional topological insulator (SSH array). In the next chapter, I demonstrate a new (one-dimensional) topological structure, whose edge mode creates not a Lorentzian but a Fano-like spectral line shape upon excitation. This enables realizing more advanced computational operations, as I will discuss.

Chapter 4   Topological Fano resonances

This chapter is a modified version of the materials reported in [196].

In the previous Chapter, I showed how the Lorentzian line shape of the edge mode of a one dimensional topological insulator can be employed for solving a first order differential equation. I further showed that, by changing the quality factor of this resonance, one can achieve a large control over the constant coefficients of the corresponding equation. Yet, the fact that the spectral line-shape of the edge mode is always Lorentzian restricts the range of functionalities that can be achieved. In this chapter, I show that the proposed acoustic equation solver can support another type of topologically protected resonances, namely topological Fano resonances, produced as a result of constructive and destructive interference between two different topological edge modes coexisting within almost the same spectral range. I then discuss the possibility of performing novel signal processing tasks based on the peculiar line shape of such kinds of resonances. I start this chapter by a brief discussion about Fano resonances and their applications in modern engineering.

4.1   Introduction

The Fano resonance [182] is a ubiquitous scattering wave phenomenon, commonly found in various branches of science and engineering like atomic and solid states physics [183,184], electromagnetism [185-187], electronic circuits [188,189], photonics [191-193], nonlinear optics [194,195], and acoustics [196,197]. Such intriguing type of resonance occurs as a result of constructive and destructive interferences between two overlapping resonant scattering states with different lifetimes: a wide-band "bright" resonance, and a narrower "dark" resonance. The dark resonance serves as a quasi-isolated (localized) state whose coexistence in the continuum of the

bright resonance gives rise to the asymmetric and ultra-sharp line shape profile of the Fano resonance [198].

While originally developed to explain the inelastic scattering of electrons in Helium [199], the ultra-sharp spectrum of Fano resonances has established itself as a centerpiece in the realization of many modern optical devices, including low threshold lasers [200], low energy switches [201], ultrafast modulators [202], high quality factor filters [203], compact electromagnetically induced transparency (EIT) devices [204], ultrathin perfect absorbers [205], and highly accurate interferometers [206]. Moreover, apart from its steepness, the peculiar asymmetric line shape of Fano resonances is found to be excessively sensitive to environmental changes, a characteristic which has enabled the realization of highly sensitive and accurate sensors [207,208].

Unfortunately, this extreme sensitivity also comes with a price: guaranteeing a Fano resonance near the frequency of interest requires extreme control over the system's geometry as fabrication imperfections can shift the bright and dark modes away from each other. Even worse, disorder may introduce extra parasitic resonances, completely destroying the much-sought Fano line shape. Therefore, the performance advantages obtained from Fano interferences are often mitigated by the costs associated with the required fabrication technology. Although they work quite well in theory, the performance of Fano-based devices degrades significantly upon fabrication due to inevitable flaws [209].

As I discussed in the previous chapter, the recent development of topological wave physics offer an unprecedented solution to this vexing problem. Following these advances, one may wonder whether topology maybe leveraged to build a novel form of sturdy topologically protected Fano resonance, which may be largely appealing for a wide range of applications in different areas of physics, from photonics to mechanics and acoustics. In the following, I first extend the reach of topological wave physics by introducing the general concept of topological Fano resonances. More specifically, I demonstrate that the ultra-sharp spectrum of Fano resonances can be guaranteed by design without stringent geometrical requirements, and with a complete immunity to structural

disorder, while retaining its ability to shift under environmental changes. I further explain the relevance of such resonances performing analog computational tasks.

4.2   Acoustic topological Fano resonances

The underlying idea of my proposal is conceptually sketched in Fig. 4.1. Let us first consider the conventional Fano resonance (Fig. 4.1a). It is typically achieved by overlapping two resonant states with different lifetimes: one needs a bright and a dark mode that coexist in a certain spectral range. Upon coupling, the resonant interaction of these two states leads to constructive and destructive interferences, which creates the archetypal asymmetric peak-and-dip Fano line shape. Since the Fano resonance is a resonant scattering state obtained from an interference phenomenon between only two modes, it is intrinsically sensitive to perturbations in the geometry and environment. More specifically, even a small amount of disorder can shift the resonance frequencies and coupling phase of the two resonating modes, and introduce new resonant states that uncontrollably deform the peculiar Fano spectral signature. This is schematically represented in the right panel of Fig. 4.1a, where disorder has created new dips and peaks in the spectrum. My proposal is, instead, to start from bright and dark modes whose existence is topologically guaranteed (Fig. 4.1b, left). Upon coupling, a topological Fano resonance may be created, whose line shape can be preserved even in the presence of geometrical disorder. Environmental changes may shift the bright and dark modes, but not suppress them nor introduce new modes. As a result, the Fano shape inherits some form of topological immunity against disorder, as I demonstrate in the following.

Let us start with considering the two-dimensional acoustic parallel-plate waveguide represented in Fig. 4.2a. Assume first that the waveguide does not contain any obstructing object. The corresponding eigen-modes are either even or odd with respect to the dashed green line due to vertical inversion symmetry. By solving the scalar Helmholtz equation with the Neumann boundary
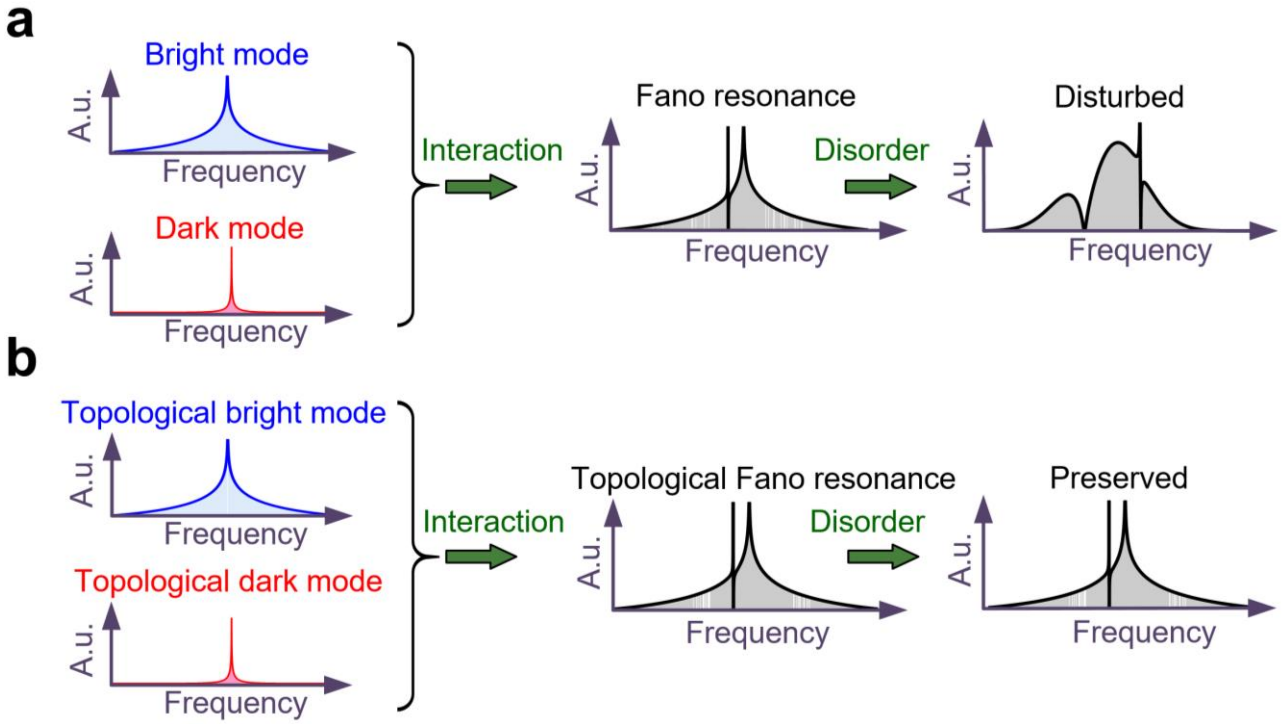
Figure 4.1: Topological Fano resonance. a, Interaction between a bright resonance and a dark narrower resonance can lead to an ultra-sharp and asymmetric line shape, characteristic of a Fano resonance. Even small levels of disorder, however, can severely destroy the line shape of the resonance, by introducing new dips and peaks. b, To make Fano resonances immune to disorder, one can instead start from bright and dark modes whose existence is topologically guaranteed. The resulting topological Fano line shape is robust against a large class of geometrical imperfections: the occurrence of new disorder-induced dips and peaks is prevented by topology [196].

condition being applied to the walls of the waveguide, one can easily find that the even modes do not have a cutoff frequency, whereas the odd modes possess a cut of frequency of $f_c = \pi c_s / 2h$ (c_s is the speed of sound).

Now, suppose a single cylindrical obstacle is embedded inside the waveguide, whose center is placed right at the centerline. Since the obstacle preserves the vertical mirror symmetry, the entire structure remains mirror-symmetric and the resulting eigenstates will still be either even or odd. An odd mode localized to the obstructing cylinder, and below the cutoff frequency of the radiation odd waves, i.e. f_c, can then coexist within the continuum of the even modes, while it remains completely decoupled from them because of its different symmetry. Shown in Fig. 4.2b is the field profile of this mode.
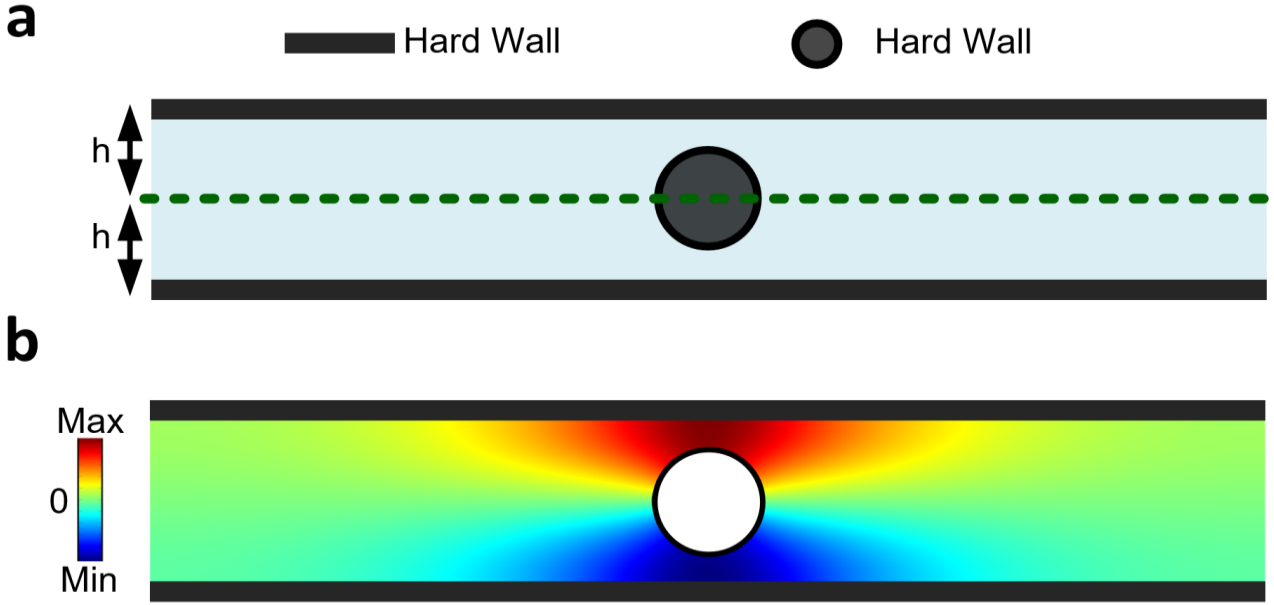
Figure 4.2: Symmetry-protected bound states in the continuum in an acoustic waveguide. a, An acoustic waveguide containing an obstructing cylinders is considered. b, An odd mode localized to the obstructing cylinder, and below the cutoff frequency of $\pi c_s/2h$ can happen to coexist within the radiation continuum of the waveguide while remaining perfectly bounded to the obstacle [196].

Based on its profile distribution, one can deduce that it is not possible for the even (radiation) modes traveling from one side to the other side of the waveguide to excite this odd-symmetric state, because of the different symmetry. Consequently, this mode is a symmetry-protected bound-state in the continuum (BIC): it is completely hidden in the transmission or absorption spectra when carrying out a scattering experiment [210].

Next, I consider a periodic array of acoustic bound states in the continuum described before (Fig. 4.3a). The corresponding band structure of the crystal is shown in the bottom panel. It is instructive to divide the dispersion bands into two categories according to the symmetry of their corresponding mode profiles, which are represented in Fig. 4.3b for $k_x = 0$ and $k_x = \pm\pi/a$. The first category is associated with eigenmodes having even symmetry with respect to the centerline of the waveguide. These bands, marked in blue in Fig. 4.3a, possess the typical frequency dispersion of a one-dimensional sonic crystal made of far-field coupled scatterers, with waves propagating down to the quasi-static limit. The second category (the red band), corresponding to odd-symmetric eigenstates, exhibits the typical cosine band characteristic of evanescently coupled resonators. Such
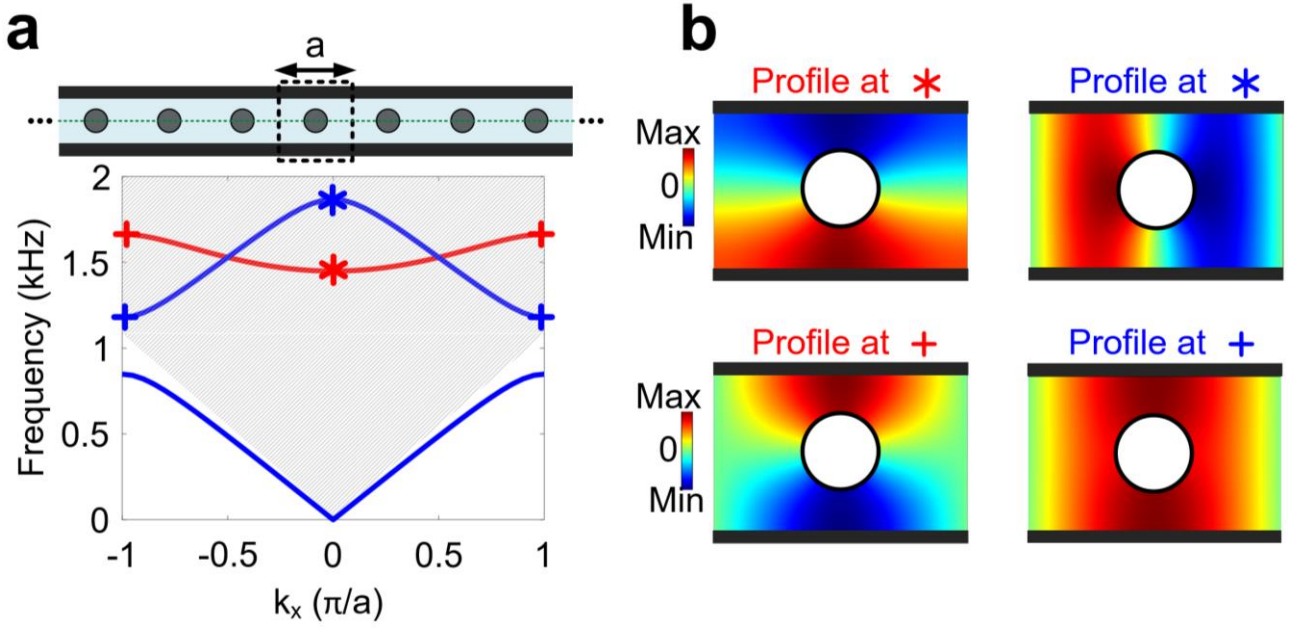
Figure 4.3: Independent topological subspaces in an acoustic waveguide. a, Band structure of an acoustic parallel plate waveguide (with a plate separation of 10 cm) containing obstructing cylinders (with a diameter of 5 cm) placed on its center line, arranged in aperiodic lattice. The red band is the dispersion of an odd-symmetric eigenmode (originating from evanescently coupled symmetry-protected bound states in the continuum), while the blue bands correspond to regular sonic crystal bands with even mode symmetry. The gray area represents the empty waveguide continuum. b, Profiles of the odd and even modes at specific Bloch wave numbers [196].

odd-symmetric modes originate from symmetry-protected bound states in the continuum (BICs), explained before.

Interestingly, the odd band behaves differently than the even bands upon scaling: while shrinking the lattice constant shifts all the even bands up in frequency, the position of the BIC band stays constant (it only gains some dispersion as the BICs couple more efficiently). This effect is demonstrated in Fig. 4.4a-c, indicating the calculated band structure of the crystals for different lattice constants, namely a, $1.25a$, and $1.4a$. The fact the odd and even modes behave differently when the crystal is scaled allows us to overlap the second blue band and the first red band in Fig. 4.3a, creating two uncoupled physical subspaces whose topological properties can be further simultaneously engineered, as I now demonstrate.
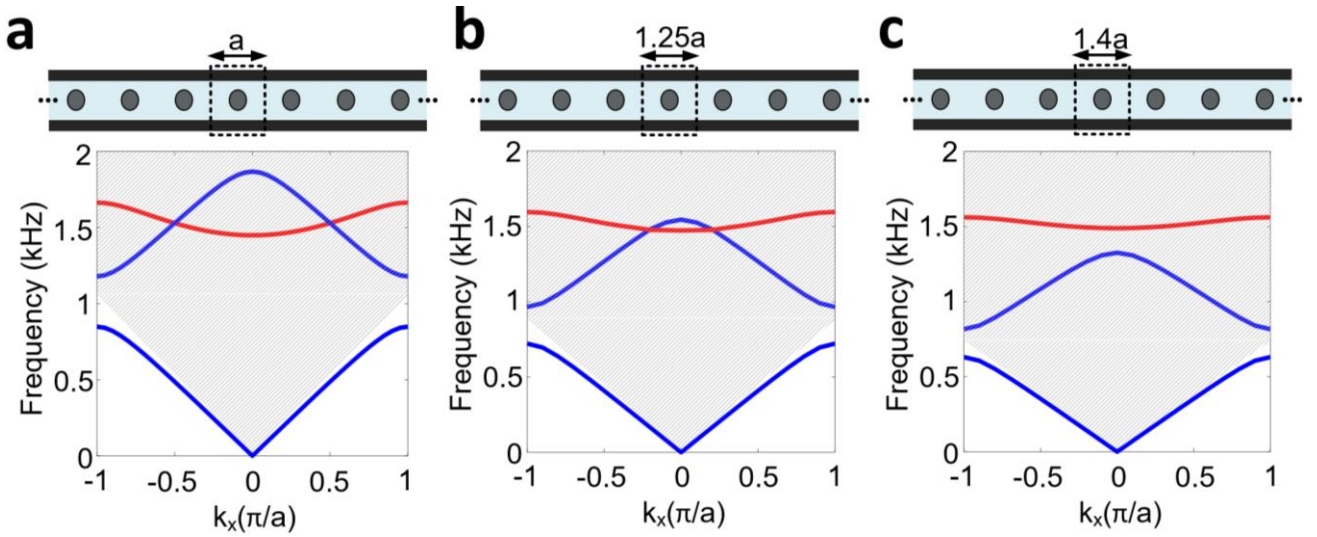
Figure 4.4: Effect of scaling the lattice constant on the band structure of the system under study. a, Band structure of the system when the lattice constant is assumed to be $a = 16.3\ cm$. The waveguide continuum is marked with the grey area, b,c, Same as panel a except that the lattice constant is increased to $1.2a$ and $1.4a$, respectively. The blue dispersion bands corresponding to the even eigenstates are moved to the lower frequency range, whereas the position of the red band associated with the BIC mode is not affected [196].

To induce a nontrivial topology in such one-dimensional periodic structure, I first double the size of the unit cell, now considering the lattice as a repetition of cylinders pairs, which effectively folds the band structure. Next, I lift the degeneracies of the new band structure at the folding pointsby reducing or increasing the distance between the two cylinders within the new extended unit cell. The top insets of Figures 4.5a and b illustrate the geometries of the associated shrunk and expanded lattices, respectively. The bottom insets report the corresponding band structures, where the bands are colored according to the previously explained symmetry classification. Although both configurations exhibit exactly the same band structure, they are topologically distinct, as it was discussed in the previous chapter. In particular, the expanded crystals correspond to a non-trivial topological origin, whereas the shrunk lattice is trivial from the topological point of view. I further emphasize, that in contrast to prior arts about1D topological insulators, the proposed configuration supports two distinct topological subspaces characterized by their different symmetries. This allows two edge modes with distinct lifetimes to coexist at a phase transition interface and induce the Fano
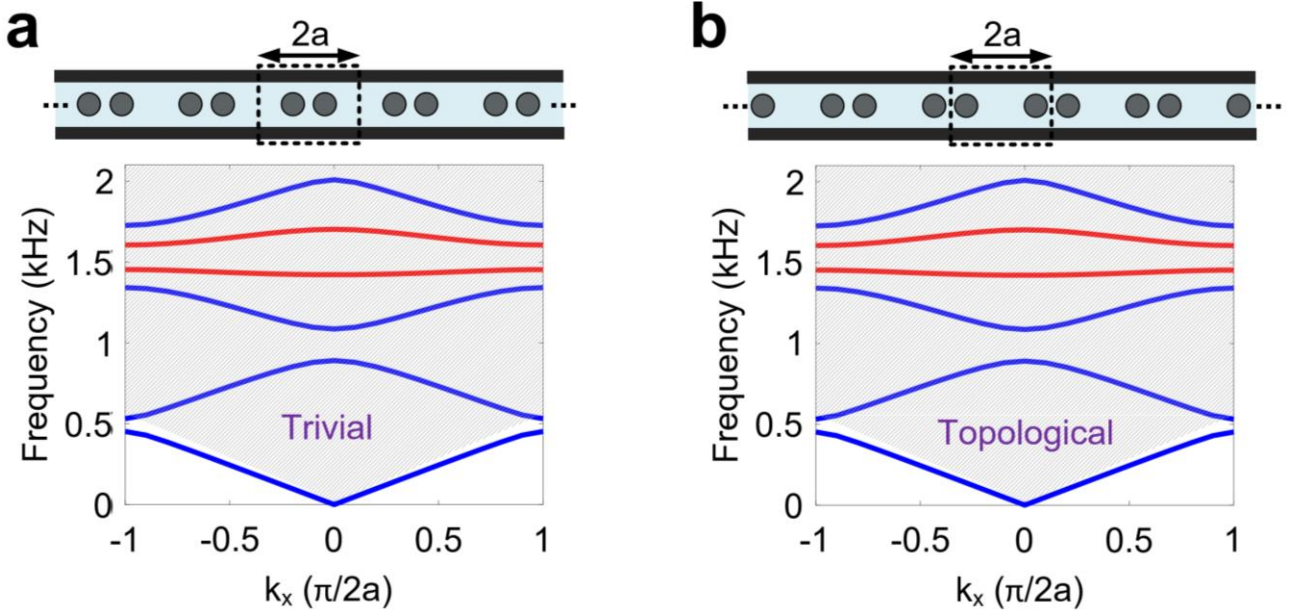
Figure 4.5: a, Band structure of the crystal when considering the extended unit cell (which includes two periods), and reducing the distance between the two obstacles with respect to the folded case. b, Same as panel (a) except that the distance between the obstacles is increased [196].

spectral line shape (instead of a Lorentzian one demonstrated before), as I will show below.

To form the topological Fano resonance, I now consider the topological edge states that form at an interface between these two crystals around 1.5 kHz. Note that the system is properly scaled such that the topological band gaps of both the even and odd subspaces overlap around this frequency. I form a finite-size system made of four crystal cells on each side of the interface. Similar to our previous classification, the corresponding edge states can be categorized into two classes: the dark edge state stemming from the BIC mode, distinguished by its odd profile, and the bright one originating from the even modes. The mode profile of these two different types of edge modes are shown in Figure 4.6a and b, respectively. The two-port system is then excited by a plane wave incident from the left (Fig. 4.7a, top) and the transmission coefficient is extracted (bottom plot in Fig. 4.7a). As observed, the spectrum shows a single peak right at the resonance frequency of the bright edge mode (the red dashed line), because the incident plane wave cannot excite the odd-symmetric (dark) edge mode. To let, instead, the bright and dark modes interact and create a topological Fano resonance, we must break the vertical inversion symmetry and slightly move all
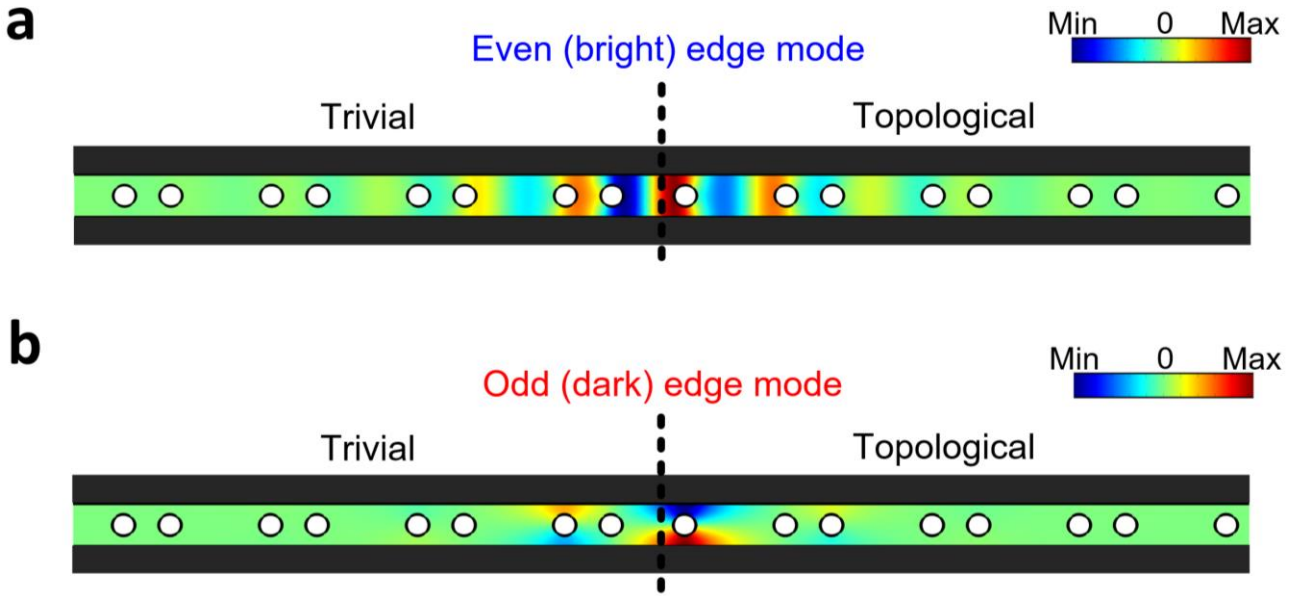
Figure 4.6: Field profile of the edge states formed at the interface between the two insulators. a, Field profile of the even edge mode originating from the radiation modes, b, Field profile of the odd edge mode stemming from the BIC mode. Although both even and odd edge modes are bounded to the interface, only the even edge mode offers a finite resonance linewidth as the odd edge mode is completely decoupled from the radiation continuum due to its different symmetry [196].

cylinders up (or down) from the centerline. Doing so indeed yields the expected Fano line shape (the solid blue line). Note that, both of the obtained bright and dark resonances are of topological nature, and the origin of the Fano resonance is indeed rooted to the topological properties of the surrounding bulk insulators. Therefore, we expect the presence of the Fano resonance to be guaranteed even in the presence of disorder, as long as it is not strong enough to close the band gaps. To test this hypothesis, I randomly changed the positions of the obstructing circles in Fig. 4.7b (1.5 cm average shift with no preferred direction) and repeat the scattering experiment. The transmission spectrum of the waveguide, represented in Fig. 4.7b (bottom panel), reveals three important properties. Despite the large degree of disorder, (i) the Fano resonance is still present, (ii) the Fano shape is not disturbed by any new localized mode (which would add new peaks or dips), (iii) the Fano resonance can shift and is still sensitive to environmental changes. These features remain true for any realization of disorder.
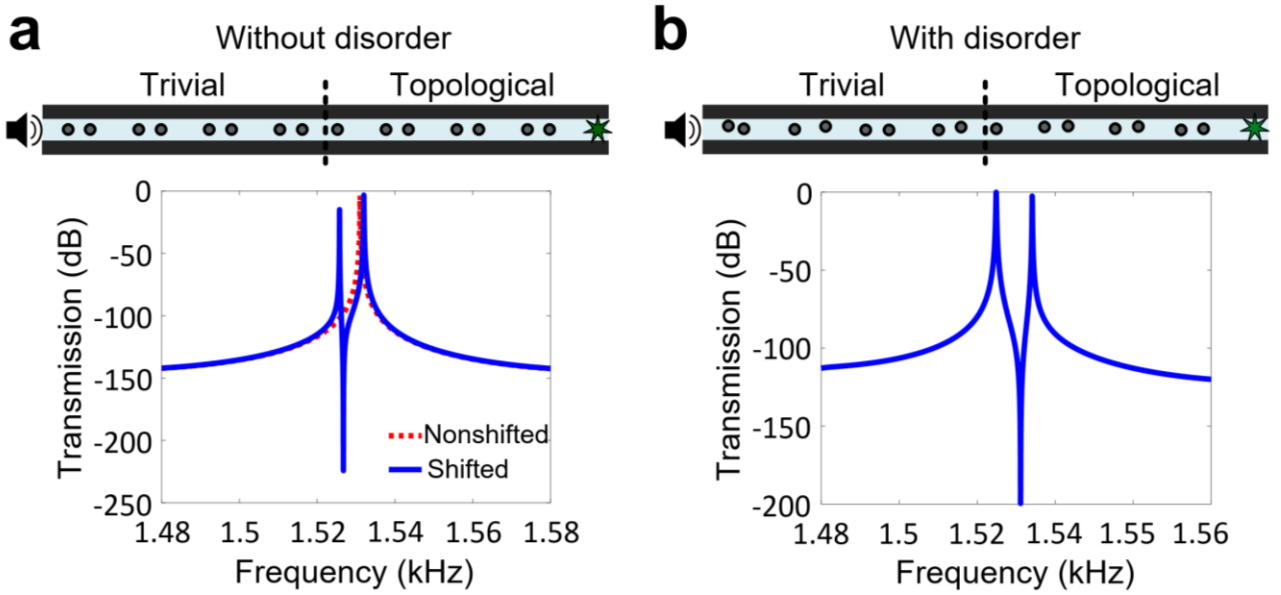
Figure 4.7: Full-wave numerical demonstration of topologically protected Fano resonances. a, Four unit cells from the trivial lattice are connected to four cells from the nontrivial system. By sending a plane wave from the left, only the even edge mode can be excited (the red dashed line), leading to only one resonance in the transmission spectrum. This is no longer the case if the obstacles are slightly shifted away from the centerline, allowing even and odd modes to interact, and inducing a topological Fano resonance (the solid blue line). b, Transmission spectrum of the waveguide when the obstacles are randomly moved from their original places. The Fano line shape is preserved due to topology [196].

Next, I compare the robustness of the topological Fano to the one of a topologically trivial Fano resonance, such as the one considered in Fig. 4.8, which is based on bright and dark resonant defect tunneling through a Bragg band gap. As it is observed, the trivial Fano spectrum is deeply the presence of disorder, which induces new localized states that destroy its characteristic shape (Fig. 4.8b). In order to unambiguously demonstrate the superiority of topological Fano resonances to trivial ones, we report in Fig. 4.9a and b the evolution of the Fano line shape versus disorder strength for the topological and trivial cases, respectively. Comparing these two parametric plots, we see that the topological Fano resonance survives disorder levels that are 10 times stronger than the ones required for breaking the trivial Fano, which is quickly destroyed by a disorder-induced localized mode. These findings broadly demonstrate the great advantage of topological Fano resonances over trivial ones.

I next constructed a prototype to experimentally demonstrate the topological Fano resonance and examine its much-sought robustness. I used an acrylic extruded clear square tube as the acoustic waveguide. Nylon 6 continuous cast black rods were manually embedded inside the waveguide to implement the topological chain under study.
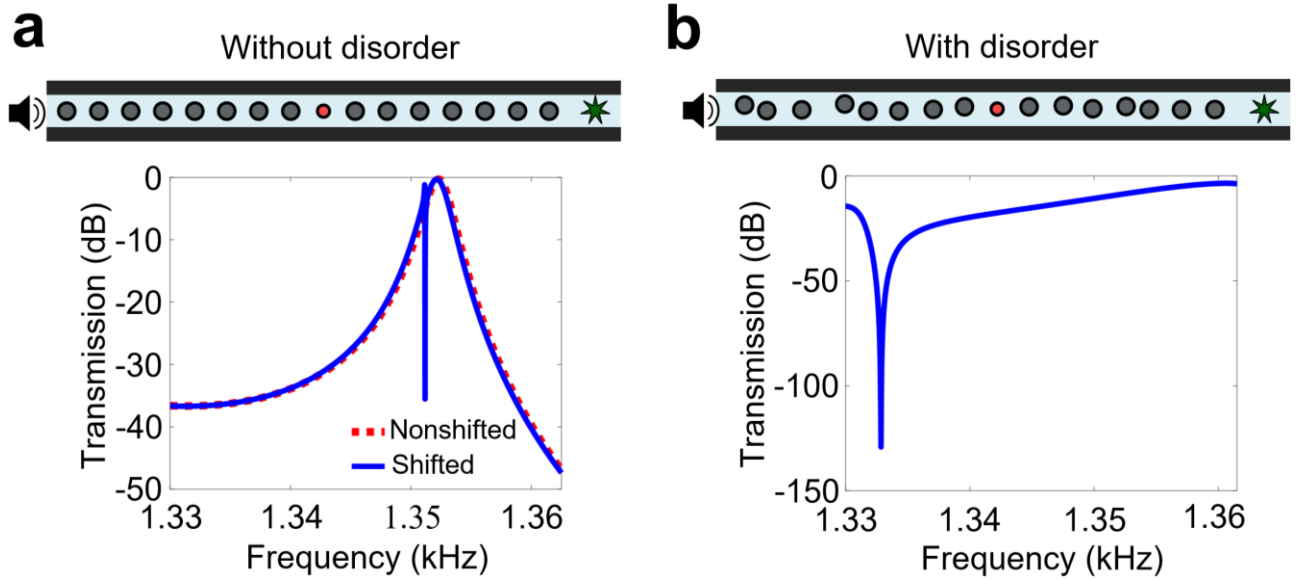
Figure 4.8: Full-wave numerical demonstration of the excessive sensitivity of trivial Fano resonances. The figure repeats the analysis of Fig. 4.7, but for a trivial Fano resonance induced by defect tunneling through a Bragg band-gap, a, Transmission spectrum of the system when no disorder is present in the system, b, Transmission spectrum of the system when some disorder is introduced to the system [196].
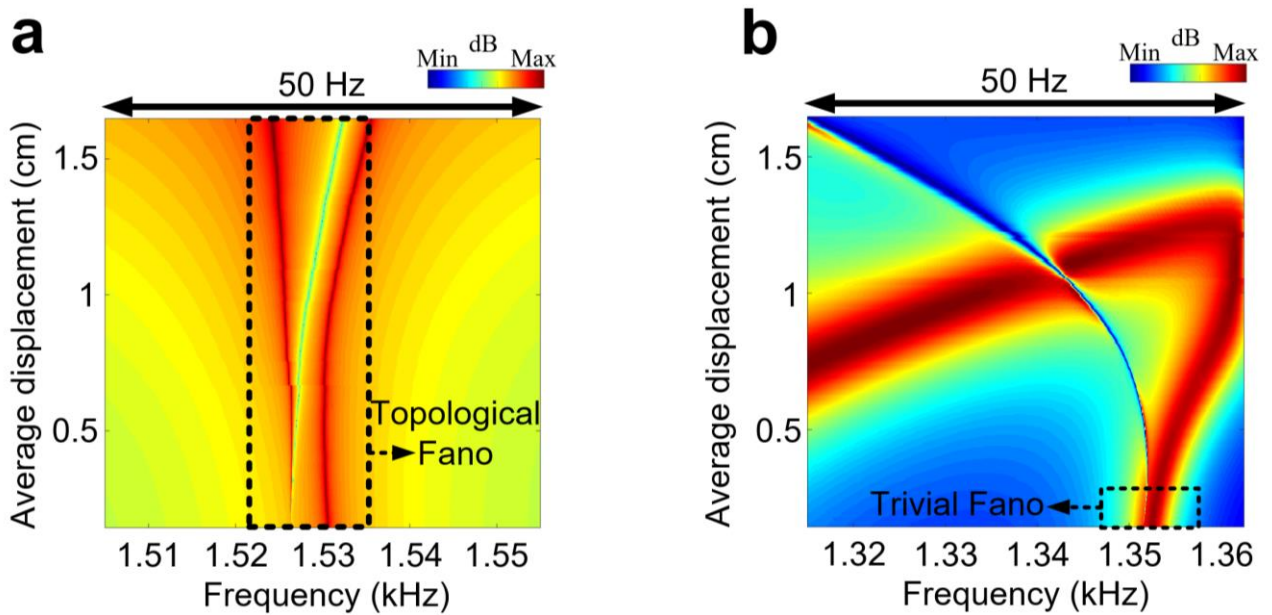
Figure 4.9: Evolution of the transmission spectrum versus disorder strength for topological Fano resonance (a) and trivial Fano resonance (b). The results of the figure broadly demonstrate the great advantage of topological Fano resonances over trivial ones [196].

Simulations predict a topological Fano resonance around the frequency $f_0 = 2.3\,kHz$. To confirm this prediction, I sent burst noise from the left of the system, whereas the right-hand side port was connected to a broadband anechoic termination. I then measured the corresponding transmission coefficient, which is represented in the bottom panel of Figure 4.10a (blue line) and compared it to the simulation results (dashed red line). As expected, we observe the topological Fano transmission
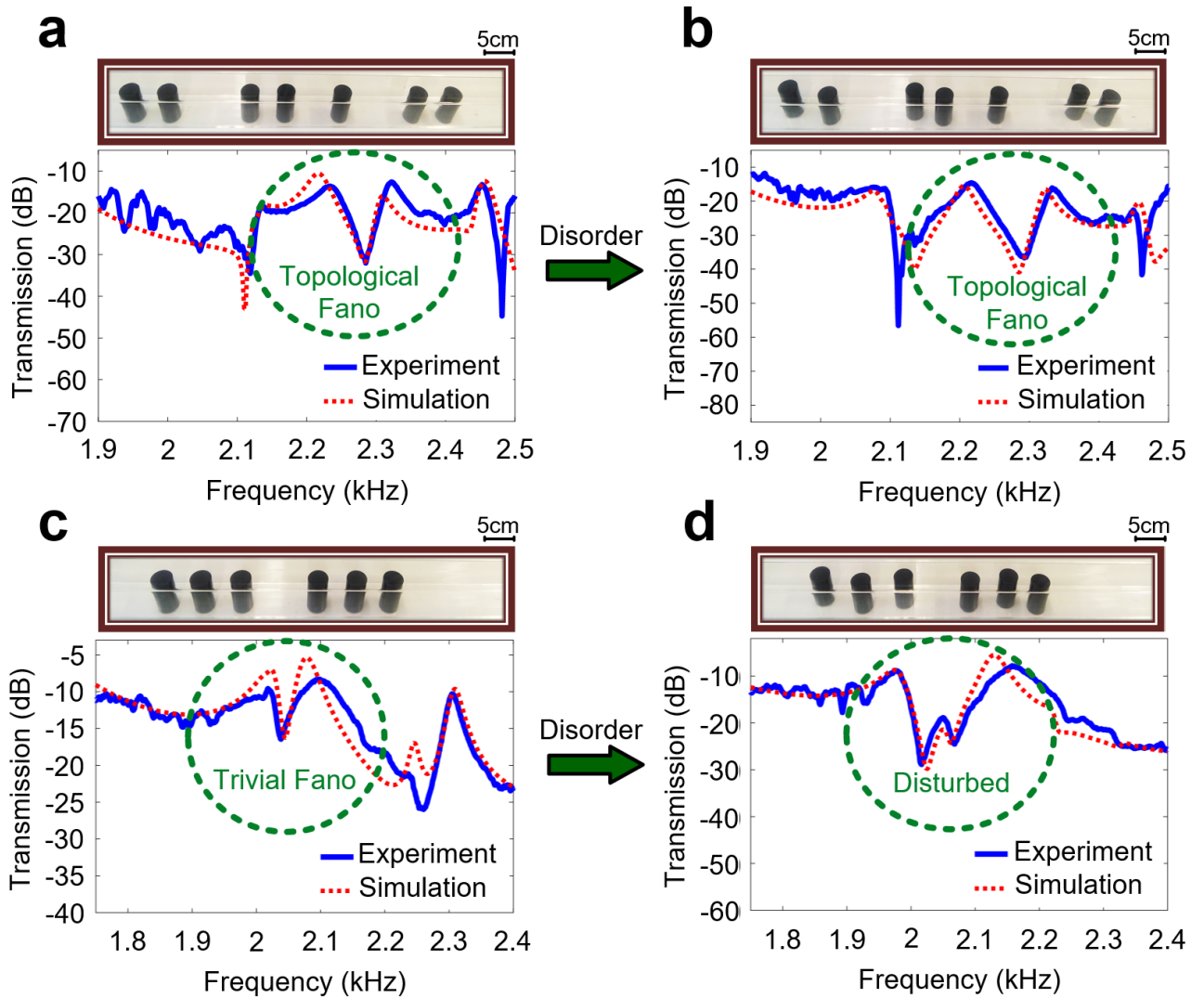
Figure 4.10: Experimental validation of topological Fano resonances. a, Nylon black rods are embedded inside a transparent square acoustic waveguide, implementing a scattering experiment analogous to Fig. 4.8a. The structure supports a topological Fano resonance around the frequency $f_0 = 2.3\,kHz$ as observed in the bottom panel. b, The obstructing rods are randomly moved away from their original positions, introducing position disorder. The Fano line shape is maintained. c,d, Same as a,b for a trivial Fano resonance induced when coupling a topologically trivial Bragg defect mode and a BIC [196].

spectrum (circled in green), with very good agreement with simulations. Next, I randomly moved the obstacles from their real positions to get the disordered configuration shown in the top panel of Fig. 4.10b. The measured transmission coefficient, represented in the bottom panel, demonstrates that the Fano lineshape is indeed perfectly preserved, despite the large level of disorder (1 cm average shift, i.e., 14% of the waveguide width, with no preferred direction).

To confirm the topological origin of this property, I repeated the scattering experiment for a (trivial) Bragg-induced Fano resonance obtained from a periodic lattice with a missing center rod at the center (total of six rods, slightly up-shifted with respect to the centerline, see Fig. 4.10c). Numerical simulations show that the missing rod creates an even defect mode overlapping with an odd dark state carried by the Bragg structure, i.e., a trivial Fano resonance. The measured spectrum exactly confirms these predictions. By adding, in Fig. 4.10d, the same level of disorder as in Fig. 4.10b, it is clear that the initial Fano shape of the resonance is extremely affected: the characteristic peak-and-dip shape of the Fano is completely destroyed, and a new dip is added to the spectrum. Such drastic deformations would be highly detrimental in any sensing application, which are usually based on tracking the shift of a single Fano dip.

4.3 Electromagnetic topological Fano resonances

While in the previous section, I demonstrated topological Fano resonances in the context of acoustics, they can be easily transferred to other areas of classical physics such as electromagnetics. Here, I demonstrate how topological Fano resonances can be obtained for electromagnetic waves. Consider a microwave parallel plate waveguide with the palate separation of $2h$ (Fig. 4.11a). Since the waveguide is infinite in the out-of-plane direction, the solution to Maxwell equations can be decomposed into transverse electric (TE) and transverse magnetic (TM) parts. Here, without loss of generality, I investigate the TE part and assume that the electric field is polarized along out of plane direction. By solving the corresponding equations for the E_z component of the field, one can easily

find that the resulting eigen-modes (E_z) are required to be even with respect to the centerline, and have a cutoff frequency of $f_c = \pi c / 2h$ ($c = 3 \times 10^8 \, m/s$ is the speed of light).
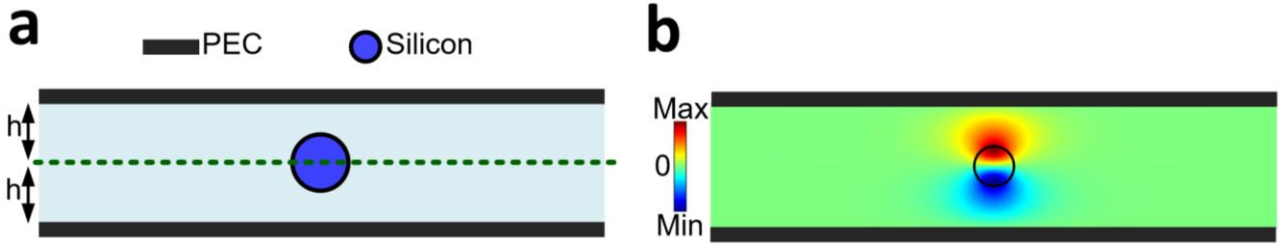
Figure 4.11: Electromagnetic bound states in the continuum a, A microwave parallel plate waveguide containing a single silicon rod placed on the centerline is considered. b, Profile of the corresponding bound state forming within the radiation continuum of the waveguide [196].

Suppose now a circular dielectric obstacle (a silicon rod) is placed right at the centerline. The dielectric rod supports a set of resonances whose E_z components can be even or odd with respect to the centerline. If the resonance frequency of one of the odd dielectric modes falls above the waveguide cutoff (f_c), it can coexist in the radiation continuum of the even waveguide modes, while, simultaneously, remaining perfectly bounded to the rod due to its different symmetry. Fig. 4.11b (second panel) depicts the profile (E_z component) of the corresponding BIC mode obtained via FEM simulations.

Now that I successfully realized a bound state in the radiation continuum of the waveguide, I pursue the same procedure as the acoustic case to achieve a topological Fano resonance. I first form a periodic lattice of the dielectric obstacles and calculate its dispersion (Fig. 4.12a). The dispersion bands are colored according to the symmetry of their eigenmodes represented in Fig. 4.12b. I further note that, similar to the acoustic case, one can adjust the frequency of the radiation (even) modes by scaling the lattice constant, whereas the position of the dispersion band of the BIC (odd) mode is not affected by scaling. This allows one to induce independent topological subspaces in the mono-mode microwave waveguide under investigation, as explained before.

Consider now the configuration of Fig. 4.13a, where different topological phases are induced by detuning the extra-cell and intra-cell couplings between the dielectric resonators. The profiles of the corresponding even and odd edge modes are shown in the second and third panel,
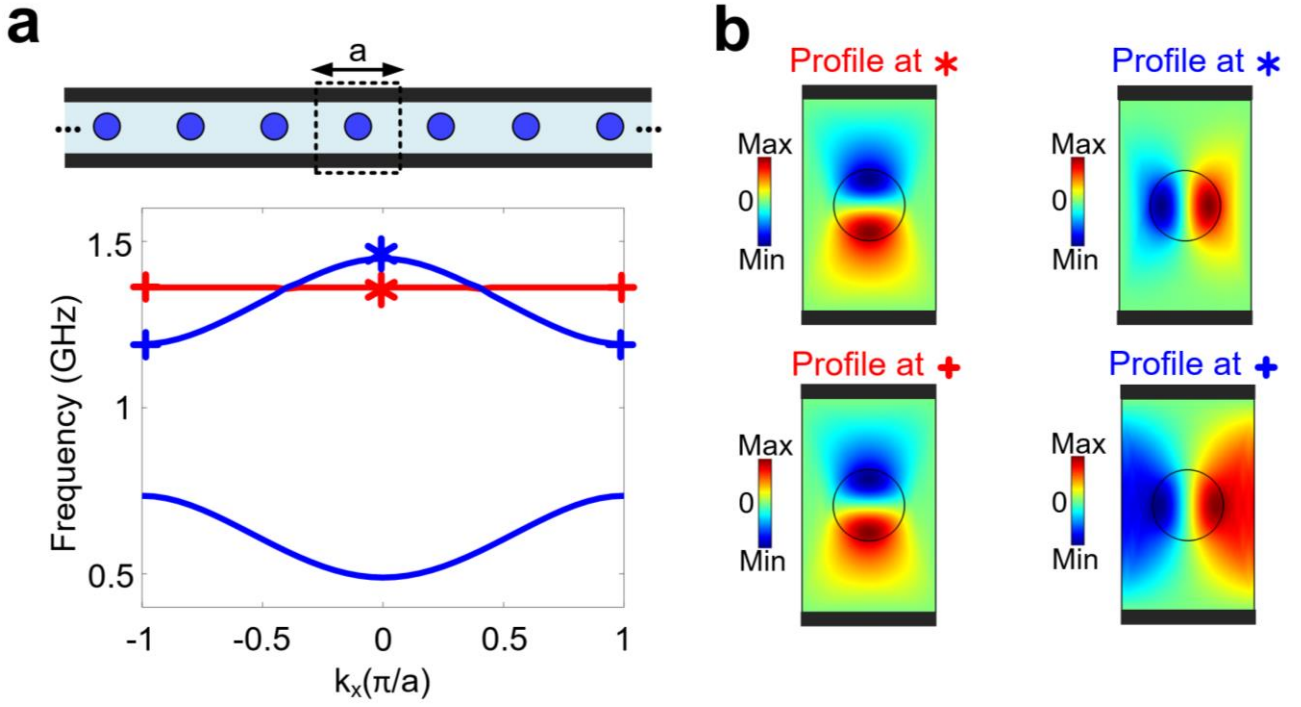
Figure 4.12: Independent topological subspaces in a microwave waveguide, a, We consider aperiodic lattice of silicon rods inside the waveguide. The BIC (odd) mode has a low-dispersive behavior (the red band), while the radiation (even) modes exhibit a stronger frequency dispersion (blue bands). b, Profile of the even and odd eigenstates at certain Bloch wavenumbers [196].

respectively. By subtly choosing the lattice constant, I have made the odd edge mode coexist within the spectral range of the even mode. The scattering experiment (Figure. 4.13a, bottom panel, dashed red spectrum), however, reveals only the presence of the even edge mode since the odd edge mode is decoupled from even-symmetric waves. By slightly moving the dielectric resonators from the centerline, however, a topological Fano resonance emerges as a result of the small leakage of the odd edge mode to the radiation waves (the solid blue line). Just like in acoustics, the obtained Fano resonance is expected to be robust against disorder. To assess this robustness, I randomly change the position of the resonators to achieve the largely disordered configuration of Fig. 4.13b (first panel, average shift is 4.6% of h, with no preferred direction). Shown in the second and third panels are the profiles of the corresponding even and odd edge modes, respectively. Notably, the resonance frequencies of both bright and dark resonances can shift but no Anderson localization occurs. The resulting Fano line shape is therefore expected to be preserved. This is indeed evident from the

transmission spectrum of the waveguide in the fourth panel, confirming the high robustness of the

achieved topological Fano resonance (obtained based on electromagnetic waves).
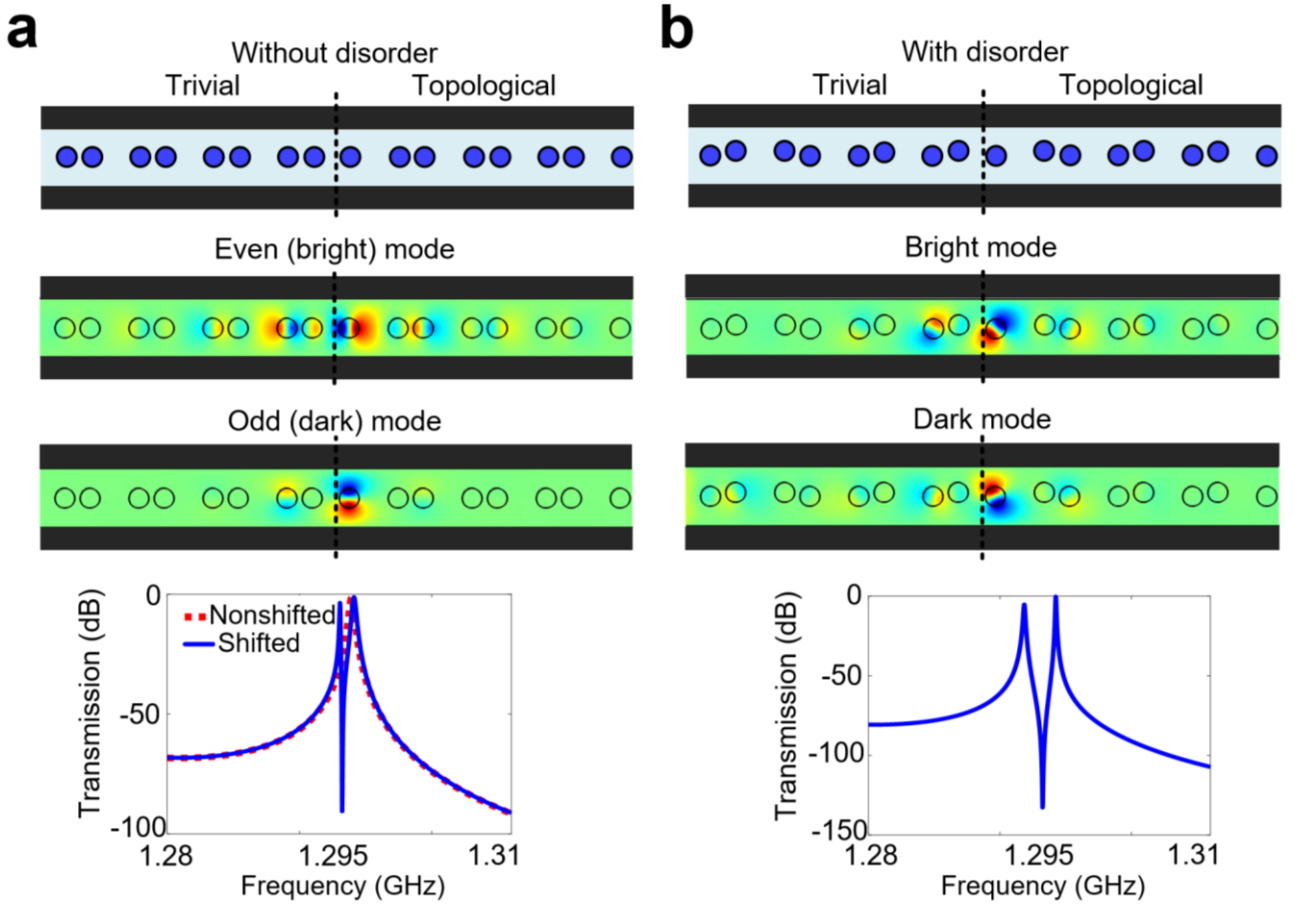
Figure 4.13: Electromagnetic topological Fano resonances: a, Ideal case without position disorder, for a system of dielectric rods in a parallel plate waveguide. A topological Fano resonance is observed. b, Same as panel a) but for in the presence of position disorder. The presence and shape of the Fano resonance is protected against disorder by the topology of the bulk insulators [196].

4.4   Analog signal processing based on topological Fano resonances

The spectral characteristics of Fano resonances are different from ordinary Lorentzian resonances, which are created by the excitation of a single resonance state. Because of this reason, in temporal domain, they correspond to a relation which is different from the first order ODE proposed in Eq. 3.1. Suppose that the resonance frequencies of the bright and dark resonances are ω_1 and ω_2, respectively. The transfer function associated with the Fano resonance caused by the interference between these two resonances can be approximated by

$$H(\omega_1, \omega_2) = \frac{1}{-(\omega - \omega_1)(\omega - \omega_2) + j\big(\gamma_1(\omega - \omega_1) + \gamma_2(\omega - \omega_2)\big) + \gamma_1\gamma_2 - \kappa^2} \tag{4.1}$$

in which γ_1 and γ_2 are decay rates corresponding to the bright and dark states respectively, and κ is the coupling coefficient between bright and dark states. Let us suppose first that the input signal is modulated at the frequency of the bright state, i.e. ω_1. By taking an inverse Fourier transform from Eq. 4.1, one can derive the corresponding temporal relation of H as

$$d^2f(t)/dt^2 + (\gamma_2 + j\Delta\omega)\,df/dt + (\gamma_1\gamma_2 - \kappa^2 + \gamma_1 j\Delta\omega)f(t) = g(t) \tag{4.2}$$

in which $\Delta\omega = \omega_1 - \omega_0$. This implies that any system supporting Fano resonance can be pictured as an equation solver solving the equation given in Eq. 4.2. As evident from the relation given in Eq. 4.2, the corresponding constant coefficients can be tuned by changing the quality factors of the dark and bright states, as well as the coupling coefficient κ.

4.5   Conclusions

To conclude, in this chapter, I demonstrated the concept of topological Fano resonance. The theoretical and experimental findings provided in this chapter demonstrated the superior

robustness of topological Fano resonances over trivial Fano resonances. In particular, topology forced the archetypal Fano line shape to occur in the desired frequency range, as long as the level of disorder is not strong enough to close the surrounding topological band gaps. The obtained experimental results shows that obtaining a topological Fano resonance does not require tight geometrical tolerances, very different from trivial Fano resonances. In addition, topological Fano resonances are still sensitive to environmental changes, and tracking the shift of the Fano dip may allow for a new generation of sturdy sensors.

Apart from its relevance for signal processing tasks, the concept of topological Fano resonance proposed in this chapter holds promise in many applicative fields, including phononic, photonic, and plasmonic sensing technologies and or biomolecular detection.

Chapter 5 Topological random analog signal processing

This chapter is a modified version of the materials reported in [213].

5.1 Introduction

As discussed in the previous chapters, the performance of most wave systems, in particular, analog signal processors is largely impeded by disorder. Even at very low concentration, impurities or geometrical imperfections can cause severe self-interference effects, largely hindering wave propagation and device performance. I demonstrated in the previous chapters that the much-sought topological protection of topological insulators can significantly alleviate the detrimental effects of disorder on wave propagation, enabling the realization of robust analog signal processors that maintain their original functionality in the presence of impurities.

Although topological insulators have somewhat enhanced the robustness of analog wave systems to disorder, their topological protection is still limited by a phenomenon, known as Anderson localization (AL) [211]. This process, occurring in the regime with dominating randomness, progressively fills the band gap of the TI with disorder-induced localized bulk states, destroying the insulating topological phase and impeding the transportation of the corresponding boundary state. Such a behavior seems to be disappointing at first glance, because it implies that even topological wave systems become fragile when the disorder level is high enough to turn the TI into an ordinary insulator. Yet, the mere fact that introducing disorder to a

system can induce a topological phase transition is encouraging, because it suggests that the opposite transition might, in principle, be possible. Recently, in a remarkable development [212], it was theoretically demonstrated that some trivial insulators with specific parameters can indeed go through a topological phase transition upon introducing disorder, converting them to TIs with robust conductive states flowing on their boundaries. Soon after, these exotic topological phases, referred to as disorder-induced topological insulators or topological Anderson insulators (TAIs), were experimentally observed in different physical platforms [213-215].

In this chapter, I demonstrate, both theoretically and experimentally, that the much-sought disorder-induced character of TAIs is relevant for realizing an unconventional generation of analog signal processors that not only are not restricted by disorder but also owe their proper functionality to disorder. I demonstrate this by proposing a novel class of wave-based computing systems that, in a regime of strong randomness, perform advanced, non-random computational tasks such as image processing and equation solving. These findings, defying the conventional view that disorder is detrimental for realizing well-defined analog functionalities, provide a roadmap for the realization of a large variety of disorder-induced wave systems in which disorder acts as a powerful engine, forcing the system to perform the functionality of interest.

5.2   Acoustic topological signal processors

I start again with considering the tight-binding toy Hamiltonian of the Su-Schrieffer–Heeger (SSH) chain expressed as

$$H = \sum_n \omega_0 a_n^\dagger a_n + \sum_n K a_{2n-1}^\dagger a_{2n} + \sum_n J a_{2n}^\dagger a_{2n+1} + H.C. \tag{5.1}$$

in which $a_n^\dagger$, a_n are creation and annihilation operators for the site n, K, and J stand, respectively, for the intra-cell and extra-cell coupling coefficients, and $\omega_0 = 1$ is the on-site

energy of the atoms. Let us suppose that the parameters K and J are defined as $K = K_0(1 + 0.5D_sW)$ and $J = J_0(1 + D_sW)$, in which $K_0 = 0.1$, $J_0 = 0.09$, D_s is a parameter quantifying the strength of disorder, and W is a site-dependent random number. Since $K > J$ in the clean limit ($D_s \to 0$), the disorder-free system corresponds to a trivial topological phase, characterized by a zero winding number. To induce a topological phase transition, I start to increase the intrinsic disorder of the system, now considering the case in which $D_s > 0$. Notice that, on average, regardless of D_s, the parameter K is always smaller than J. However, quite surprisingly, the difference in their standard deviations can create a topological phase transition in a certain range of values for D_s, leading to an insulator with non-trivial topological index (non-zero winding number) [214].
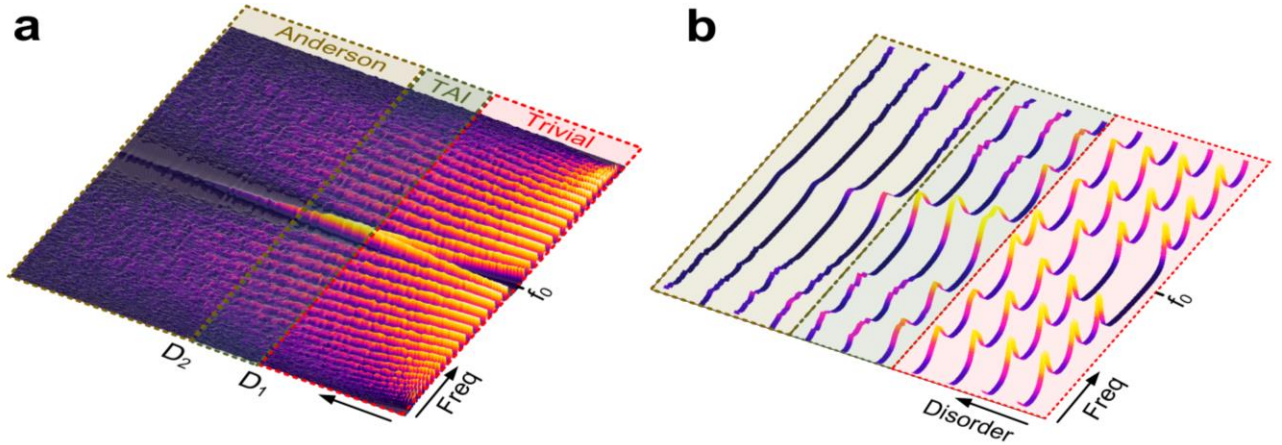
Fig. 5.1: Disordered version of Su-Schrieffer–Heeger model (SSH) model, a, Evolution of the corresponding (averaged) transmission spectrum versus disorder strength. Starting from an ordinary trivial insulator in the clean limit (red region), the system switches into a topological insulator in the regime $D_1 < D_s < D_2$ (TAI regime), characterized by a zero-energy edge state which manifests itself as a resonance peak in the spectrum. For extremely high disorder intensities (yellow region), the transportation is arrested by Anderson localization. b, Averaged transmission coefficient of the system for several representative disorder strengths. In the TAI regime (green area), the spectrum exhibits a Lorentzian profile near f_0, corresponding to the transfer function of a first order differential equation [213].
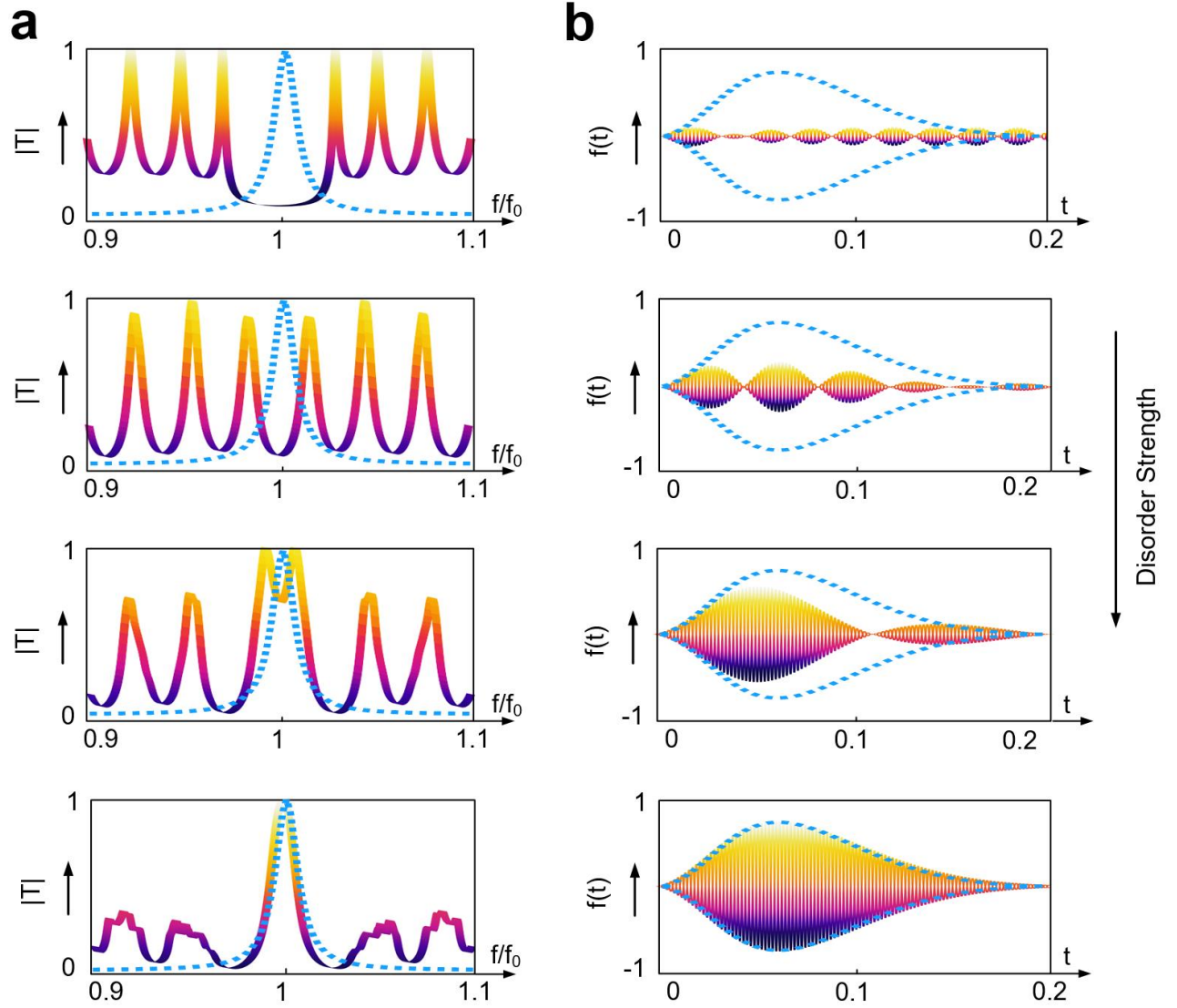
Fig. 5.2: Demonstration of disorder-induced equation solving. We suppose that the system is excited with a Gaussian-modulated sinusoidal signal and calculate (a) the corresponding transmission coefficient (T) and (b) output time signal ($f(t)$), when gradually increasing the disorder strength from zero to the regime of TAI. It is seen that disorder acts like an actuator in our system, triggering the proposed computing system to return the exact solution of the ODE that is aimed at solving (blue dashed line) [213].

In order to examine such a possibility, I consider a finite two-port scattering system made of 100 unit cells coupled to external waveguides and plot in Figure. 5.1a the disorder-averaged transmission spectrum versus the parameter D_s. As it is observed, in the disorder-free case, the
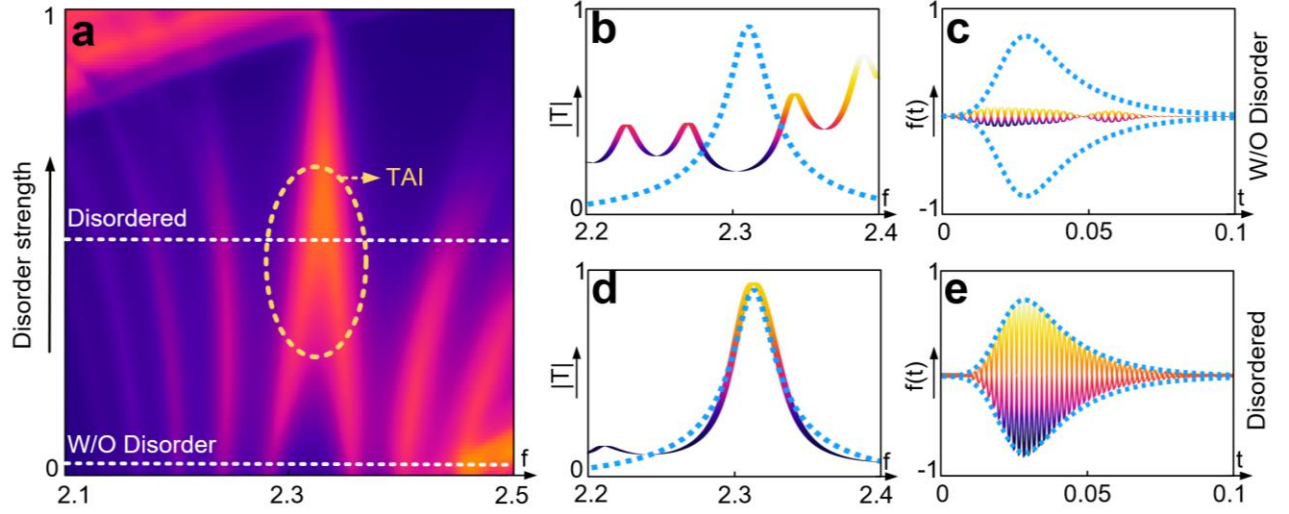
Figure 5.3: Numerical demonstration of topological random computing based on acoustic signals, a, Evolution of the (averaged) transmission coefficient of the phononic crystal as the strength of disorder is increased. The emergence of a disorder-induced zero-energy state is clear in the disorder-averaged transmission spectrum (oval region), allowing one to perform self-induced analog computing. b,c, Disorder-averaged transmission spectrum and the corresponding transmitted field, when the disordered-free system is excited with a Gaussian-type time-modulated signal. d,e, Same as b and c except that the system is sufficiently disordered, so that it finds itself in the TAI regime [213].

spectrum is gapped around f_0. This insulating band gap becomes narrower with increasing disorder strength, and is eventually closed at D_1. After D_1 (and before D_2), the band-gap re-opens but, this time, it includes a resonance peak emerging at the center of the gap. This in-gap resonance, corresponding to resonant tunneling through a topological edge state, indicates the non-trivial character of the system under investigation for $D_1 < D_s < D_2$ (TAI regime). If one increases the disorder level further ($D_s > D_2$), the onset of Anderson localization is reached, where all states start to localize in the bulk with decreasing transmission coefficient.

In Fig. 5.1b, I have plotted the disorder-averaged transmission coefficient for several representative disorder strengths. Notice that, in the TAI regime, the topological mid-gap resonance has a Lorentzian profile, following the general form of $H(\omega) = A/(Bj(\omega - \omega_0) + C)$ in the vicinity of ω_0.
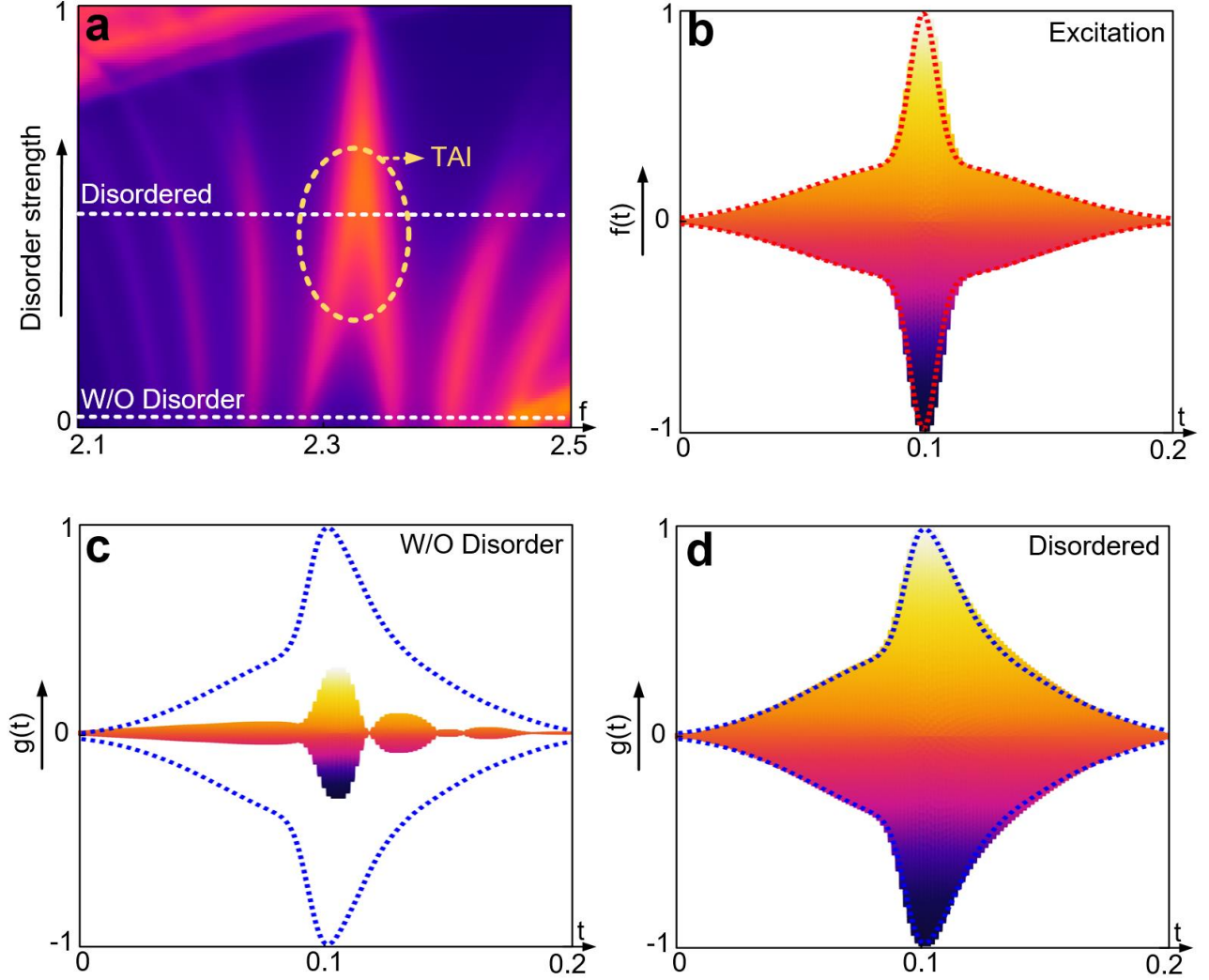
Figure 5.4: Numerical demonstration of topological random computing for an arbitrarily shaped signal. a, Disorder-averaged transmission coefficient of the proposed acoustic random computer versus disorder, b, We suppose that the system is excited with an irregularly shaped signal shown in the inset, c, Corresponding output signal in the disorder-free limit, being far from the solution of the target ODE aimed at solving. d, Corresponding output in the regime of topological Anderson phase [213].

As explained in Chapter 3, in temporal domain, $H(\omega)$ corresponds to the transfer function of a first order differential equation (ODE) of the form: $Bf'(t) + Cf(t) = Ag(t)$. It then follows that, for $D_1 < D_s < D_2$, the proposed disordered one-dimensional toy model can be pictured as a time-domain analog computing machine, that returns the solution of a definite first
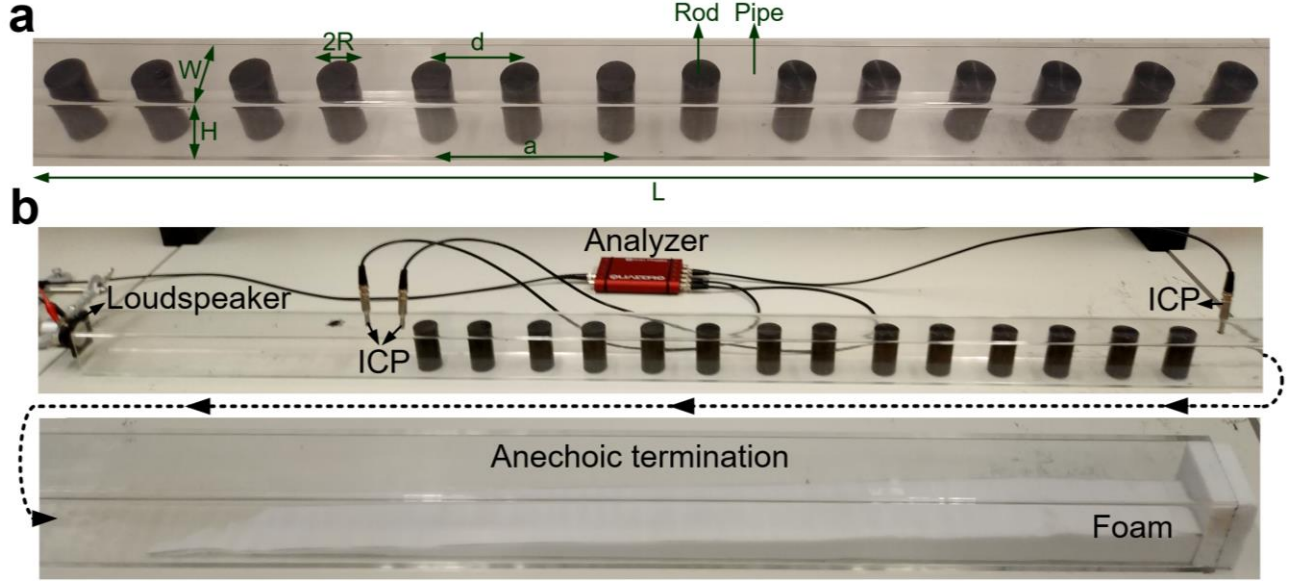
Figure 5.5: Experimental setup used to demonstrate topological random computers, a, The fabricated sample consisting of a rectangular pipe, taking the role of the acoustic waveguide, and a set of nylon cast plastic rods embedded inside the waveguide. b, In addition to the fabricated sample, the experimental setup consists of an acoustic Quattro Data Physics analyzer, three ICP® microphones, a loudspeaker and an acoustic termination, made from appropriately tampered foam [213].

order ODE at its output. Remarkably, such analog computer, while performing a definite task, has a disorder-induced character and an indefinite geometry, a property that directly stems from the underlying topological Anderson insulator phase.

In order to examine the functionality of the proposed analog computer, I assume that the system is excited with a Gaussian-modulated sinusoidal pulse, and calculate the corresponding disorder-averaged transmitted signal ($f(t)$) and transmission spectrum (T), when gradually increasing the disorder level from zero to the regime of TAI. The corresponding results are respectively depicted in Fig. 5.2a and b, illustrating how disorder forces the proposed disordered system to return the solution of the particular ODE that we wish to solve (the target analytical solution is marked with blue color).

To validate these findings in a full-wave 3D geometry, I mapped the model into a one-dimensional phononic crystal, built from a chain of acoustic quasi-bound states in the continuum (BICs) embedded in a monomode acoustic waveguide. Such coupled bound states, resonating at the frequency of $f_0 = 2310 \, Hz$, mimic the evanescently-coupled tight-binding chain described by the Hamiltonian of Eq. 5.1. In order to probe the system with far-field scattering tests based on the waveguide mode, I make the radiative quality factor of the bound states finite by slightly breaking the inversion symmetry of the structure with respect to its longitudinal axis. Fig. 5.3a represents the transmission coefficient (averaged over disorder realizations) as a function of both frequency and disorder strength, obtained via 3D full-wave numerical simulations based on the finite element method. The result of this figure confirms the emergence of a disorder-induced resonance peak, corresponding to the zero-energy states of the TAI phase (the oval region). The possibility to leverage the Lorentzian line shape of this resonance for carrying out disorder-induced filtering or equation solving is demonstrated in Fig. 5.3b-e, where I have reported the averaged transmittance of the system both in the clean limit and in the topological Anderson phase. When no disorder is imparted to the system, the transmission spectrum (Fig. 5.3b) exhibits a minimum due to a band gap around f_0, leading to an output signal (Fig. 5.3c) that is very different from the solution of the targeted differential equation (the blue curve, which is analytically predicted). In the regime of TAI phase, on the contrary, the transmission spectrum matches the desired transfer function $H(f)$ (Fig. 5.3d). As such, the corresponding transmitted signal, shown Fig. 5.3e, is nothing but the solution of the targeted ODE (blue curve). In Fig. 5.4, I have repeated the analysis for another type of excitation signal, having an arbitrary peculiar shape.
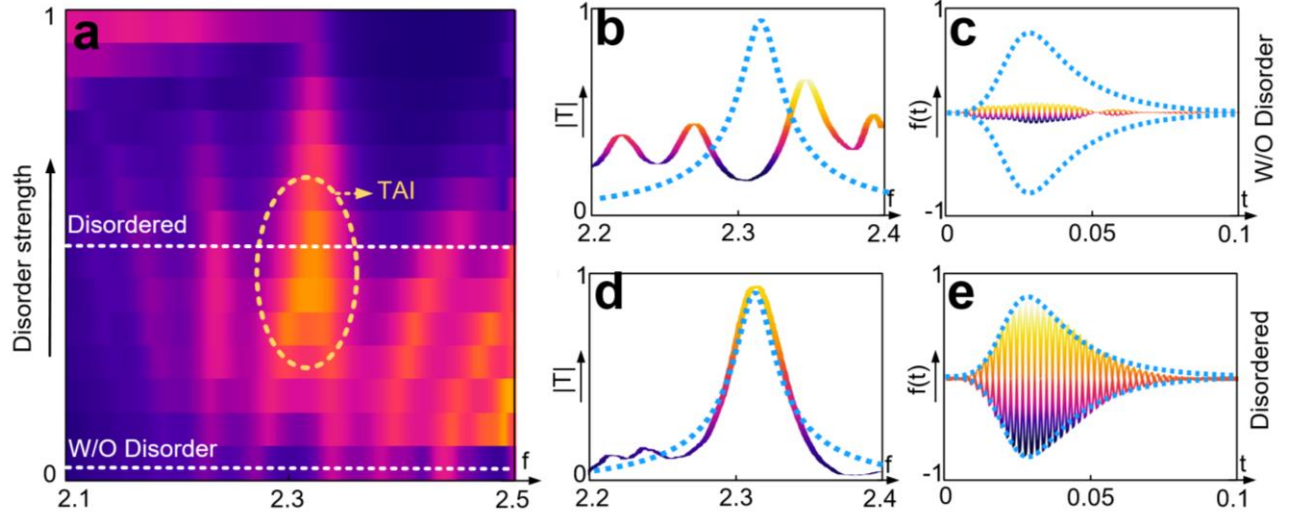
Figure 5.6: Experimental demonstration of topological random computers, a, Evolution of the (averaged) transmission coefficient of the phononic crystal as the strength of disorder is increased, obtained via 3D full-wave numerical simulations. The emergence of a disorder-induced zero-energy state is clear in the disorder-averaged transmission spectrum (oval region), allowing one to perform self-induced analog computing. b,c, Disorder-averaged transmission spectrum and the corresponding transmitted field (numerical simulations), when the disordered-free system is excited with a Gaussian-type time-modulated signal. d,e, Same as b and c except that the system is sufficiently disordered, so that it finds itself in the TAI regime [213].

I now experimentally verify these findings, based on a fabricated prototype of the system under study. The sample, shown in Fig. 5.5a includes a transparent pipe with square transverse cross-section, serving as a waveguide, and a chain of nylon cast scatterers, that are embedded inside the waveguide. The width, height, and length of the waveguide are $W = 7\,cm$, $H = 7\,cm$, $L = 2\,m$, respectively, the radii of the cylinders are $R = 1.75\,cm$, the lattice constant is $a = 16.6\,cm$ and the detuning parameter d is $d = 7.8\,cm$. The structure is tested in the experimental setup shown in Fig. 5.5b. Apart from the fabricated prototype, the setup includes three PCB 130F20 ICP® microphones, measuring the associated pressure field, a loudspeaker, generating sound and exciting the system, an acoustic Quattro Data physic analyzer, analyzing the associated measured data, and a computer, controlling the setup. Note also that, in order to
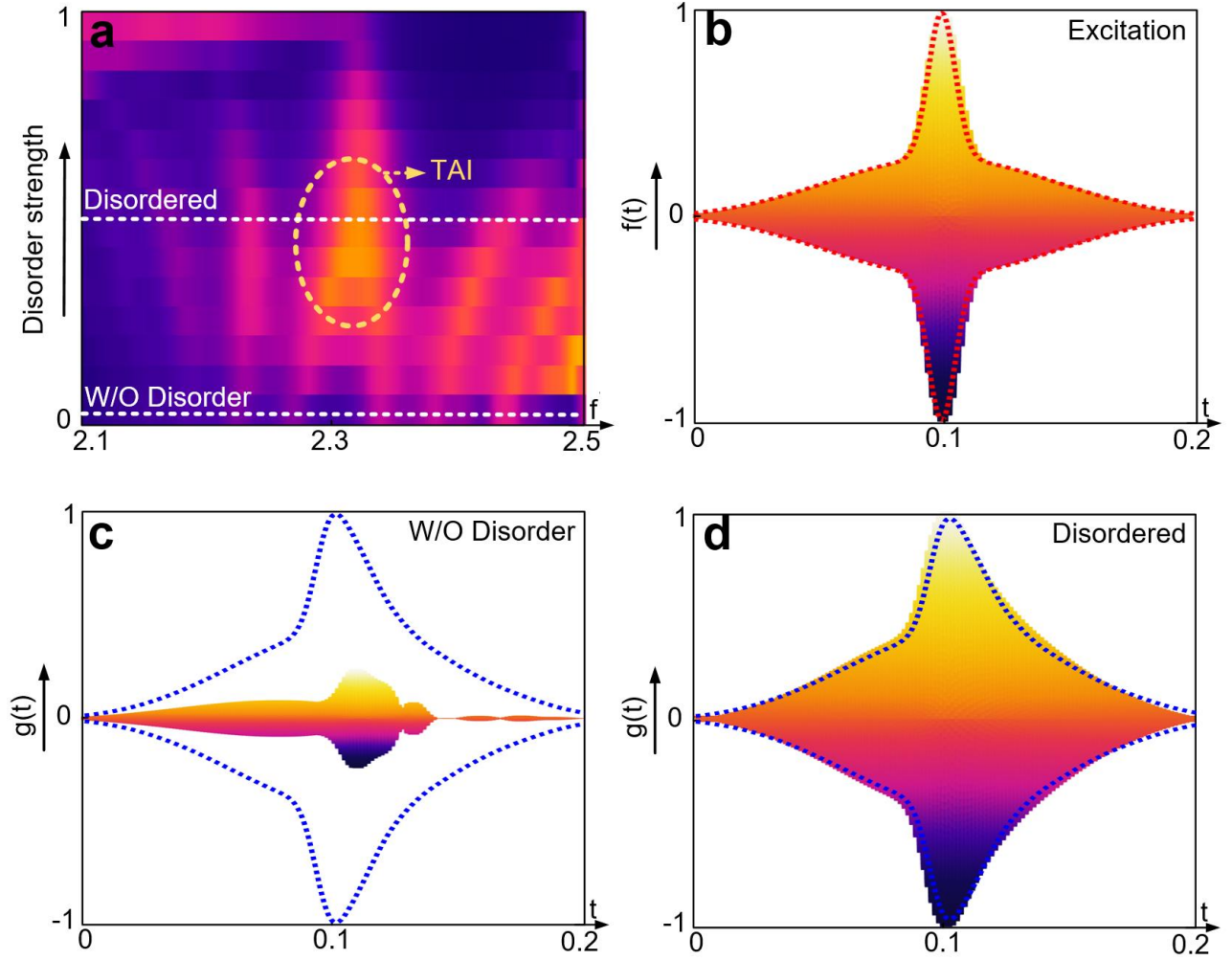
Figure 5.7: Experimental demonstration of topological random computing for an arbitrarily shaped signal. a, Disorder-averaged transmission coefficient of the proposed acoustic random computer versus disorder, b, The system is excited with an irregularly shaped signal shown in the inset, c, Corresponding output signal in the disorder-free limit, being far from the solution of the target ODE aimed at solving. d, Corresponding output in the regime of topological Anderson phase [213].

avoid unwanted reflection and refraction, the end of the system is terminated with an anechoic termination, made of an adiabatically tapered foam, shown in the bottom panel of the figure.

In order to extract the disorder-averaged transmission spectrum, I excited the system with the loudspeaker, and extracted the corresponding transmission spectrum for each realization of
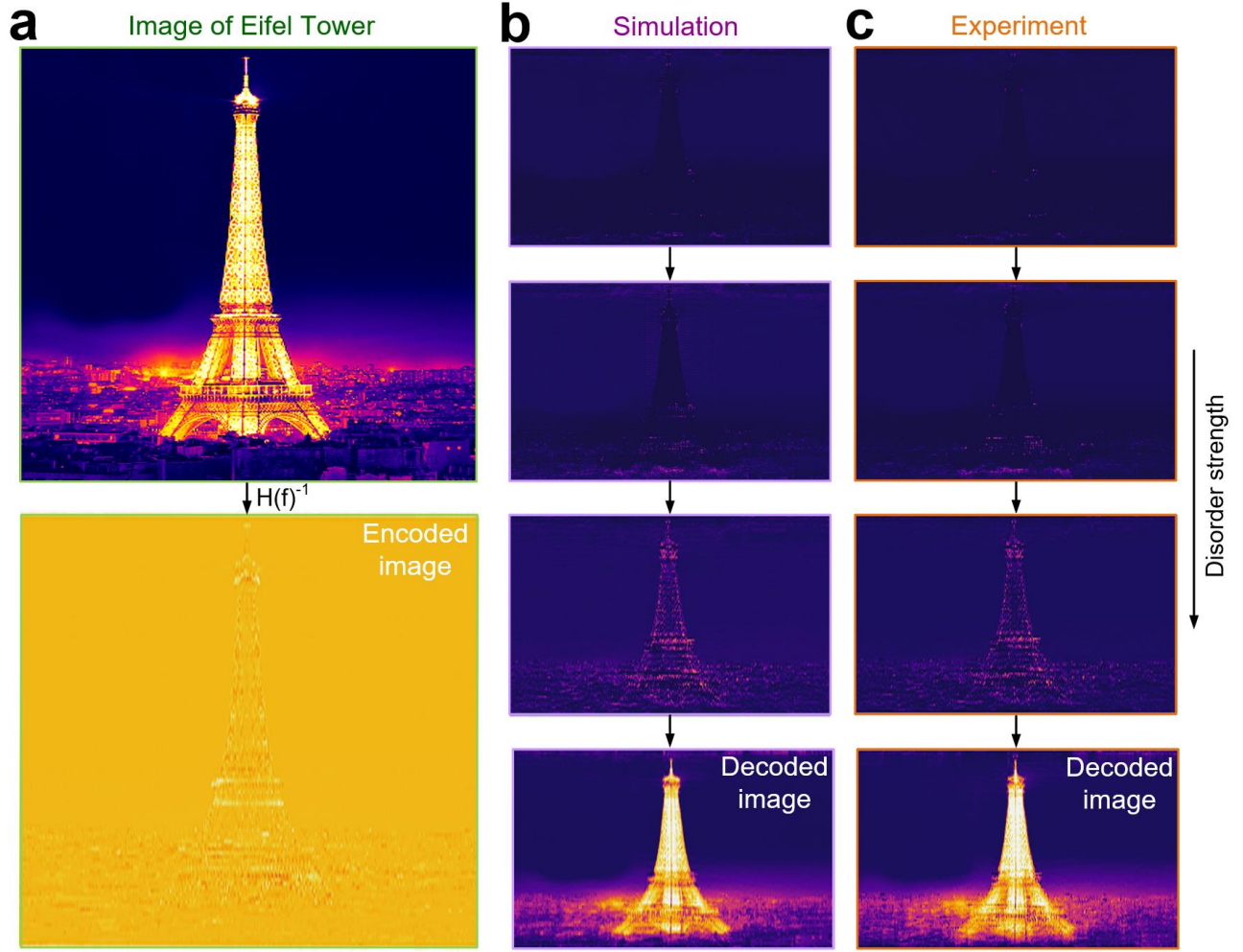
Fig. 5.8: Disorder-induced topological image processing, a, (Top) Image of the Eifel tower, considered for processing, (Bottom) The original image is encrypted with the inverse of the target transfer function $H(f)$. The encrypted image is then fed into the input of the proposed topological random computer. b, Corresponding output images as the level of disorder is gradually increased. c, Corresponding experimental results. The results, in agreement with numerical simulations, demonstrate the intriguing possibility of decoding the encrypted image by providing our proposed computing system with more and more disorder [213].

disorder by standard standing wave pattern analysis. Then, I took the average of 10 different independent measurements, each of which corresponds to a distinct disorder configuration. The corresponding disorder-averaged transmission spectrum, as a function of disorder, is shown in Fig. 5.6a, being in perfect agreement with our prior numerical findings.
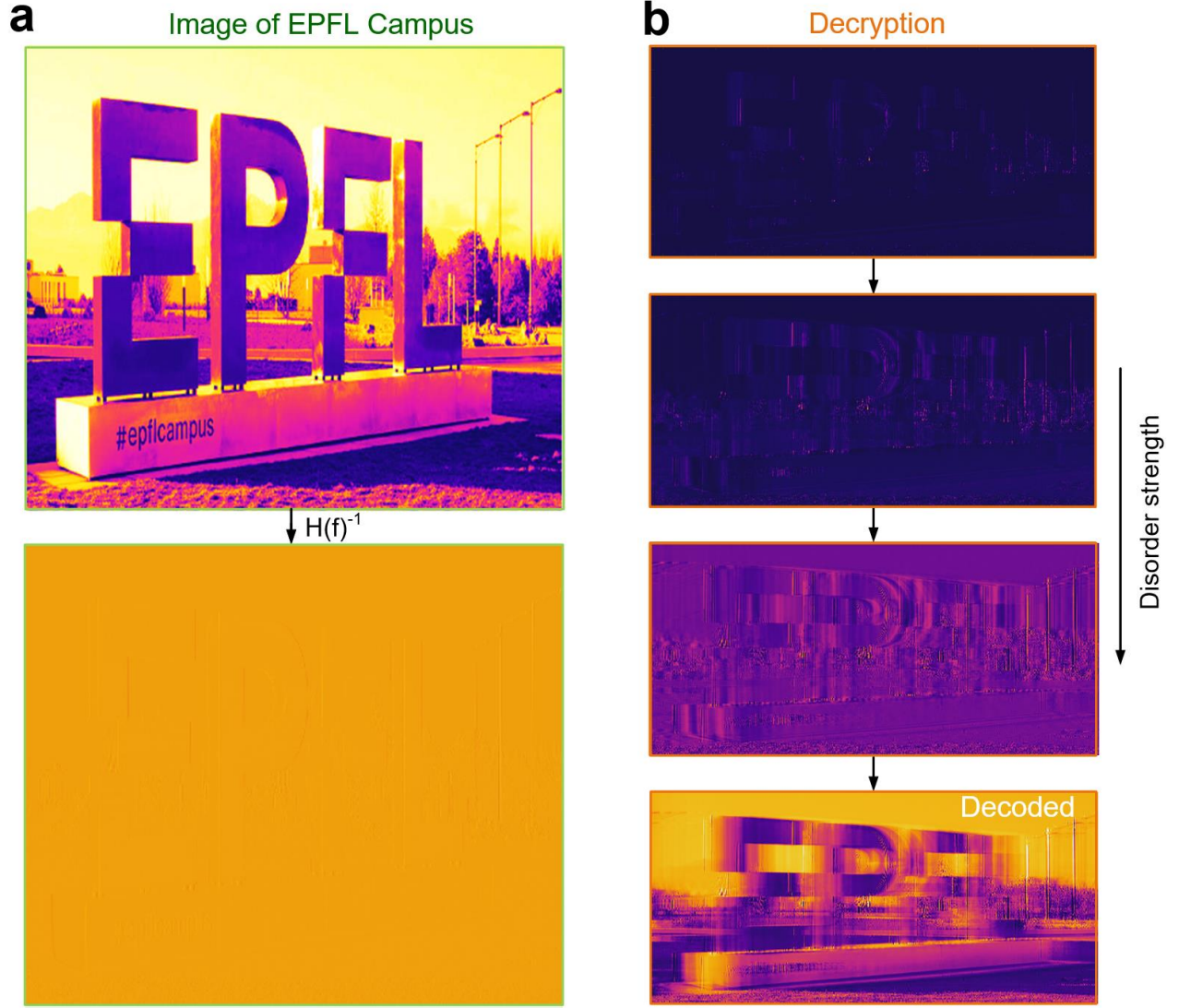
Fig. 5.9. Performing image processing with our proposed computing machine, The figure repeats the analysis of Fig. 5.8, for a different test image taken on our campus. The results are obtained based on the measured (experimental) transmission spectrum [213].

The possibility to leverage the Lorentzian line shape of the edge mode of the TAI phase for carrying out disorder-induced filtering or equation solving is demonstrated in Fig. 5.6b-e. For the disorder-free sample, the transmission spectrum (Fig. 5.6b) has very low level around f_0, leading to an output signal (Fig. 5.6c) that is drastically different from the solution of the desired differential equation (the blue curve). However, in the regime of TAI phase, the transmission

spectrum follows the desired transfer function $H(f)$ (Fig. 5.6d) and, consequently, the corresponding transmitted signal, shown Fig. 5.3e, is nothing but the solution of the targeted ODE (blue curve). In Fig. 5.7, I have repeated the analysis for another type of excitation signal, having an arbitrary peculiar shape.

5.3   Topological random image processing

The proposed computing scheme promises to enable more-complex functionalities. In Fig. 5.8, I demonstrate its relevance for image processing. Consider the image of the Eiffel tower, shown in Fig. 5.8a (top). Suppose that the pixels of this image are processed by the inverse of the target transfer function $H(f)$, therefore encrypting the image. I excite the proposed acoustic computing system with a signal corresponding to the encrypted image. Since, in the regime of TAI, the transfer function of the computing system is approximately equal to $H(f)$, the system is expected to decrypt the encoded image. This is demonstrated in the insets of Fig. 5.8b, illustrating how the encrypted image is gradually decoded by the proposed computing system, when more and more disorder is introduced. The associated experimental results, shown in Fig. 5.8c, are in full agreement with the simulations. Note that decoding the image is not a trivial task as one needs not only to tune the disorder strength to the right level, but also to have some information about the required disorder statistics, in particular the difference in the standard deviations of the couplings. In Fig. 5.9, I have tested the functionality of the proposed system for another image taken in our campus.

5.4   Photonic topological random signal processors

Although demonstrated here in the context of acoustics, we can expect the emergence of such topological random computers to be generic. Here, I propose the photonic version of such kind of computers. Consider a regular photonic crystal consisting of a conventional metallic

waveguide, inside which a one dimensional array of silicon rods is implemented. Similar to the acoustic case, I introduce some disorder into the successive distance between the inclusions of the photonic crystal. In the regime where the strength of disorder is weak, the transmission spectrum is gapped around the resonance frequency of the resonators, due to the topologically trivial nature of the system in the clean limit. Adding disorder to the system, however, closes the trivial gap and re-opens it as topological, as broadly discussed previously. This gives rise to a zero-energy edge state, manifesting itself as a Lorentzian resonance peak in the averaged transmission spectrum, which is employed to solve a first-order differential equation in time domain (or perform first-order band-pass filtering in frequency domain). As opposed to conventional EM-based signal processors for which the presence of disorder is drastically detrimental, the proposed computing system owes its proper performance to the existence of disorder. To demonstrate these predictions, I consider a Gaussian-modulated sinusoidal signal (with frequency of f_0 and the variance of $\sigma = 0.1f_0$) as the input signal. I then study what the system returns both in the clean and TAI regimes. Figs. 5.10a and b show the output signals corresponding to the clean and disordered systems, respectively. When the system is free of disorder (panels a), the output signal has a very low level, being far from the solution of the targeted ODE (blue dashed line). On the other hand, the disordered system (panel b) has perfectly resolved the solution of the ODE. These observations demonstrate the much-sought disorder-induced character of the proposed photonic equation solver.
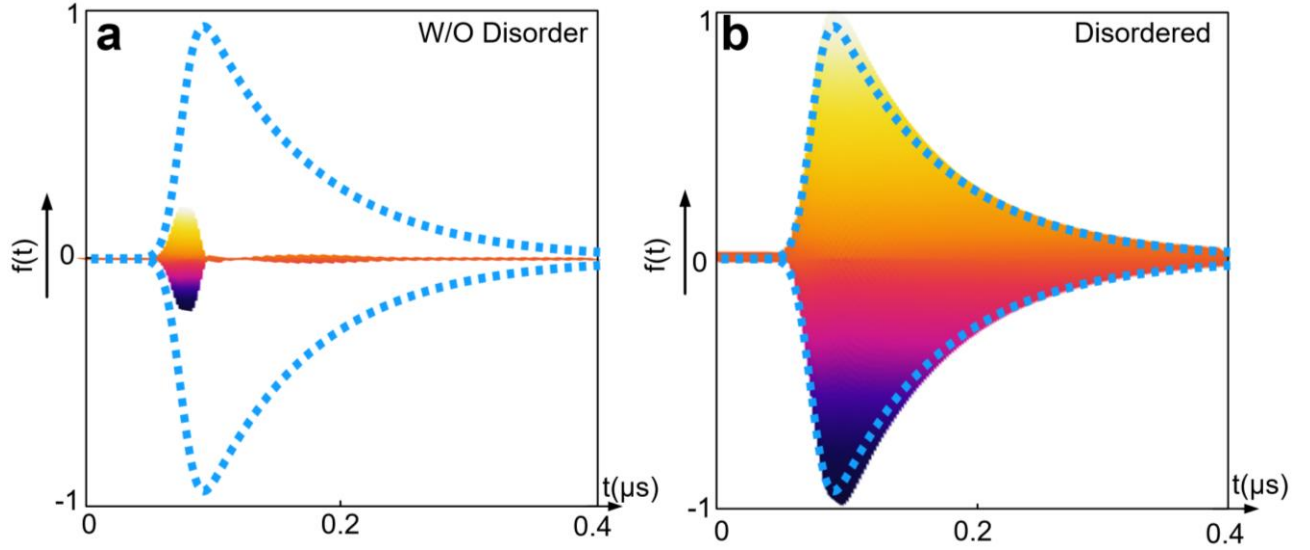
Fig. 5.10. Demonstration of topological random computing in electromagnetics, I consider a photonic crystal quite similar to the phononic crystal shown in Fig. 62, consisting of silicon rods arranged inside a conventional metallic waveguide. In the clean limit, the system is designed to be topologically trivial. Yet, introducing disorder to it enables topological phase transition, leading to topological Anderson insulator phase. a, Disorder-averaged transmitted signal, when the system is excited with a Gaussian-type time modulated signal and only weak amount of disorder is present. b, Same as a except that the system is strongly disordered so that it enters TAI regime [213].

5.5   Conclusions

In this chapter, I demonstrate the unique possibility of turning the harmful effects of disorder into an advantage, based on the disorder-induced character of the so-called topological Anderson insulators. I constructed an explicit example of a novel class of analog computers in which disorder acts as a pseudo-engine, driving the system to carry out a desired, well-defined, computational task. I demonstrated that it is possible to achieve advanced signal processing tasks, such as equation solving and image processing, by adding disorder to pure systems. The disorder triggered the system to go to a topological phase transition, turning a topologically trivial system into a non-trivial one supporting gap-closing boundary states on its edges. Upon excitation, these self-induced topological boundary states yielded a mid-gap resonance in the

(averaged transmission spectrum of the chain), which was leveraged for analog computing purposes. These findings open a new horizon for leveraging disorder as an intrinsic degree of freedom to achieve desired analog functionalities.

Chapter 6   Conclusions and future directions

6.1   Achieved results

In this project, I have investigated the intriguing possibility of robust signal manipulation and analog signal processing based on topological insulators. The computing systems and signal processors proposed in this thesis are very fast due to their wave nature. In particular, they process signals as fast as the speed of wave. This feature is highly appealing in modern engineering, where speed is one of the most important factors which should be taken into account. More importantly, I demonstrated that the much-sought topological protection of topological insulators can be leveraged to ensure a strong robustness and stability.

I have identified three different types of computing systems. The first type, demonstrated in Chapter 3 was based on the Lorentzian resonance associated with the edge mode of a one-dimensional topological insulator. I demonstrated the relevance of such kind of a resonance for solving a first order differential equation. By providing numerical simulations and experimental measurements, I demonstrated that, in stark contrast to conventional analog signal processors proposed thus far, the functionality of a topological analog computing system is not significantly affected by the presence of disorder.

In chapter 4, I discussed the possibility of performing more complex signal processing tasks based on a novel class of topological resonances possessing a Fano line shape. I achieved this based on the coupling between two distinct Lorentzian resonances, each of which was topological in nature. I demonstrated, both in simulation and experiment, how topology can

protect the much-sought line-shape of Fano resonances. This is in stark contrast to trivial Fano resonances, which are very sensitive to structural and geometrical disorder.

Finally, in chapter 5, I demonstrated a novel class of topological computing systems that not only do not suffer from disorder, but, surprisingly, take advantage of it to perform a desired functionality. In particular, inspired by the recently proposed concept of topological Anderson insulators, I showed that it is possible to achieve topological phase transition solely by adding disorder to pure systems, turning them from a trivial insulator into a topological one with gap-closing resonance modes on their boundaries. I then demonstrated, both in theory and experiment, how such resonances can be used for performing disorder-induced signal processing.

6.2   Future directions

On basis of this work, several future directions can be pursued. All of the computing systems demonstrated in this work were based on one-dimensional topological insulators. Generalizing the concept of topological analog signal processing to two, three and even higher dimensions is therefore a straightforward, but very important, issue which has to be addressed in future studies. One may for instance think of implementing a topological computing system by means of a quantum Hall insulator, owing its topological properties to a broken time reversal symmetry. Such systems provide immunity against a wider range of imperfections and defect types, since their topological orders are protected by time reversal symmetry, which cannot be broken unless by introducing magnetization or spin-orbit coupling mechanisms.

Another important thing to investigate is studying topological analog computers in photonics. Such kinds of computers have two important advantageous features, compared to the computing systems demonstrated in this thesis, which were mainly based on acoustic signals. The first advantage is that their speeds are much higher, since light waves travel much faster than

sound. The second advantage is that they are much more compact than the configurations proposed in this thesis. This is because the wavelength of operation is very smaller in optics. Another interesting route to follow is to combine wave-based computing techniques with the ones of artificial intelligence and machine learning, enabling realization of a novel generation of "auto-computer", which automatically perform desired functionalities. All of the computing systems demonstrated in this are required to be properly designed for a specific functionality. However, combing the emerging concept of machine learning with analog signal processing could potentially lead to intelligent analog computers, which perform a desired functionality without any supervision. Altogether, a very bright future for wave-based analog signal processing can be envisioned.

References

1. D. R. Solli, and B. Jalali. Analog optical computing. *Nature Photonics* **9**, 704 (2015).
2. J. S. Small, General-purpose electronic analog computing: 1945-1965. *IEEE Annals of the History of Computing* **15**, 8-18 (1993).
3. A. Silva, et al. Performing mathematical operations with metamaterials. *Science.* **343,** 160–163 (2014).
4. N. Engheta, and R. W. Ziolkowski, eds. *Metamaterials: physics and engineering explorations*. John Wiley & Sons, 2006.
5. A. Youssefi, et al. Analog computing by Brewster effect. *Optics letters* **41**, 3467-3470 (2016).
6. F. Zangeneh-Nejad, and A. Khavasi. Spatial integration by a dielectric slab and its planar graphene-based counterpart. *Optics letters* **42**, 1954-1957 (2017).
7. F. Zangeneh-Nejad, and R. Fleury. Performing mathematical operations using high-index acoustic metamaterials. *New Journal of Physics* **20**, 073001.
8. A. Pors, M. G. Nielsen, and S. I. Bozhevolnyi. Analog computing using reflective plasmonic metasurfaces. *Nano letters* **15**, 791-797 (2014).
9. A. Chizari, et al. Analog optical computing based on a dielectric meta-reflect array. *Optics letters* **41**, 3451-3454 (2016)
10. A. Geim, Graphene: status and prospects. *science* **324**, 1530-1534 (2009).
11. S. AbdollahRamezani, et al. Analog computing using graphene-based metalines. *Optics letters* **40**,5239-5242 (2015).
12. S. Zuo, et al. Mathematical operations for acoustic signals based on layered labyrinthine metasurfaces. *Applied Physics Letters* **110**, 011904 (2017).
13. T. Yang, et al. All-optical differential equation solver with constant-coefficient tunable based on a single microring resonator. *Scientific reports* **4**, 5581 (2014).
14. N. Mohammadi Estakhri, B. Edwards, and N. Engheta. Inverse-designed metastructures that solve equations. *Science* **363**, 1333-1338 (2019).
15. B. A. Bernevig, and T. L. Hughes. *Topological insulators and topological superconductors*. Princeton university press, 2013.
16. L. D. Landau, On the theory of phase transitions. Ukr. J. Phys. **11**, 19-32 (1937).
17. F. D. M. Haldane, Model for a quantum Hall effect without Landau levels: Condensed-matter realization of the parity anomaly. *Physical Review Letters* **61**, 2015 (1988).
18. X. Wen. Topological orders in rigid states. *International Journal of Modern Physics B* **4**, 239-271 (1990).
19. M. Hasan, and L. K. Charles. Colloquium: topological insulators. *Reviews of modern physics* **82**, 3045 (2010).
20. X. Qi, and S. Zhang. Topological insulators and superconductors. *Reviews of Modern Physics* **83**, 1057 (2011).
21. Y. Hatsugai, Chern number and edge states in the integer quantum Hall effect. *Physical review letters* **71**, 3697 (1993).
22. D. Pesin, and A. H. MacDonald. Spintronics and pseudospintronics in graphene and topological insulators. *Nature materials* **11**, 409 (2012).

23. L. Šmejkal, et al. Topological antiferromagnetic spintronics. *Nature Physics* **14**, 242 (2018).

24. M. Berry. Quantal phase factors accompanying adiabatic changes. *Proceedings of the Royal Society of London. A. Mathematical and Physical Sciences* **392**, 45-57 (1984).

25. F. D. M. Haldane, and S. Raghu. Possible realization of directional optical waveguides in photonic crystals with broken time-reversal symmetry. *Physical review letters* **100**, 013904 (2008).

26. L. Lu, J. D. Joannopoulos, and M. Soljačić. Topological photonics. *Nature photonics* **8**, 821 (2014).

27. X. Zhang, et al. Topological sound. *Communications Physics* **1**, 1-13 (2018).

28. S, D. Huber, Topological mechanics. *Nature Physics* **12**, 621 (2016).

29. M. Fruchart, and D. Carpentier. An introduction to topological insulators. *Comptes Rendus Physique* **14**, 779-815 (2013).

30. J. K. Asbóth, L. Oroszlány, and A. Pályi. A short course on topological insulators. *Lecture notes in physics* **919** (2016).

31. P. A. Kalozoumis, et al. Finite-size effects on topological interface states in one-dimensional scattering systems. *Physical Review A* **98**, 023838 (2018).

32. Y. Hadad, V. Vitelli, and A. Alu. Solitons and propagating domain walls in topological resonator arrays. *ACS Photonics* **4**, 1974-1979 (2017).

33. Q. Cheng, et al. Topologically protected interface mode in plasmonic waveguide arrays. *Laser & Photonics Reviews* **9**, 392-398 (2015).

34. C. W. Ling, et al. Topological edge plasmon modes between diatomic chains of plasmonic nanoparticles. *Optics express* **23**, 2021-2031 (2015).

35. Z. Zhang, et al. Experimental Realization of Multiple Topological Edge States in a 1D Photonic Lattice. *Laser & Photonics Reviews* **13**, 1800202 (2019).

36. P. St-Jean, et al. Lasing in topological edge states of a one-dimensional lattice. *Nature Photonics* **11**, 651 (2017).

37. M. Xiao, et al. Geometric phase and band inversion in periodic acoustic systems. *Nature Physics* **11**, 240 (2015).

38. M. Parto, et al. Edge-mode lasing in 1D topological active arrays. *Physical review letters* **120**, 113901 (2018).

39. D. Woolard, and J. L. Jensen. *Spectral Sensing Research for Water Monitoring Applications and Frontier Science and Technology for Chemical, Biological and Radiological Defense*. **48**. World Scientific, 2008.

40. Y. Zhang, et al. Experimental observation of the quantum Hall effect and Berry's phase in graphene. *Nature* **438**, 201 (2005).

41. Z. Wang, et al. Observation of unidirectional backscattering-immune topological electromagnetic states. *Nature* **461**, 772 (2009).

42. R. Fleury, et al. Sound isolation and giant linear nonreciprocity in a compact acoustic circulator." *Science* **343**, 516-519 (2014).

43. A. B. Khanikaev, et al. Topologically robust sound propagation in an angular-momentum-biased graphene-like resonator lattice. *Nature communications* **6**, 8260 (2015).

44. Z. Yang, et al. Topological acoustics. *Physical review letters* **114**, 114301 (2015).

45. C. L. Kane., and E. J. Mele. Quantum spin Hall effect in graphene. *Physical review letters* **95**, 226801(2005).

46. B. A. Bernevig, T. L. Hughes, and S. Zhang. Quantum spin Hall effect and topological phase transition in HgTe quantum wells. *Science* **314**, 1757-1761 (2006).

47. X. Zhu, et al. Z2 topological edge state in honeycomb lattice of coupled resonant optical waveguides with a flat band. *Optics express* **26**, 24307-24317 (2018).

48. O. Gröning, et al. Engineering of robust topological quantum phases in graphene nanoribbons. *Nature* **560**, 209 (2018).

49. V. K. Kozin, et al. Topological metamaterials based on polariton rings. *Physical Review B* **98**, 125115 (2018).

50. Y. Bliokh, D. Smirnova, and F. Nori. Quantum spin Hall effect of light. *Science* **348**, 1448-1451 (2015).

51. C. He, et al. Acoustic topological insulator and robust one-way sound transport. *Nature Physics* **12**, 1124 (2016).

52. H. Chen, et al. Elastic quantum spin Hall effect in kagome lattices. *Physical Review B* **98,** 094302 (2018).

53. F. Ju, Y. Cheng, and X. Liu. Acoustic spin Hall-like effect in hyperbolic metamaterials controlled by the helical wave. *Scientific reports* **8,** 11113 (2018).

54. B. Xia, et al. Topological phononic insulator with robust pseudospin-dependent transport. *Physical Review B* **96**, 094106 (2017).

55. S. Wang, M. Guancong, and C.T. Chan. Topological transport of sound mediated by spin-redirection geometric phase. *Science advances* **4**, eaaq1475 (2018).

56. A. Slobozhanyuk, et al. Three-dimensional all-dielectric photonic topological insulator. *Nature Photonics* **11**, 130 (2017).

57. S. H. Mousavi, A. B. Khanikaev, and Z. Wang. Topologically protected elastic waves in phononic metamaterials. *Nature communications* **6**, 8682 (2015).

58. J. Mei, Z. Chen, and Y. Wu. Pseudo-time-reversal symmetry and topological edge states in two-dimensional acoustic crystals. *Scientific reports* **6**, 32752 (2016).

59. Y. Deng, et al. Observation of zone folding induced acoustic topological insulators and the role of spin-mixing defects. *Physical Review B* **96,** 184305 (2017).

60. C. He, et al. Topological phononic states of underwater sound based on coupled ring resonators. *Applied Physics Letters* **108,** 031904 (2016).

61. Y. Zhou, P. R. Bandaru, and D. F. Sievenpiper. Quantum-spin-Hall topological insulator in a spring-mass system. *New Journal of Physics* **20**, 123011 (2018).

62. A. B. Khanikaev, et al. "Photonic topological insulators." *Nature materials* 12.3 (2013): 233.

63. M. Miniaci, et al. Experimental observation of topologically protected helical edge modes in patterned elastic plates. *Physical Review X* **8**, 031074 (2018).

64. L. Wu, and X. Hu. Scheme for achieving a topological photonic crystal by using dielectric material. *Physical review letters* **114**, 223901 (2015).

65. S. Yves, et al. Crystalline metamaterials for topological properties at subwavelength scales. *Nature communications* **8**, 16023 (2017).

66. L. Wang, et al. The existence of topological edge states in honeycomb plasmonic lattices. *New Journal of Physics* **18**, 103029 (2016).

67. S. Barik, et al. Two-dimensionally confined topological edge states in photonic crystals. *New Journal of Physics* **18**, 113013 (2016).

68. Y. Yang, et al. Visualization of a unidirectional electromagnetic waveguide using topological photonic crystals made of dielectric materials. *Physical review letters* **120**, 217401 (2018).

69. M. Shalaev, et al. Robust topologically protected transport in photonic crystals at telecommunication wavelengths. *Nature nanotechnology* **14**, 31 (2019).

70. M. Honari-Latifpour, and L. Yousefi. Topological plasmonic edge states in a planar array of metallic nanoparticles. *Nanophotonics* **8**, 799-806 (2019).

71. S. Wu, Y. Wu, and J. Mei. Topological helical edge states in water waves over a topographical bottom. *New Journal of Physics* **20**, 023051 (2018).

72. R. Chaunsali, C. Chen, and J. Yang. Experimental demonstration of topological waveguiding in elastic plates with local resonators. *New Journal of Physics* **20**, 113036 (2018).

73. Y. Chen, X. Liu, and G. Hu. Topological phase transition in mechanical honeycomb lattice. *Journal of the Mechanics and Physics of Solids* **122**, 54-68 (2019).

74. S. Yu, et al. Elastic pseudospin transport for integratable topological phononic circuits. *Nature communications* **9**, 3072 (2018).

75. Z. Zhang, et al. Topological creation of acoustic pseudospin multipoles in a flow-free symmetry-broken metamaterial lattice. *Physical review letters* **118**, 084303 (2017).

76. Z. Zhang, et al. Experimental verification of acoustic pseudospin multipoles in a symmetry-broken snowflakelike topological insulator. *Physical Review B* **96**, 241306 (2017).

77. Z. Geng, et al. Topologically protected edge transport of sound in coupled cavities of a modified honeycomb lattice. *Journal of Physics: Condensed Matter* **30**, 345401 (2018).

78. S. Yves, et al. Topological acoustic polaritons: robust sound manipulation at the subwavelength scale. *New Journal of Physics* **19**, 075003 (2017).

79. B. Bradlyn, et al. Topological quantum chemistry. *Nature* **547**, 298 (2017).

80. B. Orazbayev, and R. Fleury. Quantitative robustness analysis of topological edge modes in C6 and valley-Hall metamaterial waveguides. *Nanophotonics* **8**, 1433-1441 (2019).

81. X. He, et al. A silicon-on-insulator slab for topological valley transport. *Nature communications* **10**, 872 (2019).

82. Z. Zhu, et al. Negative Refraction and Partition in Acoustic Valley Materials of a Square Lattice. *Physical Review Applied* **12**, 024007 (2019).

83. L. Ye, et al. Observation of valley-selective microwave transport in photonic crystals. *Applied Physics Letters* **111**, 251107 (2017).

84. X. Han, et al. Experimental Demonstration of Acoustic Valley Hall Topological Insulators with the Robust Selection of C 3v-Symmetric Scatterers. *Physical Review Applied* **12**, 014046 (2019).

85. X. Wu, et al. Direct observation of valley-polarized topological edge states in designer surface plasmon crystals. *Nature communications* **8**, 1304 (2017).

86. R. Pal, and M. Ruzzene. Edge waves in plates with resonators: an elastic analogue of the quantum valley Hall effect. *New Journal of Physics* **19**, 025001 (2017).

87. T. Liu, and F. Semperlotti. Experimental Evidence of Robust Acoustic Valley Hall Edge States in a Nonresonant Topological Elastic Waveguide. *Physical Review Applied* **11**, 014040 (2019).

88. T. Liu, and F. Semperlotti. Tunable acoustic Valley–Hall edge states in reconfigurable phononic elastic waveguides. *Physical Review Applied* **9**, 014001 (2018).

89. J. Lu, et al. Valley vortex states in sonic crystals. *Physical review letters* **116**, 093901 (2016).

90. J. Vila, R. Pal, and M. Ruzzene. Observation of topological valley modes in an elastic hexagonal lattice. *Physical Review B* **96**, 134307 (2017).

91. J. Noh, et al. Observation of photonic topological valley Hall edge states. *Physical review letters* **120**, 063902 (2018).

92. J. Lu, et al. Observation of topological valley transport of sound in sonic crystals. *Nature Physics* **13**, 369 (2017).

93. N. Laforge, et al. Observation of topological gravity-capillary waves in a water wave crystal. *New Journal of Physics* **21**, 083031 (2019).

94. J. Asbóth, B. Tarasinski, and P. Delplace. Chiral symmetry and bulk-boundary correspondence in periodically driven one-dimensional systems. *Physical Review B* **90**, 125143 (2014).

95. V. Dal Lago, M. Atala, and L. Torres. Floquet topological transitions in a driven one-dimensional topological insulator. *Physical Review A* **92**, 023624 (2015).

96. M. Fruchart. Complex classes of periodically driven topological lattice systems. *Physical Review B* **93**, 115429 (2016).

97. N. H. Lindner, G. Refael, and V. Galitski. Floquet topological insulator in semiconductor quantum wells. *Nature Physics* **7**, 490 (2011).

98. L. Maczewsky, et al. Observation of photonic anomalous Floquet topological insulators. *Nature communications* **8**, 13756 (2017).

99. Q. Cheng, et al. Observation of anomalous π modes in photonic Floquet engineering. *Physical review letters* **122**, 173901 (2019).

100. X. Liu, Q. Guo, and J. Yang. Miniaturization of Floquet topological insulators for airborne acoustics by thermal control. *Applied Physics Letters* **114**, 054102 (2019).

101. C. M. Dai, W. Wang, and X. X. Yi. Photonic Floquet topological insulators with fluctuations and disorders. *Physical Review A* **99**, 033844 (2019).

102. Y. Peng, et al. Low-loss and broadband anomalous Floquet topological insulator for airborne sound. *Applied Physics Letters* **110**, 173505 (2017).

103. W. Zhang, X. Chen, and F. Ye. Plasmonic topological insulators for topological nanophotonics. *Optics letters* **42**, 4063-4066 (2017).

104. M. C. Rechtsman, et al. Photonic Floquet topological insulators. *Nature* **496**, 196 (2013).

105. R. Fleury, A. B. Khanikaev, and A. Alu. Floquet topological insulators for sound. *Nature communications* **7**, 11744 (2016).

106. M. Pasek, and Y. D. Chong. Network models of photonic Floquet topological insulators. *Physical Review B* **89**, 075113 (2014).

107. P. Delplace, M. Fruchart, and C. Tauber. Phase rotation symmetry and the topology of oriented scattering networks. *Physical Review B* **95,** 205413 (2017).

108. M. S. Rudner, et al. Anomalous edge states and the bulk-edge correspondence for periodically driven two-dimensional systems. *Physical Review X* **3**, 031005 (2013).

109. W. Hu, et al. Measurement of a topological edge invariant in a microwave network. *Physical Review X* **5**, 011012 (2015).

110. Y. Peng, et al. Experimental demonstration of anomalous Floquet topological insulator for sound. *Nature communications* **7**, 13368 (2016).

111. D. Leykam, M. C. Rechtsman, and Y. D. Chong. Anomalous topological phases and unpaired Dirac cones in photonic Floquet topological insulators. *Physical review letters* **117**, 013902 (2016).

112. M. Neupane, et al. Observation of topological nodal fermion semimetal phase in ZrSiS. *Physical Review B* **93**, 201104 (2016).

113. L. Xia, et al. Observation of Hourglass Nodal Lines in Photonics. *Physical Review Letters* **122**, 103903 (2019).

114. W. Deng, et al. Nodal rings and drumhead surface states in phononic crystals." *Nature communications* **10,** 1769 (2019).

115. W. Gao, et al. Experimental observation of photonic nodal line degeneracies in metacrystals. *Nature communications* **9**, 950 (2018).

116. H. Po, Y. Bahri, and A. Vishwanath. Phonon analog of topological nodal semimetals. *Physical Review B* **93**, 205158 (2016).

117. L. Lu, et al. Experimental observation of Weyl points. *Science* **349**, 622-624 (2015).

118. S. Xu, et al. Discovery of a Weyl fermion semimetal and topological Fermi arcs. *Science* **349**, 613-617 (2015).

119. W. Ye, et al. Photonic Hall effect and helical Zitterbewegung in a synthetic Weyl system. *Light: Science & Applications* **8**, 49 (2019).

120. A. A. Zyuzin, and V. A. Zyuzin. Chiral electromagnetic waves in Weyl semimetals. *Physical Review B* **92**, 115310 (2015).

121. E. Goi, et al. Observation of Type I Photonic Weyl Points in Optical Frequencies. *Laser & Photonics Reviews* **12**, 1700271 (2018).

122. Z. Yang, and B. Zhang. Acoustic type-II Weyl nodes from stacking dimerized chains. *Physical review letters* **117**, 224301 (2016).

123. B. Xie, et al. Experimental Realization of Type-II Weyl Points and Fermi Arcs in Phononic Crystal. *Physical review letters* **122**, 104302 (2019).

124. X. Shi, et al. Elastic Weyl Points and Surface Arc States in Three-Dimensional Structures. *Physical Review Applied* **12**, 024058 (2019).

125. W. Chen, M. Xiao, and C. T. Chan. Photonic crystals possessing multiple Weyl points and the experimental observation of robust surface states. *Nature communications* **7**, 13038 (2016).

126. S. M. Young, et al. Dirac semimetal in three dimensions. *Physical review letters* **108**, 140405 (2012).

127. Q. Guo, et al. Three dimensional photonic Dirac points in metamaterials. *Physical review letters* **119**, 213901 (2017).

128. J. Lin, et al. Line nodes, Dirac points, and Lifshitz transition in two-dimensional nonsymmorphic photonic crystals. *Physical Review B* **96**, 075438 (2017).

129. S. Borisenko, et al. Experimental realization of a three-dimensional Dirac semimetal. *Physical review letters* **113**, 027603 (2014).

130. S. M. Young, and C. L. Kane. Dirac semimetals in two dimensions. *Physical review letters* **115**, 126803 (2015).

131. L. Lu, et al. Weyl points and line nodes in gyroid photonic crystals. *Nature photonics* **7**, 294 (2013).

132. M. Xiao, et al. Synthetic gauge flux and Weyl points in acoustic systems. *Nature Physics* **11**, 920 (2015).

133. F. Li, et al. Weyl points and Fermi arcs in a chiral phononic crystal. *Nature Physics* **14**, 30 (2018).

134. Q. Lin, et al. Photonic Weyl point in a two-dimensional resonator lattice with a synthetic frequency dimension. *Nature communications* **7**, 13731 (2016).

135. A. Blanco-Redondo, et al. Topological optical waveguiding in silicon and the transition between topological and trivial defect states. *Physical review letters* **116**, 163901 (2016).

136. L. Shen, et al. Backscattering-immune one-way surface magnetoplasmons at terahertz frequencies. *Optics express* **23**, 950-962 (2015).

137. Y. Shen, et al. Observation of low-loss broadband supermode propagation in coupled acoustic waveguide complex. *Scientific reports* **7**, 45603 (2017).

138. Q. Wei, et al. Experimental demonstration of topologically protected efficient sound propagation in an acoustic waveguide network. *Physical Review B* **95**, 094305 (2017).

139. Y. Guo, T. Dekorsy, and M. Hettich. Topological guiding of elastic waves in phononic metamaterials based on 2D pentamode structures. *Scientific reports* **7**, 18043 (2017).

140. V. Peano, et al. Topological phase transitions and chiral inelastic transport induced by the squeezing of light. *Nature communications* **7**, 10779 (2016).

141. S. A. Gangaraj, A. Nemilentsau, and G. W. Hanson. The effects of three-dimensional defects on one-way surface plasmon propagation for photonic topological insulators comprised of continuum media. *Scientific reports* **6**, 30055 (2016).

142. A. Slobozhanyuk, et al. Subwavelength topological edge states in optically resonant dielectric structures. *Physical review letters* **114**, 123901 (2015).

143. P. Wang, L. Lu, and K. Bertoldi. Topological phononic crystals with one-way elastic edge waves. *Physical review letters* **115**, 104302 (2015).

144. Y. V. Kartashov, and D. V. Skryabin. Two-Dimensional Topological Polariton Laser. *Physical review letters* **122**, 083902 (2019).

145. B. Bahari, et al. Nonreciprocal lasing in topological cavities of arbitrary geometries. *Science* **358**, 636-640 (2017).

146. X. Sun, and X. Hu. Topological Ring-Cavity Laser Formed by Honeycomb Photonic Crystals. *arXiv preprint arXiv:1906.02464* (2019).

147. C. Han, et al. Lasing at topological edge states in a photonic crystal L3 nanocavity dimer array. *Light: Science & Applications* **8**, 40 (2019).

148. J. Xu, et al. Ultrasensitive nonlinear absorption response of large-size topological insulator and application in low-threshold bulk pulsed lasers. *Scientific reports* **5**, 14856 (2015).

149. H. Zhao, et al. Topological hybrid silicon microlasers. *Nature communications* **9**, 981 (2018).

150. L. Pilozzi, and C. Conti. Topological cascade laser for frequency comb generation in PT-symmetric structures. *Optics letters* **42**, 5174-5177 (2017).

151. G. Harari, et al. Topological insulator laser: Theory. *Science* **359**, eaar4003 (2018).

152. M. Hafezi, et al. Robust optical delay lines with topological protection. *Nature Physics* **7**, 907 (2011).

153. M. Hafezi, et al. Imaging topological edge states in silicon photonics. *Nature Photonics* **7,** 1001 (2013).

154. M. A. Bandres, et al. Topological insulator laser: Experiments. *Science* **359**, eaar4005 (2018)

155. M. Ezawa. Topological switch between second-order topological insulators and topological crystalline insulators. *Physical review letters* **121**, 116801 (2018).
156. F. Hassler, A. R. Akhmerov, and C. W. J. Beenakker. Flat-lens focusing of electrons on the surface of a topological insulator. *Physical Review B* **82**, 125423 (2010).
157. H. He, et al. Topological negative refraction of surface acoustic waves in a Weyl phononic crystal. *Nature* **560**, 61 (2018).
158. T. Fujita, M. Bin Abdul Jalil, and S. Ghee Tan. Topological insulator cell for memory and magnetic sensor applications. *Applied Physics Express* **4**, 094201 (2011).
159. L. Ye, et al. Observation of acoustic valley vortex states and valley-chirality locked beam splitting. *Physical Review B* **95**, 174106 (2017).
160. H. Liu, et al. Femtosecond pulse generation from a topological insulator mode-locked fiber laser. *Optics express* **22**, 6868-6873 (2014).
161. Z. Zhang, et al. Topological acoustic delay line. *Physical Review Applied* **9**, 034032 (2018).
162. Y. Wang, et al. Topologically enhanced harmonic generation in a nonlinear transmission line metamaterial. *Nature communications* **10**, 1102 (2019).
163. R. Ilan, F. Juan, and J. E. Moore. Spin-based mach-zehnder interferometry in topological insulator p− n junctions. *Physical review letters* **115**, 096802 (2015).
164. D. A. Bykov, et al. First-order optical spatial differentiator based on a guided-mode resonant grating. *Optics Express* **26,** 10997 (2018).
165. W. Wu, W. Jiang, J. Yang, S. Gong, and Y. Ma, Multilayered analog optical differentiating device: performance analysis on structural parameters. *Optics Letters* **42**, 5270-5273 (2017).
166. H. Kwon, D. Sounas, A. Cordaro, A. Polman, and A. Alù, Nonlocal Metasurfaces for Optical Signal Processing. *Physical Review Letters*. **121**, 173004 (2018).
167. S. Zuo, Q. Wei, Y. Tian, Y. Cheng, and X. Liu, Acoustic analog computing system based on labyrinthine metasurfaces. *Scientific reports* **8**, 1-8 (2018).
168. W. Zhang, *et al.* Implementing Quantum Search Algorithm with Metamaterials. *Adv. Mater.* **30,** (2018).
169. Y. Fang, Y. Lou, and Z. Ruan, On-grating graphene surface plasmons enabling spatial differentiation in the terahertz region. *Opics Letters*, **42**, 3840 (2017).
170. Y. Hwang, T. J. Davis, J. Lin, and X. C. Yuan, Plasmonic circuit for second-order spatial differentiation at the subwavelength scale. *Opics Express* **26,** 7368 (2018).
171. Z. Dong, J. Si, X. Yu, and X. Deng, Optical spatial differentiator based on subwavelength high-contrast gratings. *Applied Physics Letters* **112**, 181102 (2018).
172. F. Zangeneh-Nejad, R. Fleury, Topological analog signal processing, *Nat. Commun.* **10,** 2058 (2019)
173. T. Zhu, *et al.* Plasmonic computing of spatial differentiation. *Nat. Commun.* **8,** 1-6 (2017).
174. F. Zangeneh-Nejad, and R. Fleury. Acoustic rat-race coupler and its applications in non-reciprocal systems. *The Journal of the Acoustical Society of America* **146**, 843-849 (2019).
175. C. Guo, M. Xiao, M. Minkov, Y. Shi, and S. Fan, Photonic crystal slab Laplace operator for image differentiation. *Optica* **5,** 251 (2018).
176. F. Zangeneh-Nejad, and Fleury, R. Performing mathematical operations using high-index acoustic metamaterials. *New journal of physics.* **20,** 073001 (2018).

177. M. Ferrera, *et al.* On-chip CMOS-compatible all-optical integrator. *Nature Communications.* **1,** 1-5 (2010).

178. D. Brunner, M. C. Soriano, C. R. Mirasso, and I. Fischer, Parallel photonic information processing at gigabyte per second data rates using transient states. *Nature Communications.* **4,** 1-7 (2013).

179. S. M. Kuo, B. H. Lee, and W. Tian, *Real-Time Digital Signal Processing: Fundamentals, Implementations and Applications. New York* (2013).

180. D. J. Griffiths, and C. A. Steinke, Waves in locally periodic media. *American Journal of Physics* **69**, 137-154 (2001).

181. B. G. Wybourne, Classical groups for physicists (1974).

182. K. Esaki, M. Sato, K. Hasebe, and M. Kohmoto, Edge states and topological phases in non-Hermitian systems. Physical Review B **84**, 205128 (2011).

183. U. Fano. Effects of configuration interaction on intensities and phase shifts." *Physical Review* **124**, 1866 (1961).

184. O. Újsághy, et al. Theory of the Fano resonance in the STM tunneling density of states due to a single Kondo impurity. *Physical review letters* **85**, 2557 (2000).

185. E. A. Laird, et al. Effect of exchange interaction on spin dephasing in a double quantum dot. *Physical review letters* **97**, 056801 (2006).

186. S. Rotter, F. Libisch, J. Burgdörfer, U. Kuhl, and H. J. Stöckmann, Phys. Rev. E - Stat. Physics, Plasmas, Fluids, Relat. Interdiscip. Top. **69**, 4 (2004).

187. A. Bärnthaler, et al. Probing decoherence through Fano resonances. *Physical review letters* **105**, 056801 (2010).

188. E. O. Kamenetskii, G. Vaisman, and R. Shavit. Fano resonances of microwave structures with embedded magneto-dipolar quantum dots. *Journal of Applied Physics* **114**, 173902 (2013).

189. A. Attaran, et al. Circuit model of Fano resonance on tetramers, pentamers, and broken symmetry pentamers. *Plasmonics* **9**, 1303-1313 (2014).

190. B. Lv, R. Li, J. Fu, Q. Wu, K. Zhang, W. Chen, Z. Wang, and R. Ma, Analysis and modeling of Fano resonances using equivalent circuit elements, *Scientific reports.* **6**, 31884 (2016).

191. B. Luk'Yanchuk, N. I. Zheludev, S. A. Maier, N. J. Halas, P. Nordlander, H. Giessen, and C. T. Chong, The Fano resonance in plasmonic nanostructures and metamaterials *Nature materials.* **9**, 707 (2010).

192. P. Fan, Z. Yu, S. Fan, and M. L. Brongersma, *Nature materials.* **13**, 471 (2014).

193. J. B. Lassiter, H. Sobhani, J. A. Fan, J. Kundu, F. Capasso, P. Nordlander, and N. J. Halas, Fano resonances in plasmonic nanoclusters: geometrical and chemical tenability, *Nano Letters.* **10**, 3184 (2010).

194. Y. Wang, L. Liao, T. Hu, S. Luo, L. Wu, J. Wang, Z. Zhang, W. Xie, L. Sun, A. V. Kavokin, X. Shen, and Z. Chen, Exciton-polariton Fano resonance driven by second harmonic generation *Physical Review Letters.* **118**, (2017).

195. J. Butet and O. J. F. Martin, Fano resonances in the nonlinear optical response of coupled plasmonic nanostructures *Optics Express* **22**, 29693 (2014).

196. F. Zangeneh-Nejad and R. Fleury, Topological Fano resonances, *Physical Review Letters*, **122**, 014301 (2019)

197. S. Hein, W. Koch, and L. Nannen, Fano resonances in acoustics. *Journal of fluid mechanics.* **664**, 238-264 (2010).

198. M. F. Limonov, M. V. Rybin, A. N. Poddubny, and Y. S. Kivshar, Fano resonances in photonics *Nature photonics* Photonics **11**, 543 (2017).

199. R. P. Madden, and K. Codilng, Two-Electron Excitation States in Helium. *The Astrophysical Journal*, **141**, 364 (1965).

200. S.L. Chua, Y. Chong, A. D. Stone, M. Soljacic, and J. Bravo-Abad, Low-threshold lasing action in photonic crystal slabs enabled by Fano resonances, *Optics Express* **19**, 1539 (2011).

201. K. Nozaki, A. Shinya, S. Matsuo, T. Sato, E. Kuramochi, and M. Notomi, Ultralow-energy and high-contrast all-optical switch involving Fano resonance based on coupled photonic crystal nanocavities. *Optics. Express* **21**, 11877 (2013).

202. W. Zhao, H. Jiang, B. Liu, Y. Jiang, C. Tang, and J. Li, Fano resonance based optical modulator reaching 85% modulation depth, *Applied Physics Letters*. **107**, (2015).

203. W. Cao, R. Singh, I. A. I. Al-Naib, M. He, A. J. Taylor, and W. Zhang, Low-loss ultra-high-Q dark mode plasmonic Fano metamaterials. *Optics Letters*. **37**, 3366 (2012).

204. N. Papasimakis and N. I. Zheludev, Opt. Photonics News **20**, 22 (2009).

205. K. Q. Le and J. Bai, Enhanced absorption efficiency of ultrathin metamaterial solar absorbers by plasmonic Fano resonance *JOSAB* **32**, 595 (2015).

206. K. P. Heeg, C. Ott, D. Schumacher, H. C. Wille, R. Röhlsberger, T. Pfeifer, and J. Evers, Interferometric phase detection at x-ray energies via Fano resonance control, *Physical Review Letters* **114**, (2015).

207. C. Wu, A. B. Khanikaev, R. Adato, N. Arju, A. A. Yanik, H. Altug, and G. Shvets, Fano-resonant asymmetric metamaterials for ultrasensitive spectroscopy and identification of molecular monolayers, *Nature Materials*. **11**, 69 (2012).

208. Z. Li, S. Zhang, L. Tong, P. Wang, B. Dong, and H. Xu, Ultrasensitive size-selection of plasmonic nanoparticles by Fano interference optical force. *ACS Nano* **8**, 701 (2014).

209. Y. Yu, M. Heuck, H. Hu, W. Xue, C. Peucheret, Y. Chen, L. K. Oxenløwe, K. Yvind, and J. Mørk, Fano resonance by means of the one-dimensional superconductor photonic crystals. *Appl. Phys. Lett*. **105**, (2014).

210. C. Hsu, et al. Bound states in the continuum. *Nature Reviews Materials* **1**, 1-13 (2016).

211. D. S. Wiersma, et al. Localization of light in a disordered medium. *Nature* **390**, 671-673 (1997).

212. J. Li, R. Chu, J. K. Jain, S. Shen. Topological anderson insulator. *Phys. Rev. Lett*. **102**, 136806 (2009).

213. F. Zangeneh-Nejad and R. Fleury, Disorder-Induced Signal Filtering with Topological Metamaterials, *Advanced Materials*, **2001034** (2020)

214. E. J. Meier, F. A. An, A. Dauphin, M. Maffei, P. Massignan, T. L. Hughes, B. Gadway, Observation of the topological Anderson insulator in disordered atomic wires. *Science*, **362**, 929-933 (2018).

215. I. Mondragon-Shem, et al. Topological criticality in the chiral-symmetric AIII class at strong disorder. *Physical Review Letters*. **113**, 046802 (2014).

Farzad Zangeneh-Nejad

Route de la Gare 20, CH 1131, Tolochenaz
fr.zangeneh@gmail.com • +41787295960 • Google-scholar
• Born on 12-05-1994

EDUCATION

Swiss Federal Institute of Technology in Lausanne (EPFL), Lausanne, Switzerland

- Ph.D. in Electrical Engineering (EDPO)   Aug 2017 –present
  - Thesis: Analog signal processing with topological acoustic metamaterials
  - Advisor: Prof. Romain Fleury
  - Focus: Topological insulators, Metamaterials, Acoustics, Optics, Quantum physics.

Sharif University of Technology, Tehran, Iran

- M.Sc. in Wave physics   Aug 2015 – Aug 2017
  - Thesis: Optical computing with plasmonic metamaterials
  - Advisor: Prof. Amin Khavasi
  - Focus: Metamaterials, Graphene, Plasmonics.

- B.Sc. in Electrical Engineering   Aug 2011 – Aug 2015

RESEARCH INTEREST

- Topological insulators
- Wave physics
- Metamaterials
- Acoustics
- Machine learning
- Analog computing
- Photonics

PUBLICATIONS

JOURNALS

[1] **F. Zangeneh-Nejad**, D. Sounas, A. Alu, R. Fleury, "Analog computing with metamaterials," *Nature Reviews Materials*, p. 1-9, 2020

[2] **F. Zangeneh-Nejad**, R. Fleury, "Disorder-induced signal filtering with topological metamaterials," *Advanced Materials*, vol. 32, 2001034, 2020

[3] **F. Zangeneh-Nejad**, R. Fleury, "Zero-index Weyl metamaterials," *Physical Review Letters*, vol. 125, 054301, 2020

[4] **F. Zangeneh-Nejad**, R. Fleury, "Nonlinear second-Order topological insulators," *Physical Review Letters*, vol. 123, 053902, 2019 (*This paper was featured on the cover of the journal (Link) and highlighted by Nature Review Materials (Link)*)

[5] **F. Zangeneh-Nejad**, R. Fleury, "Topological Fano resonances," *Physical Review Letters*, vol. 122, 014301, 2019

[6] **F. Zangeneh-Nejad**, R. Fleury, "Topological analog signal processing," *Nature Communications*, vol. 10, 2058, 2019

[7] **F. Zangeneh-Nejad**, R. Fleury, "Experimental observation of the Z_2 acoustic Weyl semimetallic phase in synthetic dimensions," *Physical Review B*, vol. 102, 064309 , 2020, selected as the editor suggestion

[8] **F. Zangeneh-Nejad**, R. Fleury, "Performing mathematical operations using high-index acoustic metamaterials," *New Journal pf Physics*, vol. 20, 073001, 2018 (*This paper was highlighted by Physics World (Link) and EPFL, School of Engineering Department (Link)*)

[9] **F. Zangeneh-Nejad**, R. Fleury, "Active times for acoustic metamaterials," *Reviews in Physics*, vol. 4, 100031, 2019 (Invited review paper)

[10] **F. Zangeneh-Nejad**, R. Fleury, "Acoustic birefringence via non-Eulerian metamaterials," *Journal of Applied Physics*, vol. 126, 034902, 2018

[11] **F. Zangeneh-Nejad**, N. Kaina, S. Yves, F. Lemoult, G. Lerosey, R. Fleury, "Non-reciprocal manipulation of subwavelength fields in locally-resonant metamaterial crystals," *IEEE Transaction on Antennas and Propagation*, vol. 68, 1726, 2019

[12] **F. Zangeneh-Nejad**, A. Alu, R. Fleury, "Topological wave insulators, a review," *accepted in Comptes Rendus Physiques, click for the pdf, 2020*

[13] **F. Zangeneh-Nejad**, R. Fleury, "Acoustic analogues of high-index optical waveguide devices," *Scientific Reports*, vol. 8, 10401, 2018 (*This paper was among the top 100 Scientific Reports physics papers in 2018 (Link)*)

[14] **F. Zangeneh-Nejad**, R. Fleury, "Acoustic rat-race coupler and its applications in non-reciprocal systems," *The Journal of the Acoustical Society of America*, vol. 146, 843, 2019

[15] **F. Zangeneh-Nejad**, R. Fleury, "Doppler-Based acoustic gyrator," *Applied Sciences*, vol. 8, 1083, 2018

[16] **F. Zangeneh-Nejad**, R. Fleury, "Topological optomechanical induced transparency", *Optics Letters*, vol. 45, 5966-5969, (2020)

[17] A. Yousefi, **F. Zangeneh-Nejad**, S. Abdollahramezani, A. Khavasi, "Analog computing by Brewster effect," *Optics Letters*, vol. 41, 3467, 2016

[18] **F. Zangeneh-Nejad**, A. Khavasi, "Spatial integration by a dielectric slab and its planar graphene-based counterpart," *Optics Letters*, vol. 43, 1954, 2017

[19] **F. Zangeneh-Nejad**, A. Khavasi, "Analog optical computing by half-wavelength slabs," *Optics Communications*, vol. 407, 338, 2018

[20] **F. Zangeneh-Nejad**, R. Safian, "A graphene-based THz ring resonator for label-free sensing," *IEEE Sensor Journal*, vol. 16, 4338, 2016

[21] **F. Zangeneh-Nejad**, R. Safian, "Significant enhancement in the efficiency of photoconductive antennas using a hybrid graphene molybdenum disulphide structure," *Journal of Nanophotonics*, vol. 10, 036005, 2016

[22] **F. Zangeneh-Nejad**, R. Safian, "Hybrid graphene–molybdenum disulphide based ring resonator for label-free sensing," *Optics Communications*, vol. 9, 371, 2016

[23] **F. Zangeneh-Nejad**, R. Safian, "Temperature dependance of elctromagnetic radiation from terahertz photoconductive antennas," *Microwave and Optical Technology Letters*, vol. 57, 2475, 2015

[24] H. Nikaein, R. Safian, **F. Zangeneh-Nejad**, "Stripline Combline Filter Tunes 900 to 1,300 MHz," *Microwave and RF Magazine*, 2016

INVITED TALKS	• Fano resonances in microwaves and photonics	2019
	The 10th international conference on metamaterials, photonic crystals and plasmonics, Lisbon, Portugal (Link)	
	• Topological metamaterials that perform computation	2019
	The 13th international congress on artificial materials for novel wave phenomena, Rome, Italy (Link)	
	• Exotic properties of spoof surface plasmon polaritons in metamaterial crystals	2018
	2nd URSI Atlantic Radio Science Meeting, AT-RASC (Link)	
	• Potential applications of high-index acoustic metamaterials	2018
	176th Meeting of acoustical society of america, Victoria BC, Canada (Link)	

HONOURS AND AWARDS	• Collaborating with Prof. Romain Fleury for getting the SNSF Spark grant (Link)	2020
	• Student paper award at Metamaterials conference, in Roma, Italy (Link)	2019
	• University of Central Florida's ORC doctoral fellowship (Link)	2017
	• Accepted as a talented student for graduate studies without taking university entrance exam	2015

TEACHING EXPERIENCES	• Teaching assistant of Prof. Romain Fleury (Link)	2019
	Name of the course: Transmission lines and waves	
	• Teaching assistant of Prof. Romain Fleury (Link)	2018
	Name of the course: Electromagnetism II	
	• Teaching assistant of Prof. Amin Khavasi (Link)	2017
	Name of the course: Plasmonics and metamaterials	
	• Teaching assistant of Prof. Arash Amini (Link)	2016
	Name of the course: Engineering mathematics	

COMPUTER SKILLS

LaTeX, Microsoft office package, Adobe Illustrator, MATLAB, Mathematica, Comsol Multiphysics, Ansoft HFSS, Agilent's ADS, CST studio, Lumerical, Altium (PCB designer), Idea Maker (for 3D printing), Blender (3D computer graphics software), Microsoft Visio,Pspice, Proteus, Verilog, Fortran, C++, python.

EXPERIMENTAL SKILLS

• Acoustic data physics analyzer (Link)
   Corresponding research paper (Link)

- 3D printer (Link)
  Corresponding research paper (Link)
- Real-time target machines (Link)
  Corresponding research paper (Link)
- Scanning laser vibrometer (Link)
  Corresponding research paper (Link)
- Vector network analyzer and spectrum analyzer (Link)
  Corresponding research paper (Link)
- Printed circuit board (PCB) implementation (Link)
  Corresponding research paper (Link)
- Oscilloscope (Link)
  Corresponding research paper (Link)
- Acoustic reverberation room (Link)
  Corresponding research paper (Link)
- Electromagnetic and acoustic an-echoic chambers (Link)
  Corresponding research paper (Link)

SELECTED TECHNICAL REVIEW ACTIVITIES

- Nature Communications
- Physical Review Letters
- Physical Review Applied
- Physical Review B
- Applied Physics Letters
- Optics Letters

REFERENCES

- **Professor Romain Fleury**
  Assistant Professor
  Swiss Federal Institute of Technology (EPFL)
  EPFL STI IEL LWE ELB 033 (Bâtiment ELB) Station 11 CH-1015 Lausanne
  romain.fleury@epfl.ch • +41 21 693 56 88

- **Professor Andrea Alu**
  Full Professor
  CUNY Advanced Science Research Center
  City University of New York 85 St. Nicholas Terrace – Room 2. 322 New York, NY 10031, U.S.A.
  aalu@gc.cuny.edu • +1.212-413-3260

- **Professor Nader Engheta**
  Full Professor
  University of Pennsylvania
  200 South 33rd Street, Room 215, Moore Building, U.S.A.
  engheta@seas.upenn.edu • +1.215-898-9777

- **Professor Geoffroy Lerosey**
  Assistant professor
  Institut Langevin, ESPCI ParisTech, CNRS
  6 rue Jean Calvin 75005, Paris France
  geoffroy.lerosey@greenerwave.com • +33 6 23 83 66 14

- **Professor Dimitrios Sounas**
  Assistant professor
  Wayne State University
  5050 Anthony Wayne Dr., Detroit, MI 48202 Engineering Room 3137
  dsounas@wayne.edu • +1 313 577-0458